

# **SiC-VSI with Sinusoidal Voltages for an Enhanced Sensorless Control of the Induction Machine**

Von der Naturwissenschaftlich-Technischen Fakultät  
der Universität Siegen

Zur Erlangung des akademischen Grades

**Doktor der Ingenieurwissenschaften**

(Dr.-Ing.)

genehmigte Dissertation

von

M.Sc. Harith Al-Badrani

aus Mosul, Irak

1. Gutachter: Prof. Dr.-Ing. Mario Pacas
2. Gutachter: Prof. Dr.-Ing. Ralph Kennel

Tag der mündlichen Prüfung: 18.12.2018



## Acknowledgment

The road is about to end, and the moment of farewell draws closer with the completion of this dissertation. Thus, I would like to take the opportunity to thank everyone who helped me through the years to accomplish this work.

This work has been carried out thanks to the Ministry of Higher Education and Scientific Research in Iraq.

I would like to thank my advisor, Prof. Dr.-Ing. Mario Pacas. I owe him especially for his decisive support of my PhD study and research. He was a tremendous mentor through his patience, motivation, and immense knowledge. I am grateful for his priceless advice on my research, and career as well.

I would also like to express my gratitude to Prof. Dr.-Ing. Ralph Kennel, Prof. Dr.-Ing. Günter Schröder and Prof. Dr. rer. nat. Frank Gronwald, for serving as my committee members, despite great hardship. Thanks for your brilliant comments, suggestions, and for making my defense such an enjoyable moment.

Dr.-Ing. Simon Feuersänger, Dr.-Ing. Van Trang Phung, and Dr.-Ing. The Minh Phan: this research could not have been conducted without their precious support.

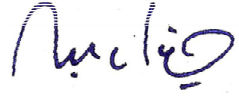
I am thankful for my close friend, Othman Al-Jawadi. Our stimulating discussions, sleepless working nights, and the fun we had together, made the period we were together in the lab easier than I could have thought. I must not forget to thank my friends Yarub Alshallawi and Qasim Alhusaini, as well.

I am so grateful for my family. To my mother and father: words cannot express how much I appreciate all the sacrifices you have made on my behalf. Your Prayers have always sustained me.

My brother Mohammed and my sisters: thank you for your support through the years of my study that encouraged me to strive for my goal.

I cannot express my gratitude to my dear wife Alaa, who has strengthened my back so much. Her encouragement, her patience, her joy and her love, have been my greatest asset in carrying out this work, and will continue to be so in my life. For our children Mariya, Ahmed and Ruqayah, she is a loving, strong and warmhearted mother and our small family brings me daily joy.

This journey couldn't have come this far without the help and support you all gave to me.

A handwritten signature in blue ink, appearing to read "Anita", is written on a small, light-colored rectangular piece of paper that is slightly tilted and placed on the page.





## Abstract

In the last few years, intensive research within the field of advance control schemes for AC drives has been conducted worldwide. With the currently available control schemes, power electronic converters and signal processing the realization of motor drives featuring excellent properties in a wide speed and torque range is possible. An operation of the motor drives without restrictions demand the measurement of the angular position of the shaft. As optical high resolution encoders are sensitive to environmental influences, like dust, vibration and temperature, they are prone to failure. They also demand additional cables and interfaces. Therefore, in the last decades a worldwide extensive research in industry and academia has led to several techniques pertaining the operation of a drive without the utilization of mechanical encoders. The so called ‘sensorless’ or "encoderless" control schemes have been enhanced in multiple research works to achieve a high dynamic performance for standard electrical AC- machines.

The present work deals with the sensorless control of the asynchronous machines by using the so-called fundamental wave models of the machine. It is well-known that a sensorless control can be achieved with good performance that can be developed based on the terminal voltages and currents of the machine without any measurement of the rotor position. Unfortunately, this method fails at low stator frequencies, and therefore the sensorless operation is only possible at medium or high speed. In addition the model utilized for the control is not fed with the stator voltages since they are usually not measured. Moreover the terminal voltages are reconstructed out of their reference values which are calculated by the controller. For this reason the control task becomes more complex because the imperfections and nonlinearity of the inverter have to be considered.

Power electronics inverters equipped with SiC switches for feeding the AC machines can be operated at higher switching frequencies, many research groups have been working with such system aiming better performance, a higher efficiency and some featuring sinusoidal output voltages. Nevertheless the objective of the current research is a different one, namely to obtain smooth terminal voltages that can be easily measured in order to enhance the classical fundamental-wave, sensorless control schemes as well as of other methods like the natural field orientation (NFO) and the control with an model reference adaptive system (MRAS).

---

## Zusammenfassung

In den letzten Jahren ist weltweit eine intensive Forschung auf dem Gebiet der Steuerung und Regelung von Drehstrommaschinen erfolgt. Die bekannten Regelverfahren in Verbindung mit den verfügbaren leistungselektronischen Umrichtern sowie mit Hilfe der sehr weit entwickelten, schnellen, elektronischen Signalverarbeitung, ermöglichte die Realisierung von elektrischen Antrieben mit hervorragenden Eigenschaften in einem weiten Drehzahl- und Drehmomentbereich. Ein geregelter Betrieb der Asynchronmaschine ohne Einschränkungen im Drehzahlstellbereich verlangt allerdings die Messung der Winkelposition des Rotors. Allerdings sind optische hochauflösende Encoder empfindlich gegen Umwelteinflüsse, wie Staub, Vibration und Temperatur, und reduzieren folglich die Systemzuverlässigkeit. Weiterhin erfordern sie zusätzliche Kabel und Schnittstellen. Daher hat man sich in den letzten Jahrzehnten, sowohl in der akademischen Welt als auch in der Industrie, mit der Entwicklung von Regelverfahren befasst, die ohne die Verwendung von mechanischen Drehgebern (Encodern) funktionieren. Diese sogenannten "sensorlosen" oder "geberlosen" Regelungen wurden in vielen Forschungsarbeiten intensiv untersucht und ständig verbessert, um eine hohe Dynamik mit Standard-Asynchronmotoren in einem weiten Drehzahlbereich zu erzielen.

Es ist bekannt, dass eine Regelung der Asynchronmaschine mit alleiniger Verwendung der Klemmengrößen (Statorstrom und -spannung) ohne Messung der Rotorposition möglich ist. Leider versagen solche Methoden bei sehr kleinen Statorfrequenzen und finden deshalb nur bei höheren Drehgeschwindigkeiten Verwendung. Darüber hinaus, wird in solchen Verfahren die Messung der Klemmenspannungen vermieden und anstatt dessen die von der Regelung errechneten Sollgrößen verwendet. Die Realisierung wird deshalb komplexer, denn etwaige Nichtlinearitäten und Unzulänglichkeiten des Wechselrichters müssen im Modell berücksichtigt werden.

Für die Speisung der Asynchronmaschine können auch mit SiC-Schaltern ausgestattete Wechselrichter verwendet und mit sehr hohen Schaltfrequenzen betrieben werden. In einigen Forschungsarbeiten wurden solche Systeme im Hinblick auf eine bessere Effizienz und Dynamik sowie auf die Glättung der Klemmenspannung untersucht. Die Vorliegende Arbeit verfolgt allerdings ein anderes Ziel, nämlich die Messung der nahezu sinusförmigen Statorspannungen zur Verbesserung der bekannten sensorlosen Regelverfahren sowie die Untersuchung der "Natürlichen Feldorientierten Regelung" und die Modell-Referenz-Regelung bei Speisung mit gemessenen Spannungen.

# Contents

<b>Acknowledgment</b> .....	<b>i</b>
<b>Abstract</b> .....	<b>iv</b>
<b>Zusammenfassung</b> .....	<b>v</b>
<b>Contents</b> .....	<b>vi</b>
<b>Nomenclatures</b> .....	<b>ix</b>
<b>1 Introduction</b> .....	<b>1</b>
1.1 Motivation of the present work .....	1
1.2 State of the art .....	2
1.2.1 Sensorless control of the induction machine .....	2
1.2.1.1 Fundamental wave models .....	2
1.2.1.2 Natural Field Orientation (NFO) .....	4
1.2.1.3 Model reference adaptive system .....	4
1.2.2 Silicon Carbide (SiC) semiconductor devices .....	5
1.2.3 Topology of the inverter output filter .....	7
1.3 Objectives of this work .....	7
1.4 Outline of the chapters .....	8
<b>2 Theoretical Concepts</b> .....	<b>10</b>
2.1 Modeling of the Induction Machine (IM) .....	10
2.1.1 Mathematical model of the induction machine .....	10
2.1.2 Machine equations in the complex form .....	10
2.1.2.1 The space phasor .....	11
2.1.2.2 Coordinate transformations .....	15
2.1.3 Mathematical description of the induction machine in the complex form .....	16
2.2 Inverters .....	19
2.2.1 Voltage Source Inverter (VSI) .....	19
2.2.2 Pulse Width Modulation (PWM) .....	20

---

2.3	Silicon Carbide semiconductors .....	20
2.3.1	Special features of silicon carbide switches.....	20
2.3.2	Silicon carbide MOSFET based inverter .....	22
2.3.3	Dead-time effect.....	22
2.3.4	Considerations for the design of an inverter with SiC modules .....	23
2.4	Design of the inverter output filter.....	26
2.5	Summary of the chapter .....	28
<b>3</b>	<b>Control of the Induction Machine.....</b>	<b>29</b>
3.1	Introduction.....	29
3.1.1	Principle of the Field Oriented Control.....	30
3.2	Sensorless speed control of an induction machine .....	34
3.2.1	Classification of sensorless control.....	35
3.2.2	Principal fundamental wave models .....	37
3.2.2.1	Current model.....	37
3.2.2.2	Voltage model .....	39
3.2.2.3	Enhanced voltage model (EUM).....	41
3.2.2.4	Natural Field Orientation.....	43
3.3	Model Reference Adaptive System (MRAS) .....	47
3.3.1	Adaptive Method (AM).....	47
3.3.2	Model reference adaptive system method.....	47
3.3.2.1	MRAS when using voltage and current model .....	49
3.3.2.2	MRAS with the NFO model as reference .....	51
3.4	Summary of the chapter .....	51
<b>4</b>	<b>Enhancement of the Conventional Control Techniques.....</b>	<b>53</b>
4.1	Sinusoidal voltages and practicability of the measurement .....	53
4.2	Enhancement of the standard voltage model .....	56
4.2.1	Dead time .....	56
4.2.2	Transistor nonlinearity .....	58

4.2.3	Delay in the signal processing .....	58
4.3	Practical realization of the integrator.....	61
4.3.1	Low gain feedback.....	62
4.3.2	Feedback with a PI element.....	63
4.4	Measurement of the terminal voltages in the low speed range .....	65
4.5	Mandatory experimental validation.....	67
4.6	Summary of the chapter.....	67
<b>5</b>	<b>Experimental Validation.....</b>	<b>68</b>
5.1	Experimental setup .....	68
5.1.1	Implementation of the controller and sensors.....	70
5.1.2	SiC two-level inverter.....	71
5.1.3	Induction machine and load.....	74
5.1.4	Filter design .....	75
5.2	Experimental results .....	76
5.2.1	General open loop behavior of voltage model.....	76
5.2.2	Integration with proportional feedback.....	79
5.2.3	Field oriented control schemes .....	82
5.2.3.1	Identification of the rotor flux space phasor .....	82
5.2.3.2	Field oriented torque control with different voltage models .....	89
5.2.4	Model reference adaptive system.....	93
5.2.4.1	Steady state behavior of the MRAS with different reference model .	94
5.2.4.2	Dynamic behavior .....	96
5.3	Summary of the chapter.....	110
<b>6</b>	<b>Conclusions .....</b>	<b>111</b>
<b>7</b>	<b>Appendix .....</b>	<b>112</b>
<b>8</b>	<b>References .....</b>	<b>113</b>

## Nomenclatures

### Symbols

$ r $	Absolute value
$ \underline{r} $	Magnitude of a space phasor
$D$	Diode
$p$	Number of pole pairs
$S$	Power semiconductor switch
$S$	Sector
$s$	Laplace variable
$i, I$	Current
$j$	Imaginary unit ( $j^2 = -1$ )
$J$	Moment of inertia
$\text{Im}\{\underline{r}\}$	Imaginary part
$\text{Re}\{\underline{r}\}$	Real part
$K$	Proportional constant
$d, q$	Axis of a system of rotating coordinates
$L$	Inductance
$R$	Resistance
$T$	Torque
$T$	Period duration
$u, U$	Voltage
$\alpha, \beta$	Axis of a stationary system of coordinates
$\gamma$	Rotor angle
$\Delta$	Increment of a variable
$\xi$	Error between the reference and the adaptive models in MRAS
$\pi$	Mathematical constant
$\sigma$	Leakage Factor
$\tau$	Time constant
$\varphi$	Angular position of the rotor flux space phasor
$\Psi$	Magnetic flux
$\omega$	Angular velocity

**Matrices/ Vectors**

$[r]_{UVW}, [r]_{\alpha\beta}, [r]_{dq}$	Algebraic vectors of a space phase in the $UVW - \alpha, \beta -; d, q -$ coordinate systems, respectively
$[T]$	Transformation matrix
$[i]$	Currents Matrix
$[u]$	Voltages Vector
$[R]$	Resistance Matrix
$[L]$	Inductance Matrix
$[\psi]$	Flux Vector

**Subscripts**

$C_f$	Filter capacitor
$e_{cos}, e_{sin}$	Signals corresponding to the sin- and cos- component in the one-dimension synchronous transformation
$f_o$	Fundamental frequency
$f_c$	Cut-off Switching frequency of LC filter
$f_{sw}$	Switching frequency of the inverter
$i_\mu$	Magnetization current
$i_{d,q1}$	Stator current in $dq$ coordinate system
$i_{d,q2}$	Rotor current in $dq$ coordinate system
$i_{U,V,W}$	Stator currents in $UVW$ coordinate system
$i_{U,V,W2}$	Rotor currents in $UVW$ coordinate system
$K_v$	Gains of the P element of the PI damping
$L_{1\sigma}$	Leakage inductance of the stator
$L_{2\sigma}$	Leakage inductance of the rotor



$L_{1h}$	Mutual Inductance
$L_f$	Filter inductor
$M_i$	Electromagnetic torque
$M_L$	Load torque
$P_d$	Electrical power of the induction machine
$P_{mech}$	Mechanical power of the induction machine
$R_1$	Stator resistance
$R_2$	Rotor resistance
$r_{1U}, r_{1V}, r_{1W}$	Stator Variables in the $UVW$ coordinate system
$r_{2U}, r_{2V}, r_{2W}$	Rotor Variables in the $UVW$ coordinate system
$r_\alpha, r_\beta$	Real and imaginary parts of a space phasor in a stator-fixed coordinate system
$t_{r1}, t_{r2}$	delay of the upper and lower signal processing (optical receivers of the upper and lower gates)
$T_D$	Dead time of the inverter
$T_{on,S1}, T_{on,S2}$	Switch-on, delay of the upper and lower MOSFETs
$T_{off,S1}, T_{off,S2}$	Switch-off, delay of the upper and lower MOSFETs
$T_N$	Gains of the I element of the PI damping
$T_t$	Time delay of the inverter
$T_{i_i}, T_{i_\omega}$	Time constant of the PI current and speed controllers, respectively
$\tau_2$	Rotor time constant
$u_{0,ideal}$	Ideal output voltage
$u_0, u_1, u_2, u_3, u_4, u_5, u_6, u_7$	Switching states voltage space phasors
$u_{d,q1}$	Stator voltages in $dq$ coordinate system
$u_{d,q2}$	Rotor voltages in $dq$ coordinate system
$U_{mi}$	Nominal voltage
$u_{U,V,W1}$	Stator voltages in $UVW$ coordinate system
$u_{U,V,W2}$	Rotor voltages in $UVW$ coordinate system
$v_{RMS}$	RMS value
$U_{dc}$	DC link voltage

$u_{ind}$	The induced voltage
$x_1$	Stator Quantity
$x_2$	Rotor Quantity
$x_d$	d Component of the space phasor
$x_{el}$	Electrical Quantity
$x_L$	Load
$x_{mech}$	Mechanical Quantity
$x_q$	q Component of the space phasor
$x_U$	Phase U
$x_V$	Phase V
$x_W$	Phase W
$x_\alpha, x_\beta$	Alpha Beta Components of the space phasor
$\Psi_{U,V,W1}$	Stator flux in $UVW$ coordinate system
$\Psi_{U,V,W2}$	Rotor flux in $UVW$ coordinate system
$\hat{\omega}$	Observed mechanical angular speed of the MRAS
$\omega^*$	Reference of the angular velocity
$\omega_c$	Corner Frequency of the Low Pass Filter
$\omega_{mech}$	Mechanical velocity of the machine
$\gamma_{identified}$	Identified rotor angle
$\gamma_{mech}$	Machine mechanical angle
$\sigma_1$	Stator leakage factor
$\sigma_2$	Rotor leakage factor
$\phi_2$	Rotor flux angle

### Superscripts

$[X]^{-1}$	Inverse of a matrix
$[X]^T$	Transpose of a matrix
$X^*$	Reference value
$\hat{X}$	Observed value
$\dot{X}$	Derivative
$X'$	Referred to the stator

## Acronyms

<i>AC</i>	Alternating Current
<i>ADC</i>	Analog to digital converter
<i>AM</i>	Adaptive Method
<i>BJT</i>	Bipolar Junction Transistor
<i>DAC</i>	Digital to analog converter
<i>DC</i>	Direct Current
<i>DSP</i>	Digital Signal Processor
<i>EKF</i>	Extended Kalman Filter
<i>EMI</i>	Electromagnetic Interference
<i>ENFO</i>	Enhanced Natural Field Orientation
<i>EUM</i>	Enhanced Voltage Model
<i>FOC</i>	Field-Oriented Control
<i>GaN</i>	Gallium Nitride
<i>I – Model</i>	Current Model
<i>IGBT</i>	Insulated-Gate Bipolar Transistor
<i>IM</i>	Induction Machine
<i>JFET</i>	Junction Field Effect Transistor
<i>K</i>	Constant
<i>LPF</i>	Low Pass Filter
<i>MID</i>	Middle points of the DC-Link capacitors
<i>MOSFET</i>	Metal–Oxide–Semiconductor Field-Effect Transistor
<i>MRAC</i>	Model Reference Adaptive Control
<i>MRAS</i>	Model Reference Adaptive System
<i>NFO</i>	Natural Field Orientation
<i>PC</i>	Personal Computer
<i>PCB</i>	Printed Circuit Board
<i>PI</i>	Proportional-Integral
<i>PLL</i>	Phase Lock Loop
<i>PV</i>	Photo-Voltaic
<i>PWM</i>	Pulse Width Modulation
<i>RM</i>	Reference Model

<i>Si</i>	Silicon
<i>SBD</i>	Schottky Barrier Diode
<i>SiC</i>	Silicon Carbide
<i>SUM</i>	Standard Voltage Model
<i>UM</i>	Voltage Model
<i>VDF</i>	Variable Frequency Drive
<i>VSI</i>	Voltage Source Inverter
<i>WBG</i>	Wide Band Gap

# 1 Introduction

## 1.1 Motivation of the present work

Commercially available wide bandgap (WBG) semiconductors may replace Silicon (Si) switches in many applications, as they can enhance the efficiency of power electronic devices by reducing the switching losses at a given switching frequency [1]. In order to improve the efficiency, size, cost, and control features, some of the power electronic SiC-devices are currently used in switched mode power supplies (SMPS) and can be evaluated for their utilization in motor drives. It is also reported that power electronics inverter equipped with WBG switches like SiC-Mosfets are used in systems for renewable energy generation (e.g.: solar panels and wind turbines) and achieve a higher efficiency [2] and [3]. Therefore, WBG semiconductors can be considered as potentially beneficially to the development of more efficient inverters for renewable energy sources.

The availability of Silicon Carbide (SiC)-switches gives the design of conventional inverters the ability to operate at higher switching frequencies: up to 100 kHz or even more. For the feeding of three-phase machines, these high switching frequencies are not necessary and therefore dispensable in common industrial drives. Nevertheless, the high switching frequency of the inverter may be an advantage if the output voltages are appropriately filtered and become rather sinusoidal. In this way, some of the negative effects of the usually non-sinusoidal voltage may be attenuated while the performance of the sensorless control can become more efficient.

In terms of control, one of the most widely used topologies for the control of the Induction Machine (IM) is the encoder-less Field Oriented Control (FOC). It has been shown that the elimination of the position or speed sensor in variable speed drives may decrease the sensor cost and hence increase the system's reliability [4] and [5].

In this work, it is shown that the SiC inverter with an output LC filter for feeding an induction machine can produce almost sinusoidal voltages on the terminals of the machine. The advantages of a three-phase, two-level voltage source inverter (VSI) equipped with silicon carbide-switches and an output filter are: minimizing the harmonic content of the machine voltages, reducing the stress on the winding of the machine and the produced noise and extending the range of operation of a sensor-less field oriented

control scheme. This work aims to the improvement in the quality of the voltages that will be exploited for the enhancement of the voltage model that is used for the estimation of the rotor flux space phasor in field orientated control schemes.

## **1.2 State of the art**

. First the developments in the area of sensorless field oriented control of the induction machine by using fundamental wave models are described. In addition the state of knowledge in the areas of Natural Field Orientation (NFO), Model Reference Adaptive System (MRAS) and the wide bandgap (WBG) especially, Silicone Carbide (SiC) devices that are used in the two-level voltage source inverter in the present work are also discussed.

### **1.2.1 Sensorless control of the induction machine**

Since the 1970s, the vector control which is also named field oriented control (FOC), was comprehensively investigated [6] and [7]. It is reported that the indirect method of field orientation control was introduced by K. Hasse [8], while the direct method of field orientation was presented by F. Blaschke [9]. Explanations to vector control and field orientation of asynchronous motors are provided in the publications [10] and [11].

#### **1.2.1.1 Fundamental wave models**

As optical high resolution encoders are sensitive to the influences of the environment like mechanical shock, dust and temperature, they are prone to failure. The optical encoders also demand additional cables and interfaces [12]. Thus, extensive research in the last decades has led to several techniques pertaining the operation of a drive without the utilization of mechanical encoders. The so called ‘speed-sensorless’ control schemes have been enhanced by different research groups in academia and industry to achieve a control with high dynamic and good performance for standard electrical machines [13] - [24]. A good description of the state of the art and the classification of different approaches can be found in [25].

The fundamental wave models are methods that use the classical dynamic equations of the AC machine that assume sinusoidal distribution of the magnetic flux density in the air gap and neglect the space harmonics and other secondary effects. These methods

may be employed in the development of control schemes for the corresponding machines in order to obtain the information of the speed or to estimate the rotor position. Hence additional test signals or special unbalanced characteristics of the motor are not required. The fundamental wave models are applied for a very wide range of machine types as they demand less implementation effort in comparison with those that apply test signals and are well applicable at higher speeds. Basically, a stable control of the machine at standstill, i.e. zero stator frequency, is not possible with these methods because if the induced voltage in the rotor is zero, then the system becomes unobservable [25]. On the other hand, because these methods are based on a model of the machine, they are often subjected to parameter variations in temperature-dependent quantities, such as resistances, which must be adapted during the operation to obtain a reliable estimation of the speed, or even subject to measurement errors in the current measurement.

During the last five decades, the fundamental wave models were improved to provide better performance even at low speeds of operation. Thus, several important methods have been developed in order to obtain the angle of the rotor flux space phasor. By using the so-called ‘current model’, a simple approach is introduced where only the stator current and the rotor angular position are needed for the determination of the angular position of the rotor flux space phasor [26] - [28].

To avoid using an angular sensor, a sensorless control scheme based on the voltage model of the induction machine could be used [29] and [30]. The most substantial disadvantage of this approach is the presence of two open-loop integrators responsible for the calculation of the stator flux space phasor. To overcome this problem, many different models were modified such as [31] - [35].

Due to the nonlinearities of the inverters, the models used in the control schemes have to be corrected. Some additional drawbacks include measurement errors in the current measurement like offset or noise, as well as in the temperature change of the value for the stator resistance  $R_1$  [36], [13] and [4]. All these effects lead to an inaccurate estimation of the stator flux, particularly at very low stator frequencies and unloaded machines [37], [38] and [39]. Therefore, various approaches pursue a way to modify the integration to an equivalent operation, which is less susceptible to these effects, such as a first-

order delay or a band-pass [40] - [45]. Although this approximation is quite accurate for higher frequency values, it leads to a wrong output variable for the stator flux at a stator frequency below the cutoff frequency of the low pass filter (LPF) element. [46], [47] and [48]. The effective implementation of modified integration methods can be found in [49], [50] and [4]. However determining the nonlinearities of the inverter, estimating the stator resistance, as well as correcting the offsets, add more complexity to the simple structure of the voltage model.

### **1.2.1.2 Natural Field Orientation (NFO)**

The control method for the induction machine called "natural field orientation (NFO)" was presented in the literature in 1980 by Ranger Jönsson and patented as "Method and apparatus for controlling an AC motor" in 1994 [51] and [52]. The idea behind the NFO is that the stator flux space phasor is lagging  $90^\circ$  to the induced stator voltage space phasor. With the assumption that the magnitude of the stator flux is constant, the position of the stator and of the rotor flux space phasor can be calculated [1], [53] and [54].

A full dynamic model of the NFO structure was developed and presented in [55] and [56], showing the results of its linearized stability analysis. The NFO scheme also uses the stator voltages for the calculation of the induced voltages and thus for obtaining the rotor flux space phasor [57], [58] and [59]. The natural field orientation has some interesting parameter robustness properties, thus, the investigation of the parameter error effects on the frame alignment accuracy of the NFO has been presented in [60] and [61]. An advanced system for dead time compensation in the pulse width modulation (PWM) circuit was proposed in the NFO control system to enhance the control scheme [62].

### **1.2.1.3 Model reference adaptive system**

Model Reference Adaptive System (MRAS) is an adaptive control technique, which modifies the parameters of a model until it delivers a satisfying fitting and a comparable output like a reference model. For the control of the induction machine, the MRAS can use the possibility of calculating the same state variables of the machine, such as the rotor flux space phasor from two independent sets of equations or machine models. The first model can be the voltage model (UM) or the natural field orientation (NFO) and it



does not include the mechanical angular velocity  $\omega_{mech}$ . For the MRAS, the current model is the second one and contains the mechanical angular velocity  $\omega_{mech}$  as variable. In the specific case of the sensorless determination of the rotor position, the voltage model or the NFO model is used as a reference model and the parameter of identified rotor angle  $\gamma_{identified}$ , adapted until the current model is fitted and provides the same direction of the stator flux space phasor. At this point, the estimated angular velocity is assumed to correspond to its real value and may be employed for the speed control. The basic structure of the adaptive methods with reference model and a speed estimator was shown previously in [63].

There are various approaches in the literature concerning the MRAS control of the induction machine; some of these take into account the extended functions. Thus, the determination of the error between the state variables of both models can be realized in different manners: an implementation by using the rotor flux is reported in [21] and [64], while in [17] the stator current was used, however in [65] and [66] the stator machine voltages are used to determine the estimation error between the two models.

In order to extend the possibility of using the encoder-less methods, the stable work at very low speeds is presented in [4] and [5], and an additional adaptation of the value of the stator or rotor resistance is used.

A tracking allows a more accurate representation of the model, which permits more favorable estimation of the state variables. Additional corrections of the stator voltage calculation in the voltage model are reported in [67] and [68]. Examinations and results for adaptations of the MRAS structure with predictive control elements for speed estimation or fuzzy logic systems can be found in [18] and [69].

### 1.2.2 Silicon Carbide (SiC) semiconductor devices

Conventional Si-MOSFETs or Si-IGBTs are currently the most widely used semiconductor switches in inverters. Si-MOSFET exhibits switching frequency from ten to hundreds of kHz. However, conventional Si-MOSFETs have a disadvantage associated with the high "on" resistance, which rapidly increases with the rated blocking voltage.

The Si-MOSFETs featuring blocking voltage of 600V, 1200V are costly and have a limited availability. Currently, Silicon Carbide MOSFETs are available with blocking voltages of 1200V and on-resistance of 80 m $\Omega$  compared to on-resistance up to 1000 m $\Omega$  of Si-MOSFETs. They are ideal for applications like voltage source inverter [70] and offer an interesting field of investigation. An overview of new advances in novel Silicon Carbide and Gallium Nitride GaN-based power devices can be found in [71]. The Silicon Carbide SiC devices have efficient electrical properties that may replace Si switches in many applications [72] and [73]. The performance of the SiC MOSFET model based motor drive is compared with an equivalent silicon IGBT model drive in [70]. As reported in [3] by replacing the Si switches with SiC ones, the switching losses can be significantly reduced. The capability of SiC devices to work at extremely high ambient temperatures make them suitable for many automotive and aerospace applications [74], nevertheless high-temperature consistent device packaging has needed to be suitable for such environments [75] and [76].

SiC-based power switches are also suitable for high voltage applications. SiC power switches in 1,2 kV modules are available [77] and are an appropriate alternative in this voltage range since they exhibit a low specific on-resistance and are able to operate at high switching frequencies and high ambient temperatures [73].

Inverters equipped with SiC switches can be operated at higher switching frequencies, therefore many research groups have been working with such system aiming better performance, a higher efficiency but some others pursuing sinusoidal output voltages [67] - [71].

Additional research in the field of inverter design deals with increasing the efficiency of three-phase inverter based on SiC switches by using the parallel connection of power modules with the resulting reduction of the on-state losses as presented in [78]. A SiC-inverter with a sinusoidal output filter is introduced with a compact Z-source converter in [79]. In order to verify a concept of the multi-pulse inverter at high switching frequency and to achieve near sinusoidal output voltage the design of a 10kVA inverter based on SiC power devices is discussed in [80]. In Photo-Voltaic (PV) inverters, the

initial capital cost can be reduced by using SiC technology [2], [3]. The effect of the inverter dead time is under investigation in many types of research, and decreasing the dead time was presented efficiently by using Silicon Carbide Bipolar Junction Transistor (SiC-BJT) in [81]. The demonstration of the suitability of SiC devices in power generation units for a transportation vehicle, where a significant cost reduction in the thermal management system is achieved, can be found in [82], [83] and [84].

Summarizing, the reduction of the cost and size, and increasing the lifetime and the overall efficiency is the main goal of applying SiC devices.

### **1.2.3 Topology of the inverter output filter**

The installation of small LC filters between a fast switching-type inverter and a three-phase induction machine has some advantages. For example, it protects the motor winding insulation against  $dv/dt$  as well as voltage spikes and reduces other undesired effects [85]–[90].

## **1.3 Objectives of this work**

This work focuses on the design and implementation of a three-phase, two-level voltage source inverter that is equipped with (SiC)-switches and is complemented with an output filter featuring almost sinusoidal output voltages and currents. The objective of this structure is twofold: first, the reduction of the stress on the winding of the machine and the produced noise, second to increase the range of operation of a sensorless field oriented control scheme. The high switching frequency that can be achieved with the SiC-switches allows the design of a rather small LC filter for the output of the inverter. With these values, not only the harmonic content of the currents but also the ripple of the output voltage could be significantly reduced resulting in a practically sinusoidal voltage. In this way, the measured voltages can be used instead of the reconstructed ones for the enhancement of the voltage model, as well as the natural field orientation and the performance of the control scheme.

## 1.4 Outline of the chapters

The arrangement of this thesis is as follows.

**Chapter 1** presents both the motivation for, and the objectives of, the work. In addition it describes the state of the art regarding the topics of this thesis.

**Chapter 2** presents the basic concepts that are used in this work. This chapter discusses the mathematical model of a squirrel cage induction machine (IM) that uses the machine equation in a complex form i.e. as space phasor equations.

The basic description of the wo-level voltage source inverter, which is used to supply the squirrel cage induction machine, is also presented in this chapter. Some consideration for the design of the inverter with the silicon carbide devices were included as well. Finally, the design and implementation of a small LC-filter to be connected between the fast switching-type inverter and the three-phase induction machine are considered.

**Chapter 3** covers the principle of field oriented control (FOC) theory for the induction machine (IM). In addition, this chapter also focuses on the sensorless control of the induction machine and on the calculation of the rotor space phasor by two methods both based on the fundamental wave equations of the machine. The first approach employs the measured mechanical rotor position and the stator currents and is called the current model. The second one represents a simple approach without an additional speed sensor, thus the rotor flux phase phasor can be obtained by using the terminal stator voltages and currents. The voltage model of the induction machine is a convenient flux estimator model due to its simplicity; hence the stator resistance is only the important parameter of this model.

An enhancement of the voltage model is introduced that can be achieved if the model is fed with the measured terminal voltages instead of using the voltage reconstructed from the switching signals of the inverter.

The principle of control by using a model reference adaptive system (MRAS) is also included in this chapter. Finally, the natural field orientation (NFO) is discussed as an efficient control technique for the induction machine. An enhancement of the natural field orientation (ENFO) can be achieved, when the measured terminal voltages are used instead of the calculated ones.

**Chapter 4** shows the enhancement of the conventional control techniques by using the measured terminal voltages. The difference between the pulsating and sinusoidal voltages is described and the practicability of measurements is described as well. It explains some of the drawbacks of the voltage model fed by reference values of the voltages (standard voltage model) and some methods for the elimination of errors and non-linearities.

The measurement of the terminal voltages by using up-to-date electronics and only in the low voltage range is viewed as an unimplemented, but new, idea.

**Chapter 5** describes the structure of the experimental setup which was used for the validation of the theoretical considerations and presents and discusses the experimental results that were obtained in the numerous experiments.

**Chapter 6** discusses the conclusions of this work and the relevance of the obtained results as well. The proposal of the future project also indicated in this chapter.

## 2 Theoretical Concepts

### 2.1 Modeling of the Induction Machine (IM)

#### 2.1.1 Mathematical model of the induction machine

A useful study of an induction machine operation requires an active mathematical model. The mathematical representation of the three-phase induction machine should include the relationship between the electromagnetic torque and all the electrical and mechanical values of the machine. The modeling and analyzing of the induction machine as a dynamic system is the first step for its understanding and for the design of a control scheme. In order to model the induction machine, different methods are possible as already described in [40], [42].

The following assumption are adopted when the mathematical equations are written in order to simplify them [40], [43], [91]:

- Stator and rotor windings are sinusoidally distributed in space and replaced by an equivalent concentrated winding.
- The field distribution along the periphery of the air gap is sinusoidal.
- A symmetrical design of the electrical machine.
- The iron is not saturated.
- The stator and the rotor surfaces are cylindrical.
- The rotor bars are equally distributed along the surface of the squirrel rotor cage.
- The rotor bars are insulated from the rotor core.
- The air gap between the rotor and stator is symmetric.
- Hysteresis, eddy currents, anisotropy effect, core loss and skin effect, all are not considered.
- The resistance and inductance of the stator and rotor windings do not vary with the temperature.
- The friction and windage losses are neglected and the mechanical couple is stiff.

#### 2.1.2 Machine equations in the complex form

The mathematical model of the induction machine, which considers all the rotor loops of the rotor cage, is too complex, especially when it is used for the development

of a control scheme. Therefore, the model of the induction machine which is used in its control is based on the space phasor theory which will be described in the following [42] [92] [93].

### 2.1.2.1 The space phasor

The space phasor theory was first presented in the fifties of the 20th century by the Károly Pál Kovács [94]. Given the utility of this theory, it has been developed by Jaroslav Stepina [95] and L. Serrano-Iribarnegaray [96]. This theory provides a very useful tool to deal with the three-phase system in general. Due to the usefulness of this theory in three-phase systems, it has been used in order to describe the dynamic behavior of the three-phase induction machine. The space phasor has the ability to deal with complex variables that summarize the instant values of three-phase quantities, therefore, it is not limited to the description of steady-state behavior, but it is valid for the transient states and non-sinusoidal analysis.

Under the assumption that there is no zero component in a three-phase system, i.e. the three instantaneous values  $r_U(t)$ ,  $r_V(t)$  and  $r_W(t)$  of a three-phase quantity  $r$  satisfy

$$r_U(t) + r_V(t) + r_W(t) = 0 \quad (2.1)$$

the quantity  $r$  can be represented in a space phasor  $\underline{r}(t)$  defined by

$$\underline{r}(t) = \frac{2}{3} (r_U(t) + \underline{a} \cdot r_V(t) + \underline{a}^2 \cdot r_W(t)) \cdot e^{j\gamma_i} \quad (2.2)$$

where

$$j^2 = -1; \underline{a} = e^{j\frac{2\pi}{3}} = -\frac{1}{2} + j\frac{\sqrt{3}}{2}; \underline{a}^2 = e^{j\frac{4\pi}{3}} = -\frac{1}{2} - j\frac{\sqrt{3}}{2} \quad (2.3)$$

It is still necessary to define the angle  $\gamma_i$ , which is referred to an arbitrary reference axis, to complete the space phasor representation (2.2). For stator quantities, the angle  $\gamma_i = \gamma_1$  is the position of the axis of the stator winding phase  $U$  with respect to a given reference frame. Normally  $\gamma_1 = 0$  is chosen, and (2.2) can be rewritten as:

$$\underline{r}(t) = \frac{2}{3} (r_U(t) + \underline{a} \cdot r_V(t) + \underline{a}^2 \cdot r_W(t)) \quad (2.4)$$

The instantaneous value of the three phases can be obtained by making a projection of the space phasor on the corresponding axis

$$r_U = \text{Re}\{\underline{r}\}; \quad r_V = \text{Re}\{\underline{r} \cdot \underline{a}^{-1}\}; \quad r_W = \text{Re}\{\underline{r} \cdot \underline{a}^{-2}\} \quad (2.5)$$

In the three-dimension coordinate system  $U, V, W$ , the variable  $r$  can be represented in the form of a three-element algebraic vector as follows

$$[\underline{r}]_{UVW} = [r_U, r_V, r_W]^T \quad (2.6)$$

Figure 2-1 shows the geometric construction of the space phasor of the stator current  $\dot{i}_1$  for assumed values of  $r_U, r_V > 0$  and  $r_W < 0$ .

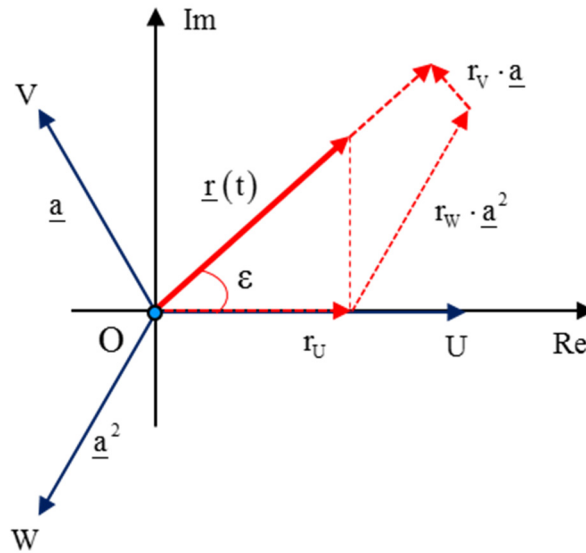


Figure 2-1 Geometric representation of the space phasor  $\dot{i}_1$

For a modeling of the three-phase electrical system a  $U, V, W$  frame of coordinates that considers each of the three-phases the  $U$ , the  $V$  and the  $W$  components as a separate entity. A simplification can be obtained by using a two-dimensional system of coordinates as it results from the space phasor representation.

By defining the angle  $\gamma_i = \gamma_1 = 0$  in (2.2) the  $\alpha, \beta$  stationary coordinates referred to the stator is defined and it is possible to obtain the components of the space phasor along the real and imaginary axis as:



$$\underline{r} = \frac{2}{3}(r_U + \underline{a} \cdot r_V + \underline{a}^2 \cdot r_W) = r_\alpha + j \cdot r_\beta, \quad (2.7)$$

with

$$\begin{aligned} r_\alpha &= \operatorname{Re}\{\underline{r}\} = \operatorname{Re}\left\{\frac{2}{3}(r_U + \underline{a} \cdot r_V + \underline{a}^2 \cdot r_W)\right\} \\ &= \operatorname{Re}\left\{\frac{2}{3}\left(r_U + \left(-\frac{1}{2} + j\frac{\sqrt{3}}{2}\right) \cdot r_V + \left(-\frac{1}{2} - j\frac{\sqrt{3}}{2}\right) \cdot r_W\right)\right\}, \\ &= r_U \end{aligned} \quad (2.8)$$

and

$$\begin{aligned} r_\beta &= \operatorname{Im}\{\underline{r}\} = \operatorname{Im}\left\{\frac{2}{3}(r_U + \underline{a} \cdot r_V + \underline{a}^2 \cdot r_W)\right\} \\ &= \operatorname{Im}\left\{\frac{2}{3}\left(r_U + \left(-\frac{1}{2} + j\frac{\sqrt{3}}{2}\right) \cdot r_V + \left(-\frac{1}{2} - j\frac{\sqrt{3}}{2}\right) \cdot r_W\right)\right\} \\ &= \frac{1}{\sqrt{3}}(r_V - r_W) \end{aligned} \quad (2.9)$$

As example, for the current space phasor results:

$$i_\alpha = i_U, \quad (2.10)$$

and

$$i_\beta = \frac{1}{\sqrt{3}} \cdot (i_V - i_W) \quad (2.11)$$

In this system, the instantaneous quantities in an equivalent two orthogonal phases can be represented as  $r_\alpha$  and  $r_\beta$ , that establishes the same resulting wave as the three-phase quantities.

In a similar way, a second frame of coordinates can be defined by choosing the angle  $\gamma_i$  as a time-varying angle  $\varphi(t)$  resulting into a two-dimensional  $d, q$  -rotating reference frame. The  $d$ -axis of the rotating reference frame is shifted by  $\varphi(t)$  from the  $\alpha$ -axis of the  $\alpha, \beta$  coordinate system as illustrated in Figure 2-2. The  $d, q$  reference frame owns a crucial advantage over the U, V, W and the  $\alpha, \beta$ -coordinate systems. If the rotational velocity  $\dot{\varphi}(t)$  is properly selected, i.e.  $\dot{\varphi}(t)$  is identical to the angular velocity of the rotating field in the airgap, the space phasors are observed in steady state as a DC-quantities in the  $d, q$  reference frame. As a result, the space phasors can be conveniently manipulated within control schemes. In the  $d, q$  coordinate system, the space phasor  $\underline{r}$  can be written as:

$$\underline{r}(t) = \text{Re}\{\underline{r}(t)\} + j \text{Im}\{\underline{r}(t)\} = r_d(t) + j r_q(t) \quad (2.12)$$

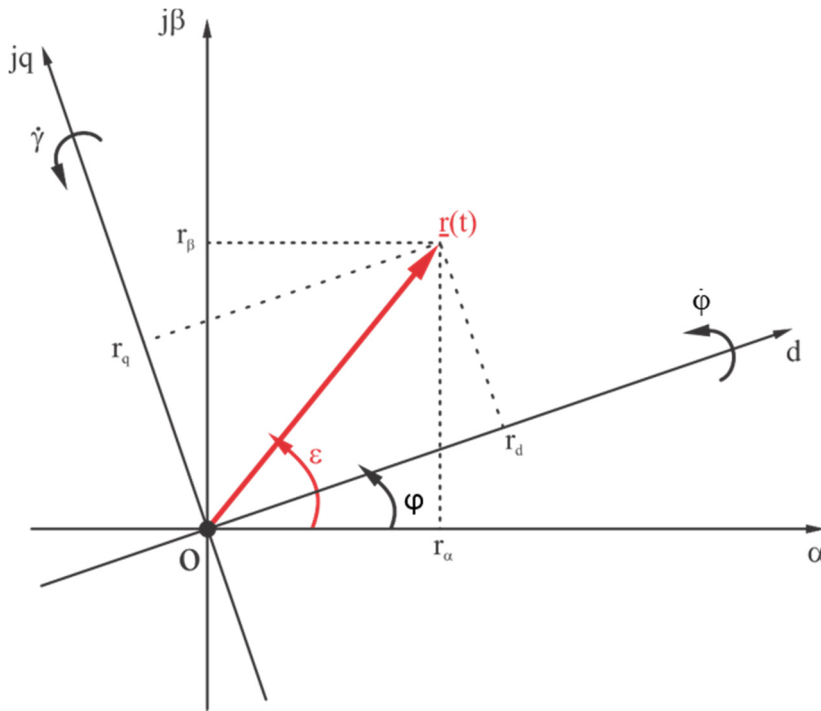


Figure 2-2 Transformation of a stator space phasor  $\underline{r}(t)$  between the fixed  $\alpha$ - $\beta$  stationary reference frame and  $d$ - $q$  rotating reference frame

It is worth noting that the space phasor representation as aforementioned is valid for any electrical and magnetic quantities, for example, current  $i$ , voltage  $u$ , magnetic flux density  $B$ , flux linkage  $\psi$ , etc.

**2.1.2.2 Coordinate transformations**

Section 2.3.1 illustrates that the quantity  $r(t)$  belonging to the space phasor  $\underline{r}(t)$  can be represented in one of the three coordinate systems: the  $U, V, W$ -, the  $\alpha, \beta$ - and the  $d, q$ - coordinate systems.

According to (2.8) and (2.9), the transformation from the  $U, V, W$ - to the  $\alpha, \beta$ - coordinate system is as follows:

$$\begin{bmatrix} r_\alpha \\ r_\beta \end{bmatrix} = \begin{bmatrix} 1 & 0 & 0 \\ 0 & \frac{\sqrt{3}}{3} & -\frac{\sqrt{3}}{3} \end{bmatrix} \cdot \begin{bmatrix} r_U \\ r_V \\ r_W \end{bmatrix} \tag{2.13}$$

And, the inverse transformation from the  $\alpha, \beta$  - to the  $U, V, W$ - coordinate systems is given by:

$$\begin{bmatrix} r_U \\ r_V \\ r_W \end{bmatrix} = \begin{bmatrix} 1 & 0 \\ -\frac{1}{2} & \frac{\sqrt{3}}{2} \\ -\frac{1}{2} & -\frac{\sqrt{3}}{2} \end{bmatrix} \cdot \begin{bmatrix} r_\alpha \\ r_\beta \end{bmatrix} \tag{2.14}$$

The transformations between the  $U, V, W$  and the  $\alpha, \beta$  coordinate systems and vice versa can be represented blocks depicted in Figure 2-3.

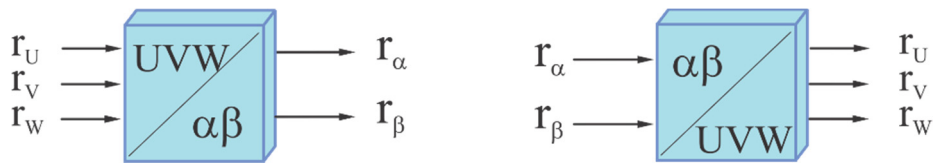


Figure 2-3 Blocks representing the transformations between the  $UVW$  and the  $\alpha, \beta$  coordinates and vice versa

Regarding the transformation between the  $\alpha, \beta$  and the  $d, q$  coordinate systems and vice versa, Figure 2-4 shows the blocks representing these transformations.



Figure 2-4 Blocks representing the transformations between the  $\alpha, \beta$  and the  $d, q$  coordinates and vice versa

As depicted in Figure 2-2  $r_\alpha + j \cdot r_\beta = |r| \cdot e^{j\epsilon t}$  and  $r_d + j \cdot r_q = |r| \cdot e^{j(\epsilon t - \varphi)}$ . Consequently, the transformation from the  $\alpha, \beta$  coordinate system to the  $d, q$  reference frame is as follows:

$$\begin{aligned} r_\alpha + j \cdot r_\beta &= (r_d + j \cdot r_q) \cdot e^{j\varphi} \\ &= (r_d + j \cdot r_q) (\cos \varphi + j \cdot \sin \varphi) \\ &= (r_d \cdot \cos \varphi - r_q \cdot \sin \varphi) + j \cdot (r_d \cdot \sin \varphi + r_q \cdot \cos \varphi) \end{aligned} \quad (2.15)$$

By decomposing in the real and the imaginary parts in (2.15) results:

$$\begin{bmatrix} r_\alpha \\ r_\beta \end{bmatrix} = \begin{bmatrix} \cos \varphi & -\sin \varphi \\ \sin \varphi & \cos \varphi \end{bmatrix} \cdot \begin{bmatrix} r_d \\ r_q \end{bmatrix} \quad (2.16)$$

and for the inverse transformation (2.60) follows:

$$\begin{bmatrix} r_d \\ r_q \end{bmatrix} = \begin{bmatrix} \cos \varphi & \sin \varphi \\ -\sin \varphi & \cos \varphi \end{bmatrix} \cdot \begin{bmatrix} r_\alpha \\ r_\beta \end{bmatrix} \quad (2.17)$$

### 2.1.3 Mathematical description of the induction machine in the complex form

The voltage equations of the induction machine can be expressed by using the space phasors theory. The complex equations that describe the dynamic behavior of the induction machine in a general frame of the coordinate is given by [27]:

$$\underline{u}_1 = R_1 \cdot \underline{i}_1 - j \cdot \dot{\gamma}_1 \cdot \underline{\psi}_1 + \dot{\underline{\psi}}_1 \quad (2.18)$$

$$\underline{u}'_2 = R'_2 \cdot \underline{i}'_2 - j \cdot \dot{\gamma}_2 \cdot \underline{\psi}'_2 + \dot{\underline{\psi}}_2 \quad (2.19)$$

For squirrel-cage rotor type, the voltage in the rotor becomes:

$$0 = R'_2 \cdot \underline{i}'_2 - j \cdot \dot{\gamma}_2 \cdot \underline{\psi}'_2 + \dot{\underline{\psi}}_2 \quad (2.20)$$

The flux space phasors of the rotor and stator can be written as:

$$\underline{\Psi}_1 = L_1 \cdot \dot{i}_1 + L_{1h} \cdot \dot{i}_2 = (L_{1h} + L_{1\sigma}) \cdot \dot{i}_1 + L_{1h} \cdot \dot{i}_2 \quad (2.21)$$

$$\underline{\Psi}_2 = L_2 \cdot \dot{i}_2 + L_{1h} \cdot \dot{i}_1 = (L_{1h} + L_{2\sigma}) \cdot \dot{i}_2 + L_{1h} \cdot \dot{i}_1 \quad (2.22)$$

where  $L_{1h}$  is the mutual inductance and the total inductances of the stator and rotor are given as:

$$L_1 = L_{1h} + L_{1\sigma} \quad (2.23)$$

$$L_2 = L_{1h} + L_{2\sigma} \quad (2.24)$$

The leakage inductances of the rotor and the stator are  $L_{1\sigma}$  and  $L_{2\sigma}$  respectively. In addition, the leakage coefficients are defined:

Where:

$$\sigma = 1 - \frac{1}{(1 + \sigma_1) \cdot (1 + \sigma_2)} = 1 - \frac{L_{1h}^2}{L_1 \cdot L_2}, \quad \sigma_1 = \frac{L_{1\sigma}}{L_{1h}}, \quad \sigma_2 = \frac{L_{2\sigma}}{L_{1h}} \quad (2.25)$$

The spaces phasors of the currents can be calculated from the flux space phasors by using Eq. no. (2.25) and it follows:

$$\begin{bmatrix} \dot{i}_1 \\ \dot{i}_2 \end{bmatrix} = \frac{1 - \sigma}{\sigma \cdot L_{1h}} \cdot \begin{bmatrix} 1 + \sigma_2 & -1 \\ -1 & 1 + \sigma_1 \end{bmatrix} \cdot \begin{bmatrix} \underline{\Psi}_1 \\ \underline{\Psi}_2 \end{bmatrix} \quad (2.26)$$

In order to complete the description of the system, the mechanical equation is necessary:

$$M_i = J \cdot \frac{\ddot{\gamma}}{p} + M_L, \quad (2.27)$$

where the internal torque  $M_i$  can be expressed as:

$$M_i = \frac{3}{2} \cdot p \cdot \frac{(1 - \sigma)}{\sigma \cdot L_{1h}} \cdot \text{Im} \{ \underline{\Psi}_1 \cdot \underline{\Psi}_2^* \} \quad (2.28)$$

This set of complex differential equations describe the dynamic behavior of the induction machine for arbitrary voltages and load torque. Before they can be utilized, the

general reference axis depicted in Figure 2-4 has to be defined in order to get the proper relationships among the angles that are used in the equations above:

$$\gamma = \gamma_2 - \gamma_1 \quad (2.29)$$

As stated above, in case of a stator fixed system of coordinates the angle  $\gamma_1$  is zero and the equations are accordingly modified. The stator coordinates are important as they describe the currents and voltages as they are measured; however a disadvantage of this frame of coordinates is that in a machine fed by AC voltages (which is the normal case) all quantities are in steady state also AC variables. For the purpose of control a frame of coordinates, in which the variables are DC quantities is preferred and will be presented in the following.

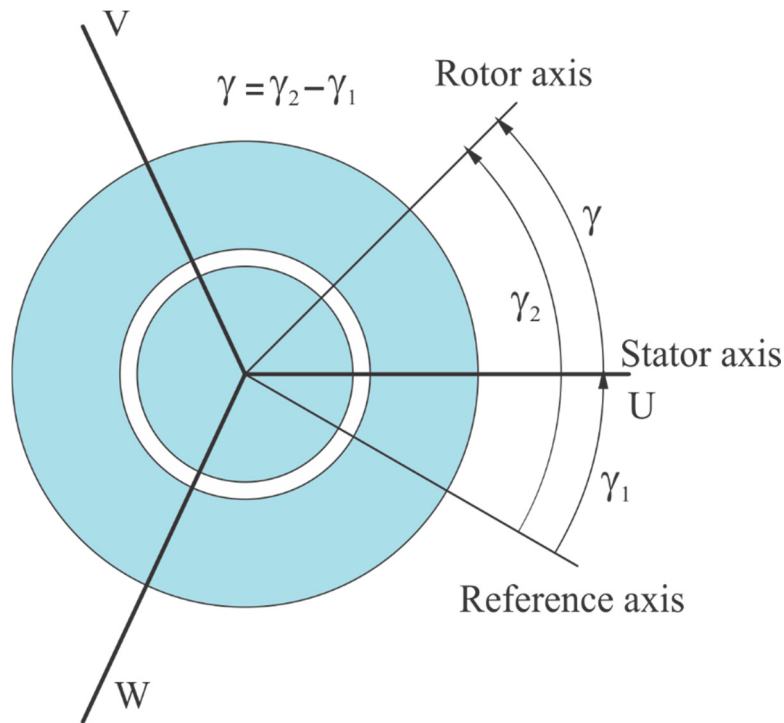


Figure 2-5 Reference angle description

## 2.2 Inverters

### 2.2.1 Voltage Source Inverter (VSI)

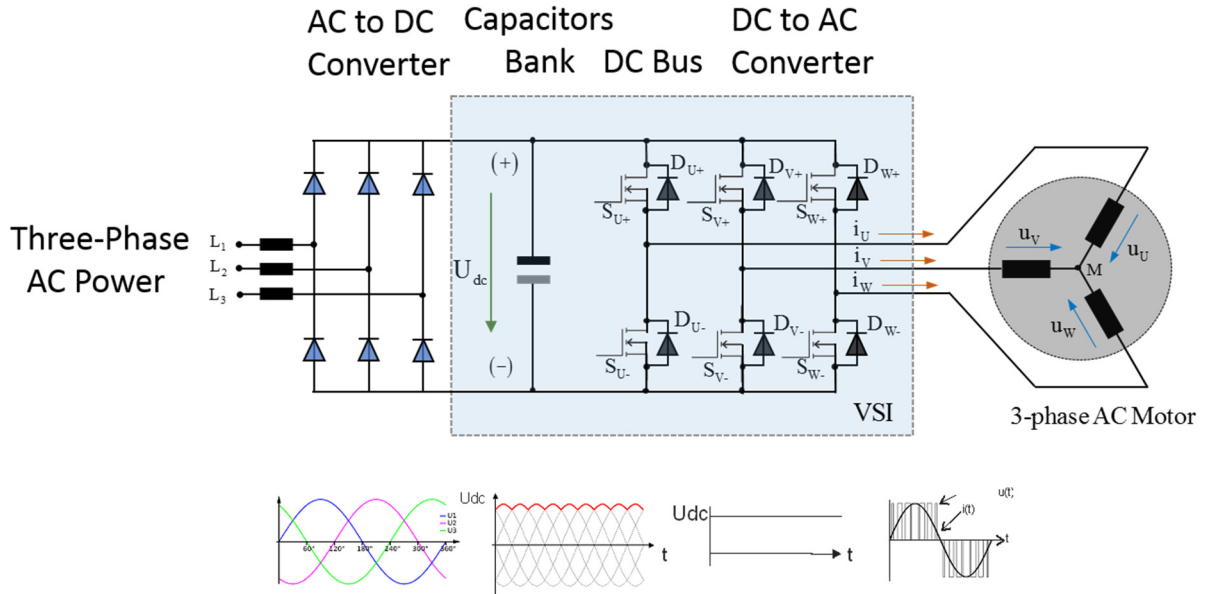


Figure 2-6 Three-phase voltage source inverter (VSI) connected to AC-motor

Figure 2-6 illustrates the typical structure of a three-phase AC variable speed drive system with a voltage source inverter (VSI). The VSI consists of three half bridges of power semiconductors, which are denoted by  $S_{U+} | S_{U-}, S_{V+} | S_{V-}, S_{W+} | S_{W-}$  corresponding to phase  $U, V$  and  $W$ , respectively. The switches have antiparallel free-wheeling power diodes with the notation  $D_{U+} | D_{U-}, D_{V+} | D_{V-}, D_{W+} | D_{W-}$ . The VSI is fed by a voltage source with the DC-link voltage  $U_{dc}$ . The VSI can convert the DC-link voltage into three-phase AC voltages by controlling the states of the power switches. The switching state of each phase is defined as [97]:

(-), in the case of the phase winding is connected to the negative potential, or

(+), in the case of the phase winding is connected to the positive potential of the DC-link voltage

By combining the possible switching states of each phase, eight voltage space phasors  $\underline{u}_0, \underline{u}_1, \underline{u}_2, \underline{u}_3, \underline{u}_4, \underline{u}_5, \underline{u}_6, \underline{u}_7$  can be obtained. The space phasor  $\underline{u}_0$ , where all the outputs are connected to the negative potential, and  $\underline{u}_7$ , where all the outputs are connected to the positive potential, are called zero voltage space phasors, because their amplitudes

are zeroed. The six remaining voltage space phasors divide the space into six equal sectors  $S_1 \cdots S_6$  as shown in Figure 2-7.

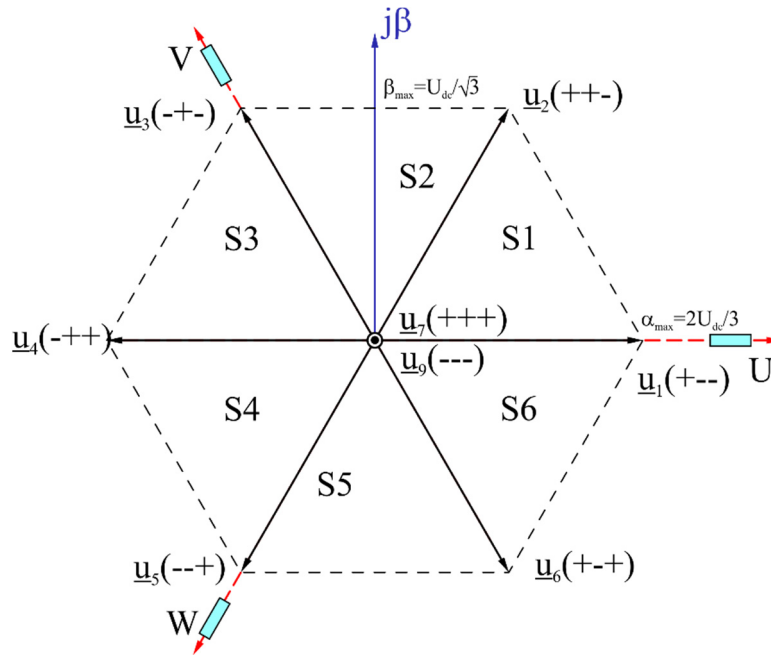


Figure 2-7 Standard voltage space phasors  $\underline{u}_0 \cdots \underline{u}_7$  provided by a two-level voltage source inverter (VSI)

## 2.2.2 Pulse Width Modulation (PWM)

In motor drives fed by voltage source inverters usually the Pulse Width Modulation (PWM) is used in the control electronics to calculate the switching instants of the power semiconductor switches. One very common method of modulation is the so-called space phasor or vector modulation, which is well described in the standard literature e.g. [63] and [104]. The technique of the space phasor modulation was used for the calculation of the switching signals of the inverter in the experimental set-up.

## 2.3 Silicon Carbide semiconductors

### 2.3.1 Special features of silicon carbide switches

Silicon Carbide switches have four main advantages:

- **Higher Thermal Conductivity:** SiC presents a higher thermal conductivity up to 3 times in contrast with silicon. Thus, the heat produced by the losses are conducted through the semiconductor in a better way and the temperature drop in the semiconductor material is reduced.



- Higher Operating temperature: SiC has a high melting temperature as well. Therefore, devices with such technology operate perfectly on a temperature that reaches 400°C, unlike the standard silicon that maximally runs on a temperature that extends to 150°C only.
- Higher Current Density: SiC exhibits a current density that exceeds the silicon current density level 2 to 3 times.
- Faster Switching Frequency: SiC technique exhibits a faster switching frequency, and thus, a small dead time rises. However, this feature has been taken as a disadvantage since it affects the quality of the current.

Regarding the switching frequency, the Silicon Carbide switches are able to be operated at higher switching frequencies up to 100 kHz or more. Based on these superior properties, high-speed switching operation can be achieved in the switches structures that place priority on operating speed. The reverse recovery current of the Silicon Carbide Schottky diode remains constant, with almost no matter how much the temperature increases, this minimizes the reverse recovery charge and contributes to the reduction of switching losses. While in the silicon diode, the reverse recovery current increases with temperature, this will lead to increase the switching losses [98].

A dramatical reduction of power losses appears in inverters when using silicon carbide switches, comparing with that one using Si switches [99] in Figure 2-8 which is clearly shows that the reduction of the power losses reaches up to 73% [99].

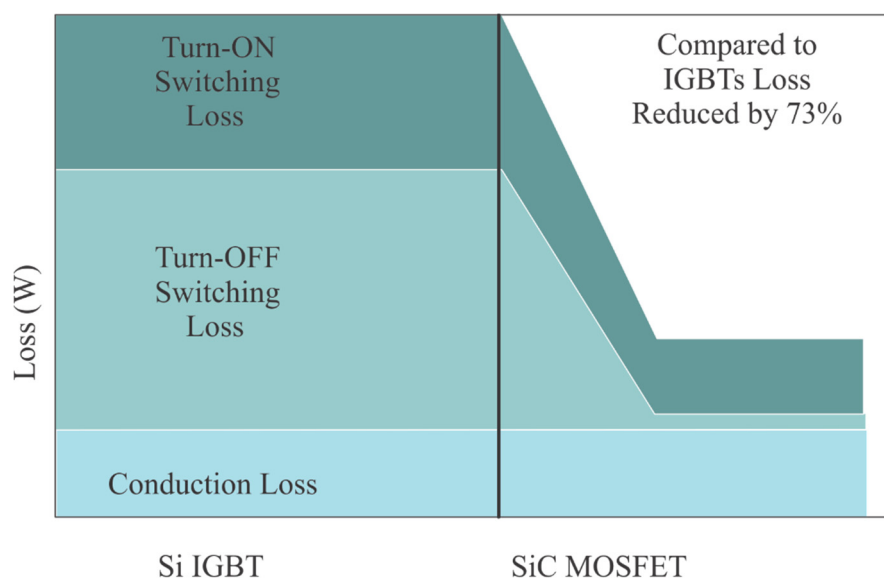


Figure 2-8 Loss comparison of SCH2080KE SiC-MOSFET+ Schottky Barrier Diode (SBD) and Si-IGBT

### 2.3.2 Silicon carbide MOSFET based inverter

Conventional Si-MOSFET or IGBTs are currently the most widely used semiconductor switches in inverters. Si-MOSFET exhibit switching frequency in tens and hundreds of kHz are easy to apply, e.g. in low voltage, computer type power supplies, which run in the kHz of switching frequency range. On the other hand, conventional Si- MOSFET have the disadvantage of on-resistance, which increases rapidly with the rated blocking voltage. The Si-MOSFET featuring blocking voltage of 600V, 1200V, or even more, have been costly and are available only in limited amounts [70]. Presently Silicon Carbide MOSFETs are available with blocking voltages equal to 1200V, (and on-resistance equal to 80 mohm) which is ideal for applications like voltage source inverters [70].

The Silicon Carbide MOSFET module which has been selected in this work a CCS020M12CM2 SiC MOSFET Six-Pack (three-phase) Module 1,2kV/20A of CREE due to their suitability in dealing with the design characteristics required and specified for this object, Figure 2-9.



Figure 2-9 CCS020M12CM2 SiC MOSFET Cree module

### 2.3.3 Dead-time effect

Conventional inverters equipped with silicon power switches demand a long dead time that reaches up to 3  $\mu$ s in order to avoid a short through the legs of the inverter. Due to this delay the output voltage is distorted. If this effect is not compensated for in the model, the reference signals for the voltage cannot be used for feeding a model. Conversely, the dead time in case of the SiC MOSFET inverter can be reduced down to 250 ns or even less.

The high switching frequency of the inverter can be advantageous if the output voltages are appropriately filtered and become rather sinusoidal. These switched output voltages of the inverter can be converted into almost sinusoidal waves by passing through a small LC filter inserted between the SiC-inverter and the three-phase load.

In this way, some negative effects of the non-sinusoidal voltage can be attenuated but in addition to that, it is expected that the performance of a sensorless control that uses the measured voltage instead the calculated one can also become better.

#### **2.3.4 Considerations for the design of an inverter with SiC modules**

For minimizing the parasitic effects in SiC MOSFET inverters, some consideration have to be taken into account; among others the design of the layout of the printed circuit board (PCB) has to be carefully examined.

A suitable layout of the printed circuit board contributes essentially to decreasing the parasitic inductance and guarantees transient voltage the maximum rated blocking voltage of the semiconductor switches [100]. In this work, following manufacturer's recommendations, a multilayer printed circuit board, designed with four layers was used; the top layer is connected to the negative pole of the DC link, while the middle two layers are connected to the middle point of the capacitor bank and the whole bottom layer to the positive pole of the DC Link. The main objective of this structure is to minimize the parasitic inductance. To mitigate this effect, the magnetic field canceling technique is used, as illustrated in Figure 2-10 [101]. This structure makes the track of the current loops short by making the entire pins of the two series capacitors connected to the middle layers, and the outer two pins of the series capacitors are connected to the + DC LINK layer and – DC LINK layer. The current track loop is illustrated with the dashed black line [101].

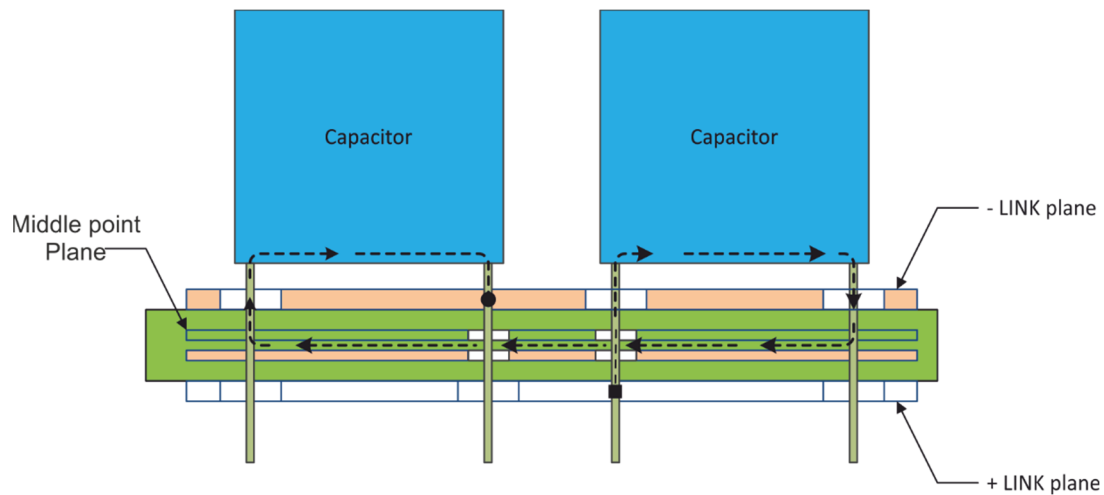


Figure 2-10 Schematic of the magnetic field cancelation

In addition to that, connections from each pair of the capacitors is suggested in [101]. In this manner, as shown in Figure 2-11 and Figure 2-12, the current in the path through the parallel capacitor arrays is flowing in inverse directions in order to reduce or cancel the field. The current paths through each series connected couples of capacitors are illustrated by black arrows.

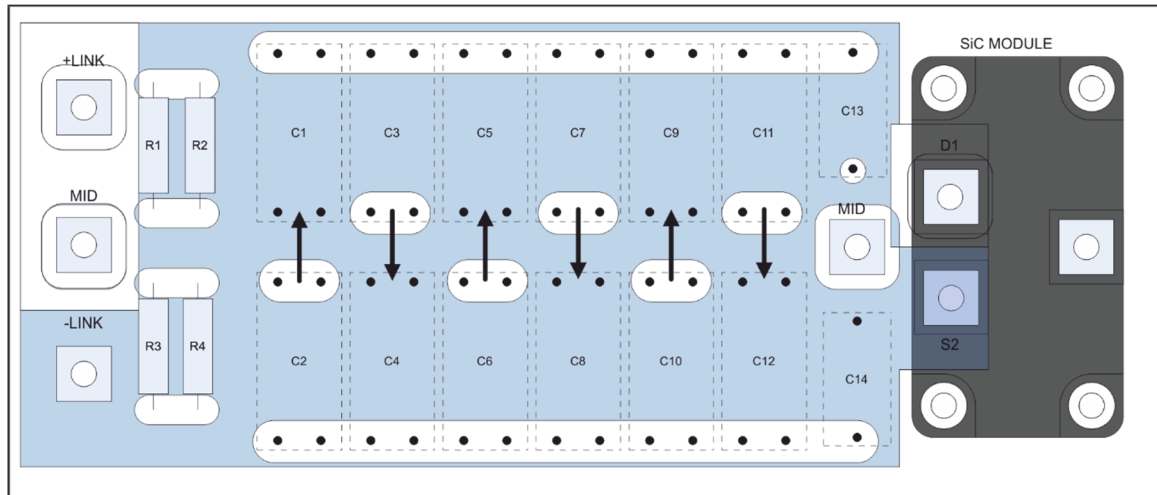


Figure 2-11 Magnetic field cancellation applied to the parallel rows of capacitors. -DC  
Link Layer

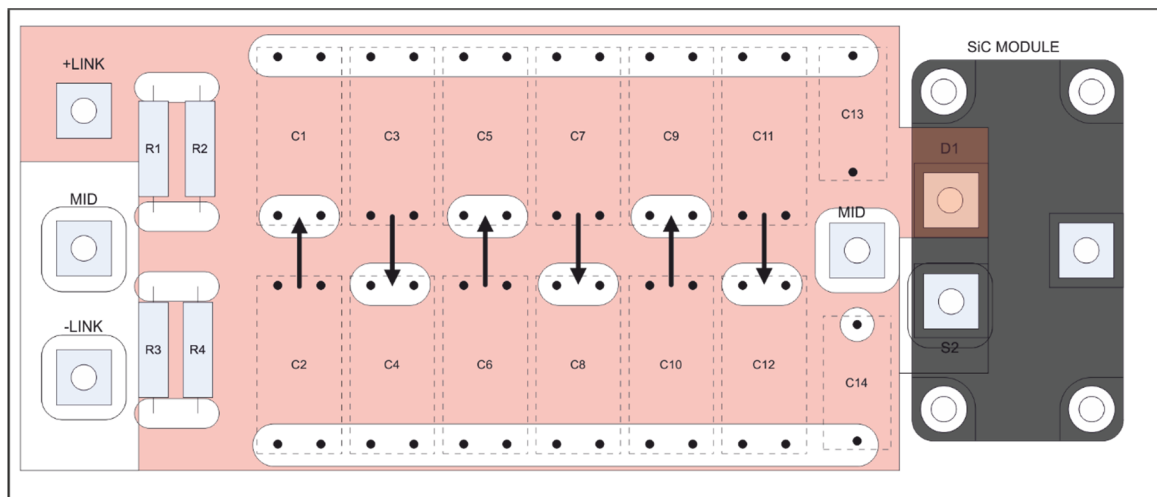


Figure 2-12 Magnetic field cancellation applied to the parallel rows of capacitors. +DC  
Link Layer

## 2.4 Design of the inverter output filter

The installation of a small LC filter to be connected between the fast switching-type inverter and the three-phase induction machine, has several advantages [97]. It protects the motor winding insulation against  $dv/dt$  and voltage spikes and reduces:

- the additional magnetic losses and eddy current losses in the motor,
- the motor heating,
- the motor bearing currents caused by circulating currents,
- the acoustic noise of the motor and
- the electromagnetic emissions of the motor cables

and delivers a filtered almost sinusoidal voltage that can be easily measured and used for the control of a drive.

In the present work, an LC-filter with the topology depicted in Figure 2-13 was designed.

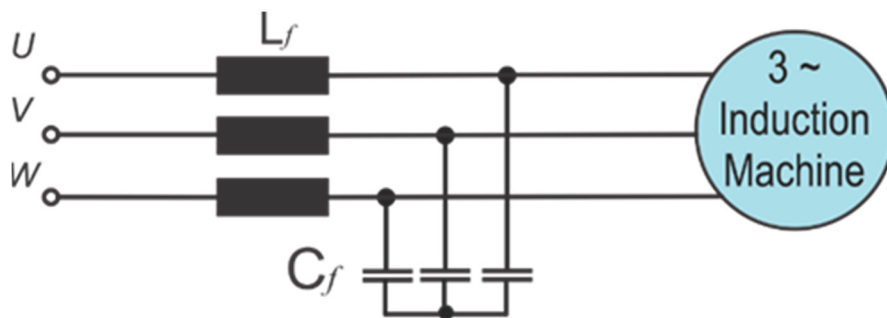


Figure 2-13 Filter topology

The circuit in Figure 2-14 and Figure 2-15 is obtained in the case of using active voltage vector. For example, in the case of (+--), the positive pole of the voltage of the DC link is connected to output phase  $U$ , and the negative pole is connected to both output of the other phases  $V$ ,  $W$ . For the high switching frequency, the reactance of the total leakage inductance of the motor, which referred to the stator side, is much larger than the reactance of capacitors, so it can be neglected.

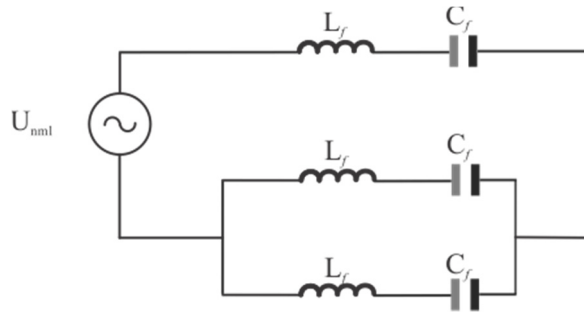


Figure 2-14 The equivalent circuit of the inverter connected with the sinusoidal filter

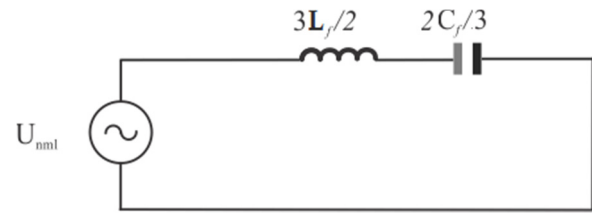


Figure 2-15 Compressed the equivalent circuit of the inverter connected with the sinusoidal filter

The values of inductance and capacitance in the equivalent circuit are  $3L_f/2$  and  $2C_f/3$ , respectively. At high switching frequency ( $f_{ws}$ ) up to (50 kHz), the reactance of inductance components  $L_f$  is much larger than reactance of the capacitors  $C_f$ . Thus the inductor that determines the ripple and it is possible to have [97] [100]:

$$2 \cdot \pi \cdot f_{sw} \cdot \frac{L_f}{2} \cdot \Delta I = \frac{U_{dc}}{\sqrt{2}} \quad (2.30)$$

So

$$n \quad (2.31)$$

The value of the capacitor  $C_f$  results from the resonant frequency of the system:

$$f_{res} = \frac{1}{2\pi \cdot \sqrt{L_f \cdot C_f}} \quad (2.32)$$

And

$$C_f = \frac{1}{4 \cdot \pi^2 \cdot f_{res}^2 \cdot L_f} \quad (2.33)$$

The smaller current ripple on the inverter output, as well as on the filter input, can be achieved by using a large value of inductance  $L_f$  that increases the cost, weight and volume. On the other hand, the larger current ripple may cause higher losses in the filter due to the loss generated in the iron core. Figure 2-16 shows the relationship between  $L_f$  and  $\Delta I$ , where  $L_f$  in mH

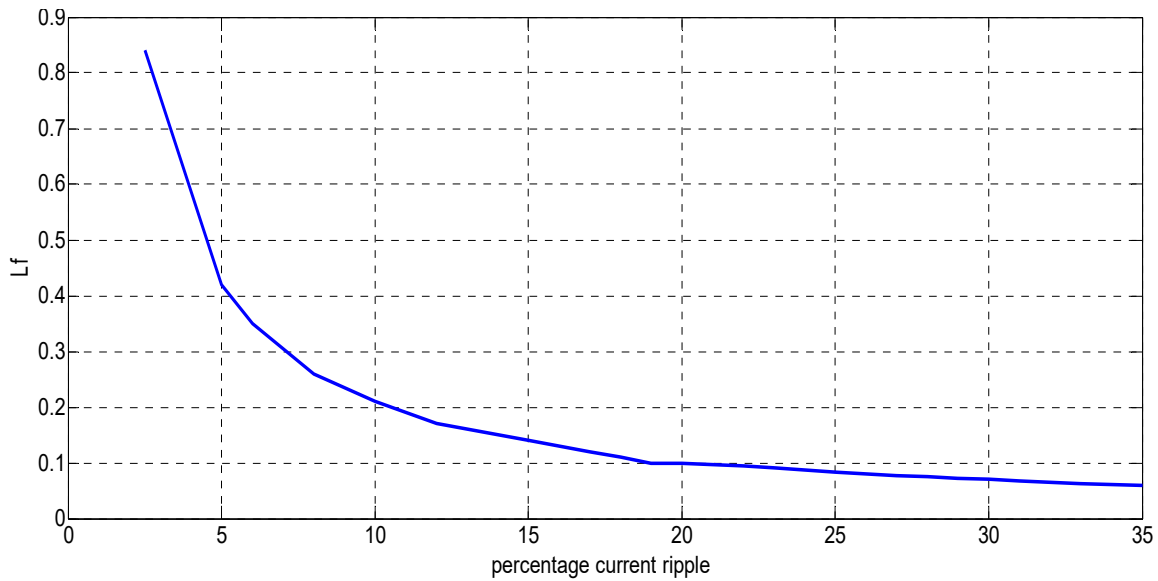


Figure 2-16 Required inductance value in relation to current ripple on the inverter output

## 2.5 Summary of the chapter

This chapter contains the basic concepts that are used in this work. First, the well-known mathematical model of a squirrel cage induction machine that uses complex space phasor equations is presented. As a second topic, the basic topology of the conventional two-level voltage source inverter with its basic description is briefly explained.

In addition the benefits of silicon carbide semiconductor switches are discussed as they are an important element of this work. A section is dedicated to design considerations for the inverter layout and for the small LC filter that is connected between the fast switching-type inverter and the three-phase induction machine (IM).



# 3 Control of the Induction Machine

## 3.1 Introduction

Induction machines are highly reliable, low cost and often the first choice in industrial equipment and in general automation, yet its control is not straightforward and complex in the implementation. In the last decades a lot of effort was dedicated to the development of suitable control schemes with and without mechanical encoder for the measurement of the shaft position [102] [103] and [104].

Figure 3-1 shows the control methods for the induction machines, which are mostly accepted and widely used. These control methods can be generally classified into two classes, the scalar control that is widespread, and the space phasor control, both of them will be explained in the next sections [105] [28] [106].

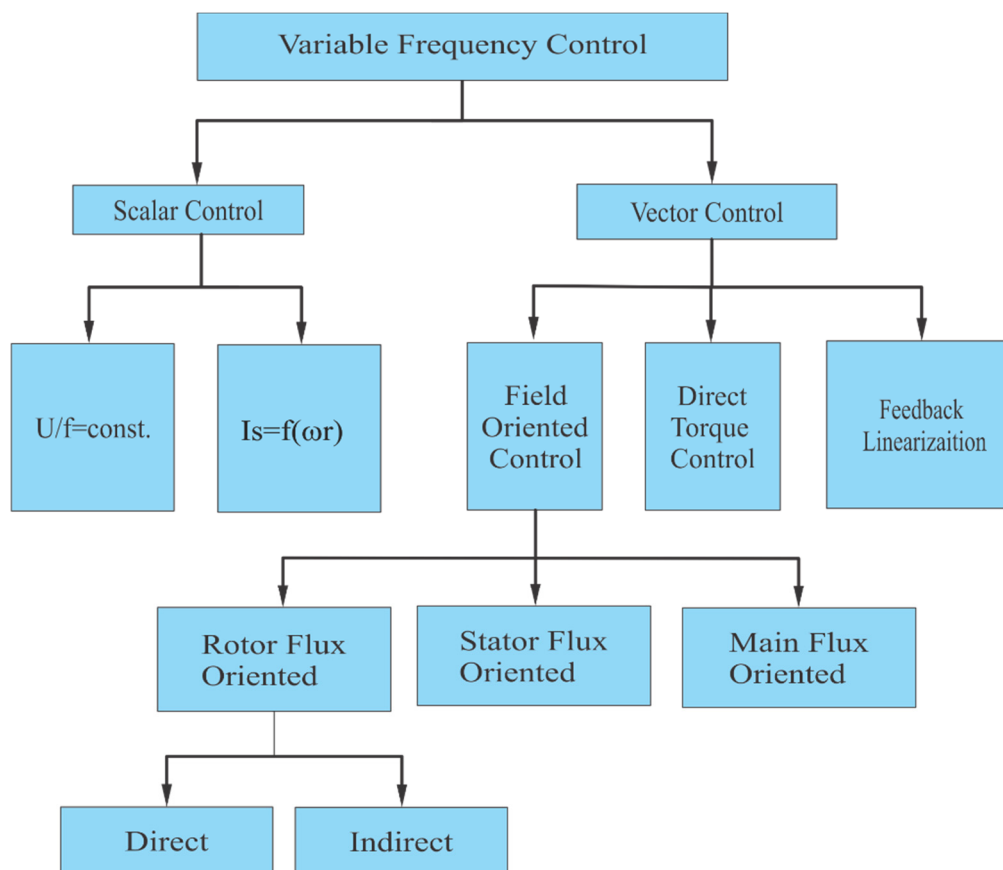


Figure 3-1 Simple classification of the induction machine control theories

The scalar control is a very simple method and, as its name suggests, it deals with scalar quantities namely the magnitude of the controlled variables. Scalar control is easily implemented and therefore very popular because it is inherently sensorless i.e. they can be realized without any sensor for the shaft position. Such schemes offer an acceptable steady state behavior, however they provide an unsatisfactory performance during the transient state especially at low operation speeds. In many applications, a behavior similar to the operation on the grid, and with constant maximum torque, regardless of the stator frequency is desired. This can be obtained if the air gap flux is kept more or less constant; this condition becomes true so long as the ratio between the stator voltage and stator frequency remains fixed. Scalar control schemes can be enhanced through modifications: the feedback of the measured variables, or introducing external current controllers. Yet the transient performance is not appropriate for applications that demand a good control of the torque in the full velocity range.

The second category of control schemes comprises the methods that apply a vectorial approach, and lead to an excellent dynamic behavior of the drive in high performance applications. A fast torque response, an excellent transient behavior, and a suitable steady state, are characteristic of this type of control. As is well-known in the control of DC machines, the field current and the corresponding main flux, as well as the armature current and thus the torque, are both separately controlled and orthogonal variables. Hence, at least theoretically, they do not influence each other. The same objective is targeted for the AC machines; therefore, an independent control of the magnetization and torque of the machine has to be achieved. Results presented in this work were obtained with field oriented control, and thus other methods will not be discussed. . Blaschke [9] and Hasse [8] were pioneers in the 70's in this regard, and proposed independently of each other a vectorial control scheme that fulfills these requirements; a deeper review of the field oriented control can be found in the next subchapter.

### 3.1.1 Principle of the Field Oriented Control

Analogous to the control of a separately excited DC machine, the reference frame is aligned to one of the rotating flux space phasors. This becomes particularly advantageous because firstly, all variables become DC-quantities in steady state and secondly, the equations are greatly simplified. The alignment with the rotor flux space phasor, rather than with the space phasor of the stator flux or of the air-gap flux, brings the simplest expression for the torque. Figure 3-2 depicts the orientation of the reference

frames, defining the angle  $\varphi_2$  between the fixed stator real axis and the rotor flux space phasor, which in turn, is aligned with the real axis of the field coordinate system.

A magnetizing current space phasor that is proportional to the stator flux phasor is defined as:

$$\underline{i}'_{\mu 2} = \frac{\underline{\Psi}'_2}{L_{1h}} = \frac{|\underline{\Psi}'_2|}{L_{1h}} \cdot e^{j\varphi_2} \cdot e^{j\gamma_1} \quad (3.1)$$

and after the bringing together the reference axis with the rotor flux space phasor, the following relations are valid:

$$\varphi_2 = -\gamma_1, \gamma = \gamma_2 - \gamma_1, \gamma_2 = \gamma + \gamma_1 = \gamma - \varphi_2, \dot{\gamma}_2 = \dot{\gamma} + \dot{\gamma}_1 = \dot{\gamma} - \dot{\varphi}_2 \quad (3.2)$$

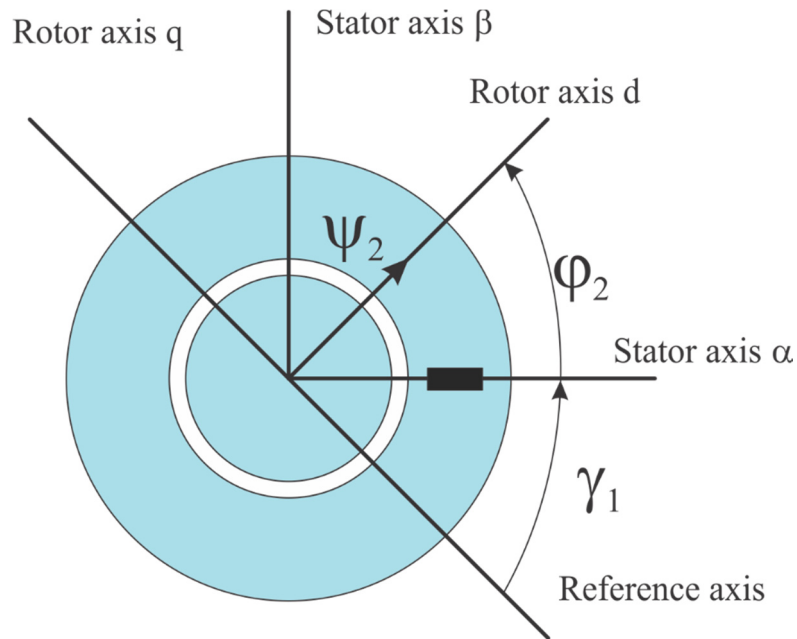


Figure 3-2 Definition of the reference angles

Then the voltage equation of the squirrel-cage rotor becomes:

$$0 = R_2 \cdot \underline{i}'_2 - j \cdot \dot{\gamma}_2 \cdot \underline{\Psi}'_2 + \frac{d\underline{\Psi}'_2}{dt} \quad (3.3)$$

$$0 = R_2 \cdot \dot{i}'_2 + j \cdot (\dot{\phi}_2 - \dot{\gamma}) \cdot \psi'_2 + \frac{d\psi'_2}{dt} R \quad (3.4)$$

$$0 = R_2 \cdot \dot{i}'_2 + j \cdot (\dot{\phi}_2 - \dot{\gamma}) \cdot i_{\mu 2} L_{1h} + \frac{di_{\mu 2}}{dt} \cdot L_{1h} \quad (3.5)$$

with

$$\dot{i}'_2 \cdot (1 + \sigma_2) = \frac{1}{L_{1h}} \cdot (\psi'_2 - L_{1h} \cdot \dot{i}_1) \quad (3.6)$$

$$\dot{i}'_2 = \frac{1}{1 + \sigma_2} \cdot \frac{(\psi'_2 - L_{1h} \cdot \dot{i}_1)}{L_{1h}} = \frac{1}{1 + \sigma_2} \cdot (i_{\mu 2} - \dot{i}_1) \quad (3.7)$$

follows from (3.5)

$$0 = \frac{R'_2}{1 + \sigma_2} \cdot (i'_{\mu 2} - \dot{i}_1) + j \cdot (\dot{\phi}_2 - \dot{\gamma}) \cdot i'_{\mu 2} \cdot L_{1h} + \frac{di'_{\mu 2}}{dt} \cdot L_{1h} \quad (3.8)$$

$$0 = \frac{R'_2}{L'_2} \cdot (i'_{\mu 2} - \dot{i}_1) + j \cdot (\dot{\phi}_2 - \dot{\gamma}) \cdot i'_{\mu 2} + \frac{di'_{\mu 2}}{dt} \quad (3.9)$$

introducing the rotor time constant:

$$\tau_2 = \frac{L'_2}{R'_2} \quad (3.10)$$

$$\tau_2 = \frac{di'_{\mu 2}}{dt} + i'_{\mu 2} = \dot{i}_1 - j \cdot (\dot{\phi}_2 - \dot{\gamma}) \cdot \tau_2 \cdot i'_{\mu 2} \quad (3.11)$$

and separating into its real and imaginary parts  $\dot{i}_1 = i_{1d} + j \cdot i_{1q}$  :

$$i_{\mu 2} + \tau_2 \cdot \frac{di_{\mu 2}}{dt} = i_{1d} \quad (3.12)$$

$$0 = i_{1q} - (\dot{\phi}_2 - \dot{\gamma}) \cdot \tau_2 \cdot i_{\mu 2} \quad (3.13)$$

and

$$M_i = \frac{3}{2} \cdot p \cdot \frac{1}{1 + \sigma_2} \cdot \text{Im} \{ \underline{\Psi}_2^* \cdot (i_{1d} + j \cdot i_{1q}) \} = \frac{3}{2} \cdot p \cdot \frac{1}{1 + \sigma_2} \cdot |\underline{\Psi}_2| \cdot i_{1q} \quad (3.14)$$

From Equation (3.12) it is easy to observe a first order delay relation between the magnetizing current and the real component of the stator current space phasor. By modifying  $i_{1d}$ , it is possible to affect the magnitude of the rotor flux and, in turn, the magnetizing state of the machine; that is why  $i_{1d}$  is often called the flux producing component of the current space phasor. Concerning the imaginary part of the rotor voltage equation (3.13), it is possible to deduce that by a constant flux, the q-component of the current is proportional to the angular frequency  $(\dot{\varphi}_2 - \dot{\gamma})$ , which describes the rotation of the rotor flux space phasor relative to the rotor and corresponds in steady state to the rotor frequency  $\Omega_2 = \Omega_1 - \dot{\gamma}$ . As the q-component of the stator current (by constant flux) is proportional to the developed torque,  $i_{1q}$  is often called the torque producing component.

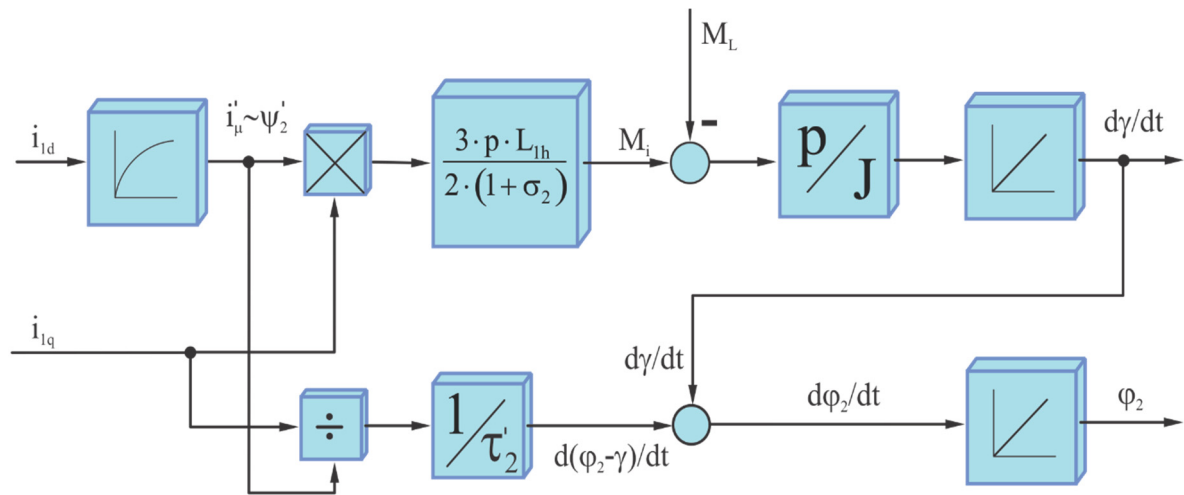


Figure 3-3 Block diagram showing of the induction machine in d,q-coordinates

As mentioned before, this control technique employs a rotating reference frame linked to the rotor flux space phasor; therefore it is mandatory to know its orientation, here represented as  $\varphi_2$ , with respect to the real axis of the alpha-beta reference frame. In the next section, some mathematical solutions to obtain this angle will be explained, as well as their advantages and limitation

### 3.2 Sensorless speed control of an induction machine

As already mentioned, appropriate control properties may be achieved when a field orientation control scheme is used in induction machine drives. Therefore, the field oriented control (FOC) is currently considered an industry standard. In the case of the induction machine, for the implementation of the FOC all the machine state variables have to be transformed into a coordinate system, which rotates synchronously with the rotor flux phase phasor [107]. For this purpose, the information of the rotor position has to be instantaneously available for the control. Position sensors, like incremental encoders and resolvers, are commonly used for determining the rotor position and are widely used in drive technology. However, they require an additional cabling between the motor and the control unit (as the well as corresponding hardware costs) which has to ensure reliable transmission and evaluation of the encoder signals.

In many applications however, the waiver of the position encoder is required due to several aspects of operation:

- For industrial applications with low demands on the dynamics or the positioning accuracy, low cost systems are preferred and the cost of the encoder can be a determining factor.
- In applications that cover a high-speed range, the encoder can also become too expensive.
- In direct drives, where the motor without a gearbox is directly coupled to the driven machine, a special encoder is required and a sensorless control can be advantageous.
- The integration of an encoder into a motor requires leads to a larger overall length. Thus a motor without an encoder results in a compact drive system with lower volume and overall length.
- Environmental conditions ( shock, vibration or aggressive atmosphere) can require a system without a mechanical position encoder [108].

Regarding the advantages that result from a control scheme without an encoder, in the last decades a lot of effort in different research groups was dedicated to the development of methods that allow the identification of the rotor position and the speed based on the measurement of the terminal voltage and current. These procedures are known in the pertinent literature as "Sensorless Control ", but the sensors for current detection and voltage measurement still exist. Despite the volume of relevant research, there was no

standard solution for sensorless control of induction machines in a wide speed range, including zero speed, until now. The reason for this lack of a general solution is the fact that the evaluation of the physical effects of the rotor angle determination is dependent on the respective operating state of the machine. Above all, the rotor angle determination at low speed or at a standstill is problematic, since the reaction of the rotor position to the measured stator magnitudes is small or zero because the voltage is induced proportionally to the rotational speed.

Under these circumstances, other methods are needed by which the rotor position can be determined from the evaluation of speed-independent effects of the machine.

As illustrated in last section, the stator flux space phasor  $\Psi_1$  of the machine can be calculated by using the voltage model without an encoder, so long as the machine's rotational speed is above a minimum value (3% of rated speed), or only rotates for a short time in the low rotational speed range. On the other hand, with the use of the voltage model, long-time rotation at low rotational speed is not possible. Thus, some of the control methods, which are called fundamental wave models, are described, specifically those that require the information of the stator flux space phasor, to operate at least at higher rotational speed without an encoder [25].

### 3.2.1 Classification of sensorless control

An accepted classification of the known methods of sensorless control, is well presented in [25], [109] and [110] as shown in Figure 3-4.

The fundamental wave models use the classical dynamic models of the induction machine, which assumes that a sinusoidal flux density is distributed in the air gap. The fundamental wave models are only valid at high stator frequency because the system becomes unobservable at zero stator frequency and the induced stator voltages become almost zero [25], [108].

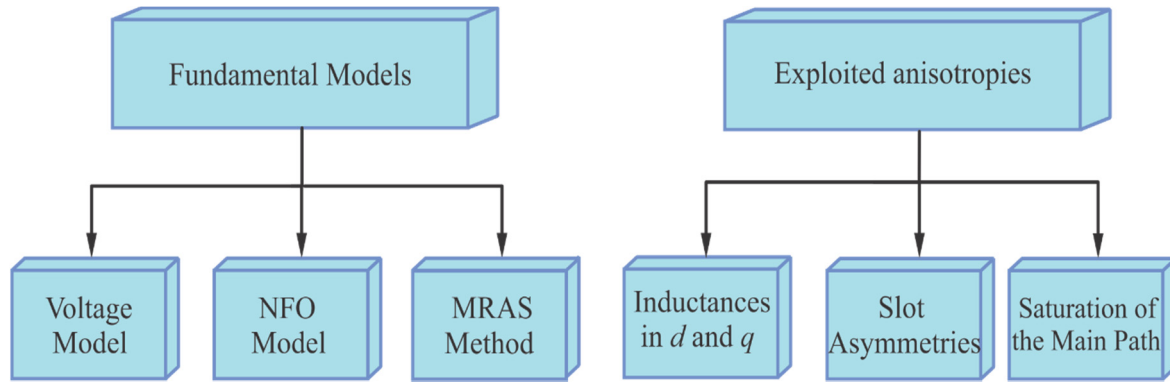


Figure 3-4 Classification of the sensorless methods

The fundamental field wave model sensorless control method uses either a voltage model [111] [112], state observers [113] [114] or Kalman filters [115] [116] for the estimation of the field angle.

As stated in [108], a minimum stator frequency range of a stable operation is between 0.25 – 1.05 % of the nominal speed. However, in experimental applications, these models fail at higher levels; between 3 – 5 % of the nominal speed of the stator frequency [117] [118]. Therefore, usually at the low-speed range, other methods have to be used for the precise operation of the drive.

Figure 3-4 also describes the second group of sensorless methods, which exploits anisotropies of the machine for the identification of the desired angular position. In all types of electrical machines there are always parasitic secondary effects, which are not considered in their fundamental model. These include saturation effects, stator slotting effects or rotor eccentricity. These effects give rise to local anisotropic magnetic machine properties which can be used to excite rotor position by excitation with a suitable test signal. A general structure for all sensorless methods in both fundamental wave models and exploited anisotropies category are depicted in Figure 3-5 [25].



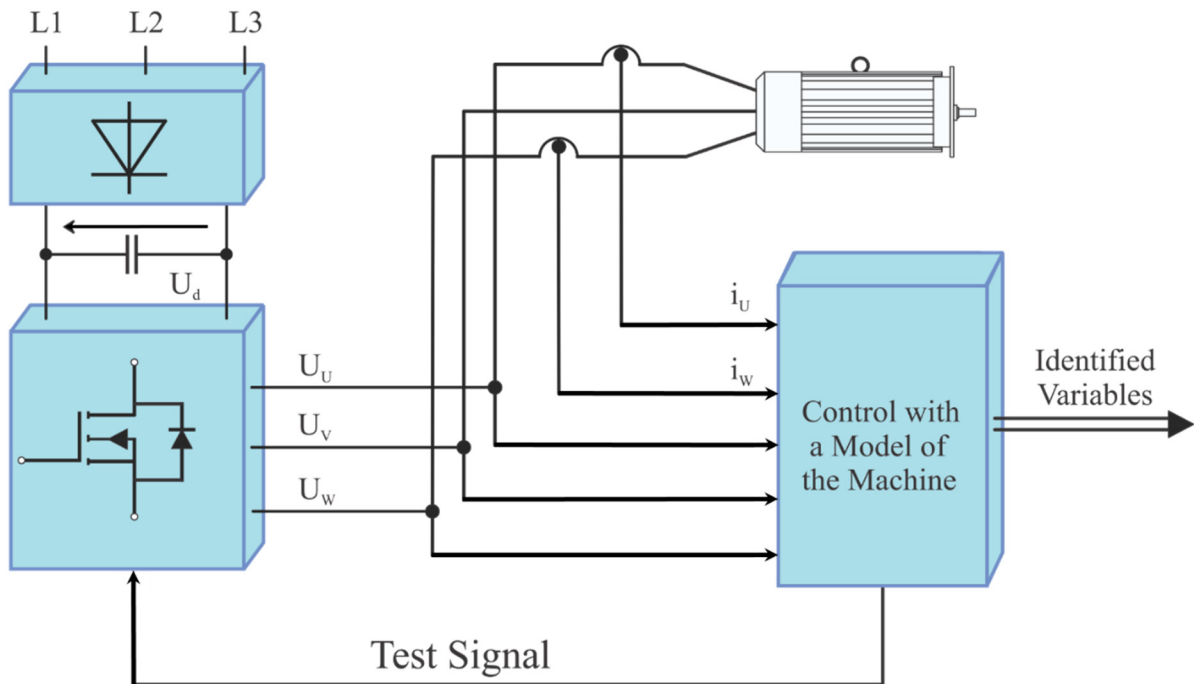


Figure 3-5 Main configurations of a sensorless control

### 3.2.2 Principal fundamental wave models

As already stated, the FOC of the induction machine requires the knowledge of the angular position of the rotor flux space phasor that can be obtained from a model of the machine to be integrated in the control scheme. In encoder-less operation, the models may only depend on the electrical measurable terminal currents and voltages to calculate the magnetic flux space phasor. In an operation with encoder, the mechanical speed can be included in the calculation as well. Two possible models for calculating the position of the rotor flux space phasor are widespread and well-known; the voltage and the current model that are explained in the following.

#### 3.2.2.1 Current model

A current model is a simple approach that is widely used for obtaining the angle of the rotor flux space phasor. By employing the rotor angular position in addition to the measured stator currents, the rotor flux space phasor angle can be obtained. The rotor angular position can be measured by using an encoder attached to the rotor shaft of the induction machine, and for the stator currents; two phases at least must be measured [5]

The model relies on the rotor voltage equation in field oriented coordinates (3.4):

$$0 = R_2 \cdot \underline{i}'_2 + j \cdot (\dot{\varphi}_2 - \dot{\gamma}) \cdot \underline{\psi}'_2 + \frac{d\underline{\psi}'_2}{dt}$$

From (3.13) follows for the rotor flux space phase angle:

$$\varphi_2 = \int \left( \dot{\gamma} + \frac{i'_{1q}}{i'_\mu \tau_2} \right) dt = \int \dot{\gamma} dt + \int \left( \frac{i'_{1q}}{i'_\mu \tau_2} \right) dt = \gamma + \int \left( \frac{i'_{1q}}{i'_\mu \tau_2} \right) dt \quad (3.15)$$

By using  $i'_{1d}$  and the rotor time constant  $\tau_2$ , the magnetizing current  $i'_{\mu 2}$  could be calculated as:

$$i'_{\mu 2} + \tau_2 \cdot \frac{di'_{\mu 2}}{dt} = i'_{1d} \quad (3.16)$$

The current model delivers implicit equations for the angle  $\varphi_2$  and the magnetizing current  $i'_{\mu 2}$ , which are depicted in Figure 3-6 starting with the three to two phase transformation,  $i_\alpha$  and  $i_\beta$  are obtained. Afterwards a second transformation is accomplished with the help of the angle  $\varphi_2$  that is supposed to be known:

$$i'_{1d} = i'_{1\alpha} \cdot \cos(\varphi_2) + i'_{1\beta} \cdot \sin(\varphi_2) \quad (3.17)$$

$$i'_{1q} = i'_{1\beta} \cdot \cos(\varphi_2) - i'_{1\alpha} \cdot \sin(\varphi_2) \quad (3.18)$$

The currents  $i_d$  and  $i_q$  obtained in this way are processed and deliver the magnitude and angle of the rotor flux space phasor. To complete the model, the stator flux space phasor can be expressed in its complex form as:

$$\underline{\Psi}_1 = \underline{i}_1 \cdot \left( L_1 - \frac{L_{1h}^2}{L_2} \right) + \underline{\Psi}'_2 \cdot \left( \frac{L_{1h}}{L_2} \right) \quad (3.19)$$

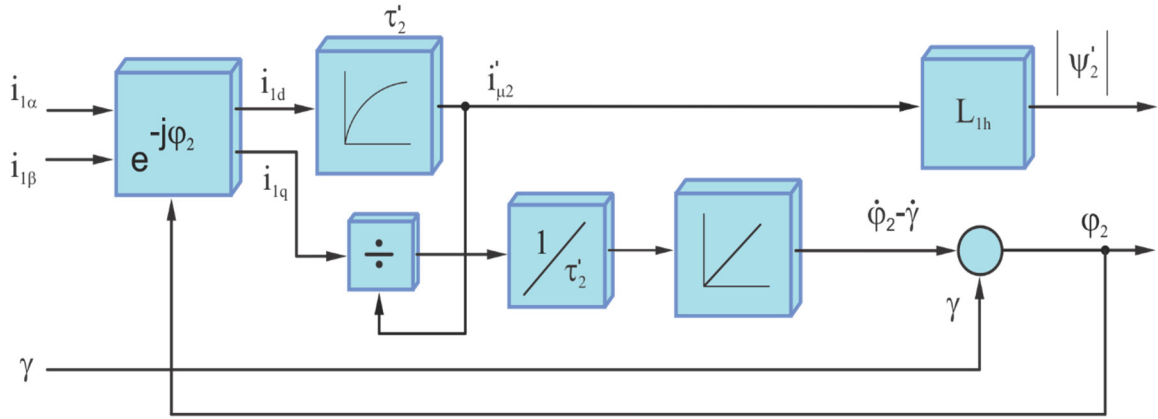


Figure 3-6 Block diagram of the current model

The main advantage of the current model is that it can be operated in the whole velocity range. In addition, in this model there are no open integrators and the first order delay relation between the input  $i_{1d}$  and output  $i_{\mu 2}'$  variables is very easy to be realized and does not yield any numerical problems.

However, two main disadvantages accompany the current model, the first one denoted by the sensitivity of the current model due to the parameters of the machine, where the temperature changes of the rotor significantly modify the value of the rotor time constant  $\tau_2'$  and that an additional sensor is needed for the measurement of the mechanical angle  $\gamma$ . Nevertheless, changes of the mutual inductance  $L_{1h}$  due to the saturation of the main path can be compensated taking into account the magnetizing curve of the machine, yet the changes in rotor resistance  $R_2'$  are not easy to be considered. The second big drawback is represented by the additional speed sensor for obtaining the position that is reducing the reliability of the system and increasing the cost.

### 3.2.2.2 Voltage model

The so called voltage model is a simple approach for the calculation of the stator and of the rotor flux space phasor without any additional speed sensor based only on the measurement of the terminal stator voltages and currents. Due to its simplicity and to the fact that only the stator resistance is the important parameter of this model, and the saturation of the main path affects its performance, it is widespread in industrial applications. The operation of this model can be explained by using the stator voltage equation:

$$\underline{u}_1 = R_1 \cdot \underline{i}_1 + \underline{\dot{\psi}}_1 + j \cdot \dot{\gamma} \cdot \underline{\psi}_1 \quad (3.20)$$

In a  $\alpha$  and  $\beta$  coordinate system fixed to the stator  $\dot{\gamma}_1 = 0$  the complex equation can be expressed in its real and imaginary parts:

$$u_{1\alpha} = R_1 \cdot i_{1\alpha} + \frac{d\psi_{1\alpha}}{dt} \quad (3.21)$$

$$u_{1\beta} = R_1 \cdot i_{1\beta} + \frac{d\psi_{1\beta}}{dt} \quad (3.22)$$

The stator flux space phasor can be written as:

$$\underline{\psi}_1 = \int (\underline{u}_1 - R_1 \cdot \underline{i}_1) dt \quad (3.23)$$

The components of the stator flux space phasor in  $\alpha, \beta$ -coordinates can be expressed as:

$$\psi_{1\alpha} = \int (u_{1\alpha} - R_1 \cdot i_{1\alpha}) dt \quad (3.24)$$

$$\psi_{1\beta} = \int (u_{1\beta} - R_1 \cdot i_{1\beta}) dt \quad (3.25)$$

Herein  $u_{1\alpha}, u_{1\beta}, i_{1\alpha}, i_{1\beta}, \psi_{1\alpha}, \psi_{1\beta}$  are the  $\alpha, \beta$ -components of the stator voltage, stator current, and stator flux space phasors respectively,  $R_1$  is the resistance of the stator winding.

As it will be explained in a later section, the integrators in (3.24) and (3.25) are implemented as first order lag or as band-pass in order to avoid a drift at low frequencies of operation.

The rotor flux space phasor can be calculated from the stator flux space phasor by using the machine equations as follows:

$$\underline{\psi}'_2 = \frac{\sigma}{\sigma - 1} \cdot L_{1h} \cdot \underline{i}'_1 + (1 + \sigma_2) \cdot \underline{\psi}_1 \quad (3.26)$$

and if it is decomposed into its  $\alpha$ - and  $\beta$ - components:

$$\psi'_{2\alpha} = \frac{\sigma}{\sigma - 1} \cdot L_{1h} \cdot i'_{1\alpha} + (1 + \sigma_2) \cdot \psi_{1\alpha} \quad (3.27)$$

$$\psi'_{2\beta} = \frac{\sigma}{\sigma-1} \cdot L_{1h} \cdot i_{1\beta} + (1 + \sigma_2) \cdot \psi_{1\beta} \quad (3.28)$$

and for the angular position of the rotor flux space phasor:

$$\varphi_2 = \arctan\left(\frac{\psi'_{2\beta}}{\psi'_{2\alpha}}\right) \quad (3.29)$$

The main advantages of the voltage model is that  $\varphi_2$  the angular position of the rotor flux space phasor can be determined by only using the stator voltages and currents of the machine. Although the  $R_1$  changes with the temperature, its variation can be easily compensated.

In the conventional voltage source inverters (VSI), the output voltages are pulsating and not sinusoidal functions, therefore instead of the measured voltages the synthetic functions calculated by the PWM are assumed to be the stator voltages and then fed to the integrators in the model. In addition, two phase currents are measured and sampled to complete the input variables. As explained above the stator resistance has an influence on the overall performance of the model; temperature variations modify the value of  $R_1$  but they can be compensated, the saturation has only a minor impact on the model as it appears multiplied with the leakage coefficient. If necessary, the saturation of the main air gap inductance can be corrected by using the measured magnetization characteristic. Figure 3-7 shows the block diagram of the standard voltage model (SUM).

### 3.2.2.3 Enhanced voltage model (EUM)

It is well known that the standard voltage model presented in the last section works only until a minimum stator frequency. An enhancement of the voltage model is depicted in Figure 3-7. This model is used for the identification of the rotor flux space phasor. One of the objectives of the present work is to examine the possible enhancement of the voltage model if the measured voltages are used instead of the reconstructed ones. In Figure 3-7, the voltage model fed with the reference values of the voltages (with an asterisk) is called the standard (SUM), whereas the enhanced one that fed with the measured terminal voltages of the machine (without an asterisk) is called the enhanced voltage model (EUM). The enhanced voltage model is the model that is fed by the measured voltages is applied to the machine after the LC filter. It is expected that due to the smooth

waveform of the measured sinusoidal voltage, the sensorless control can be operated in an extended range of speed.

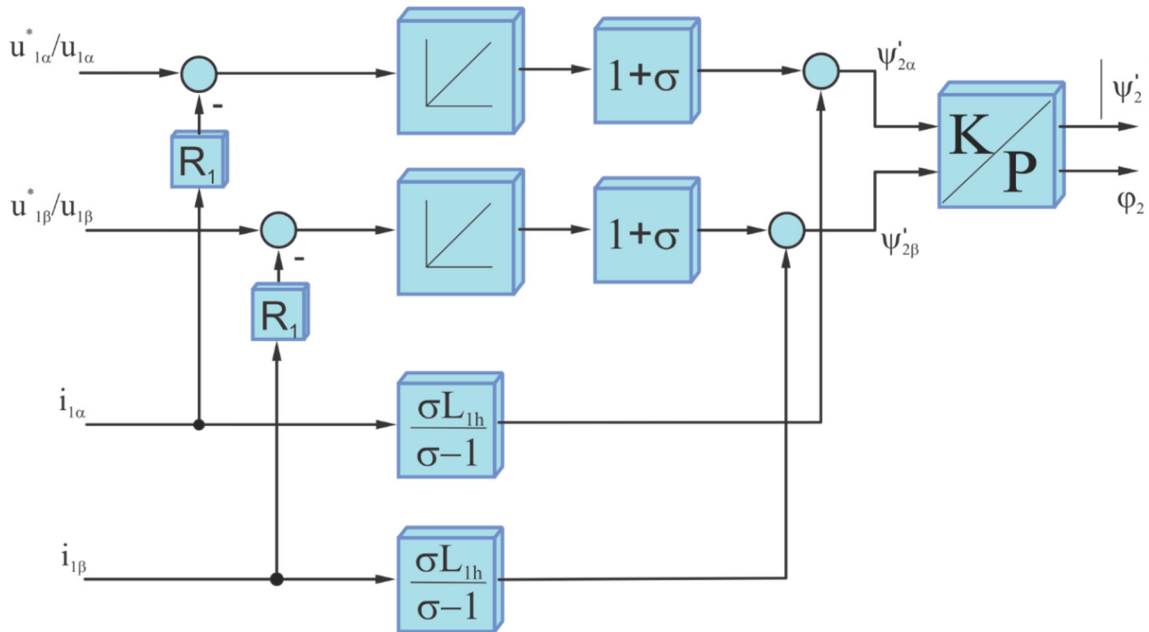


Figure 3-7 Block diagram of the standard and the enhanced voltage model

Because the measurement of the rotor position with the help of an encoder is not required, the voltage model is very suitable estimator for the position of the rotor flux space phasor in the induction machine drives. The stator flux space phasor is estimated by integrating the back electromagnetic force (back EMF), i.e. the integration of the value that obtained after the subtraction of the voltage drop through the stator resistance from the stator voltages. Later on, two open-loop integrators are used for the calculation of the rotor flux space phasor as depicted in Figure 3-7. The main problem in the voltage model is the existence of these two integrators. Due to this, a small DC offset in measured currents and voltages causes drift problem, which must be taken into account. This was the first well-known problem, while the second one is that at zero stator frequency; an ohmic character appears on the machine because of the inductance characteristics are zero. In order to overcome the first obstacle, there are some enhanced voltage models that are presented [47], [48], [119], these models are as an attenuation method, were enhanced methods could be used instead of using a pure integrator in some different form, such as:

- Low gain feedback
- PI element feedback

It should be noticed that the angle error caused by the attenuation can be corrected within certain limits by suitable methods [120]

### 3.2.2.4 Natural Field Orientation

In addition to the benefits of measuring the stator voltages and using them for the computation of the position of the rotor flux space phasor, this work examines the so-called Natural Field Orientation (NFO) under the same assumptions. The NFO control scheme was introduced in 1980 by Ranger Jönsson and patented as ‘‘Method and apparatus for controlling an AC motor’’ in 1994 [51] [52].

For the standard NFO, the reference values of the stator voltages can be used to calculate the angular velocity of the stator flux space phasor, and the integration of the angular velocity delivers the position of the stator flux space phasor.

The NFO can be described by using the complex voltage equations of the induction machine in d,q-coordinates.

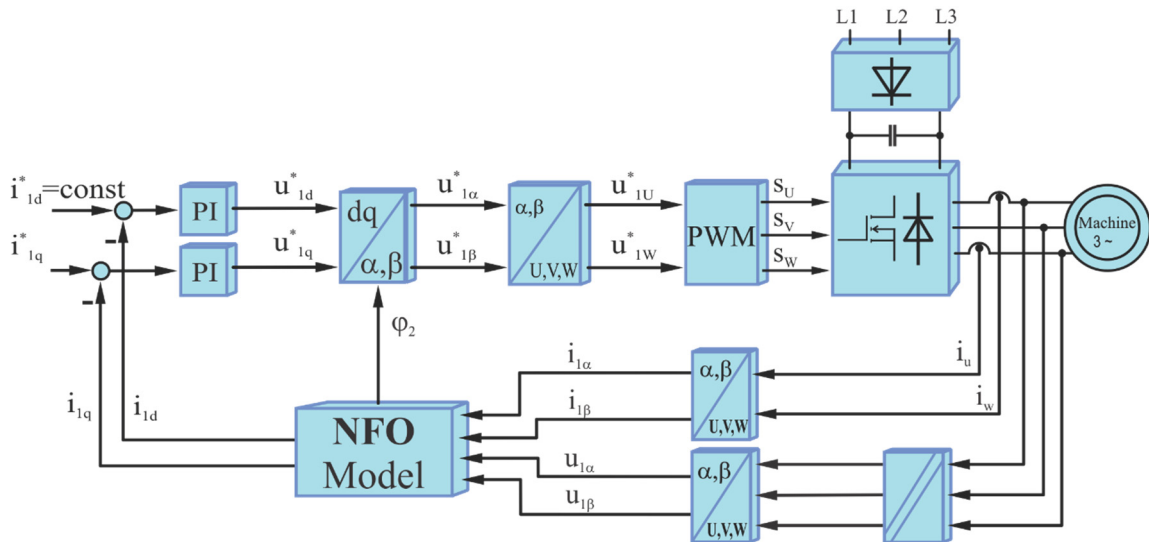


Figure 3-8 Block diagram of the NFO-sensorless control scheme

The NFO basically is based on the idea that the stator flux space phasor is lagging by  $90^\circ$  to the induced stator voltage space phasor as illustrated in Figure 3-9 and supposes that its magnitude is a constant value. From these assumptions, the position of the stator flux space phasor can be computed [58] [59].

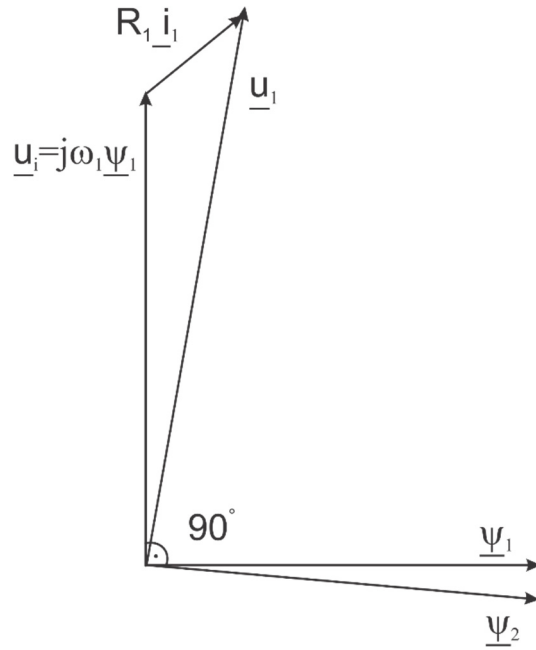


Figure 3-9 Phasor diagram for NFO explanation

In principle, NFO will be explained in stator flux oriented frame because it is easier to understand. In Figure 3-9, the reference frame is aligned to the stator flux space phasor, the corresponding components of the induced voltages are called  $u'_{i1d}$  and  $u'_{i1q}$  Figure 3-10. Assuming that the magnitude of the stator flux space phasor  $\underline{\psi}_1$  is constant and known, its angle can be defined by using the identified induced voltage  $\underline{u}_i$  according to the Figure 3-10.

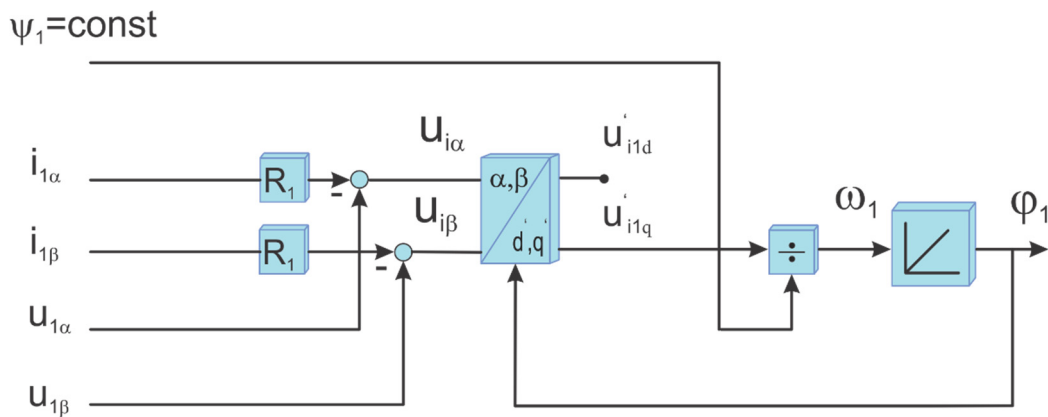


Figure 3-10 NFO scheme in the stator flux reference frame

However, in the stator flux reference frame, the current component  $i_{1q}$  is not proportional to the torque, therefore it is obvious that it is important to work in the rotor flux fixed reference frame.



For NFO calculation in the rotor flux reference frame, the following equations can be applied

$$\underline{u}_1 = R_1 \dot{i}_1 + \sigma \cdot L_1 \cdot \frac{d\dot{i}_1}{dt} + j \cdot \sigma \cdot \dot{\phi}_2 \cdot L_1 \cdot \dot{i}_1 + \frac{1}{(1 + \sigma_2)} \cdot \frac{d\Psi'_2}{dt} + j \cdot \dot{\phi}_2 \cdot \frac{1}{1 + \sigma_2} \cdot \Psi'_2 \quad (3.30)$$

Herein is  $\Psi'_2$ , the magnitude of the rotor flux space phasor,  $L_1$  the stator inductance,  $\sigma_2$  and  $\sigma$  the rotor leakage coefficient respectively the total leakage and  $\phi_2$  the angular position of the rotor flux space phasor related to the  $\alpha$ -axis.

$\Psi'_2$ , the magnitude of the rotor flux can be obtained by using the equation:

$$(\Psi'_2 + \tau'_2 \cdot \frac{d\Psi'_2}{dt}) \cdot \frac{1}{L_h} = i_{1d} \quad (3.31)$$

With  $L_h$  the main inductance of the machine and  $\tau'_2 = L_2 / R_2$  the rotor time constant.

If the terms in (3.30) containing  $\Psi'_2$  are considered to correspond to the induced  $\underline{u}_i$  voltage, it can be written:

$$\underline{u}_i = \underline{u}_1 - R_1 \dot{i}_1 - \sigma \cdot L_1 \cdot \frac{d\dot{i}_1}{dt} - j \cdot \sigma \cdot \dot{\phi}_2 \cdot L_1 \cdot \dot{i}_1 \quad (3.32)$$

The rotor voltage equation in d, q-coordinates can be written as:

$$\frac{d\Psi'_2}{dt} = -j \cdot (\dot{\phi}_2 - \dot{\gamma}) \cdot \Psi'_2 - \frac{R_2}{1 + \sigma_2} \cdot \left( \frac{\Psi'_2}{L_{1h}} - \dot{i}_1 \right) \quad (3.33)$$

it contains the mechanical angular velocity  $\dot{\gamma}$  and can be used for completing the NFO scheme.

By combining (3.32) with (3.33) and splitting in real and imaginary part follows:

$$u_{iq} = \dot{\phi}_2 \cdot \frac{1}{1 + \sigma_2} \cdot \Psi'_2 \quad (3.34)$$

Hence the position of the rotor flux space phasor can be computed as:

$$\varphi_2 = \int (1 + \sigma_2) \frac{u_{iq}}{\psi'_2} dt \quad (3.35)$$

and the mechanical angular velocity results to be:

$$\dot{\gamma} = \frac{u_{iq}(1 + \sigma_2) - \frac{R_2}{(1 + \sigma_2)} \cdot i_{1q}}{\psi'_2} \approx \frac{u_{iq} - R_2 \cdot i_{1q}}{\psi'_2} \quad (3.36)$$

The NFO scheme also uses the stator voltages for the calculation of the induced voltages and thus for obtaining the rotor flux space phasor. Again this work examines the possible enhancement of the scheme if the measured terminal voltages are used instead of the reconstructed ones

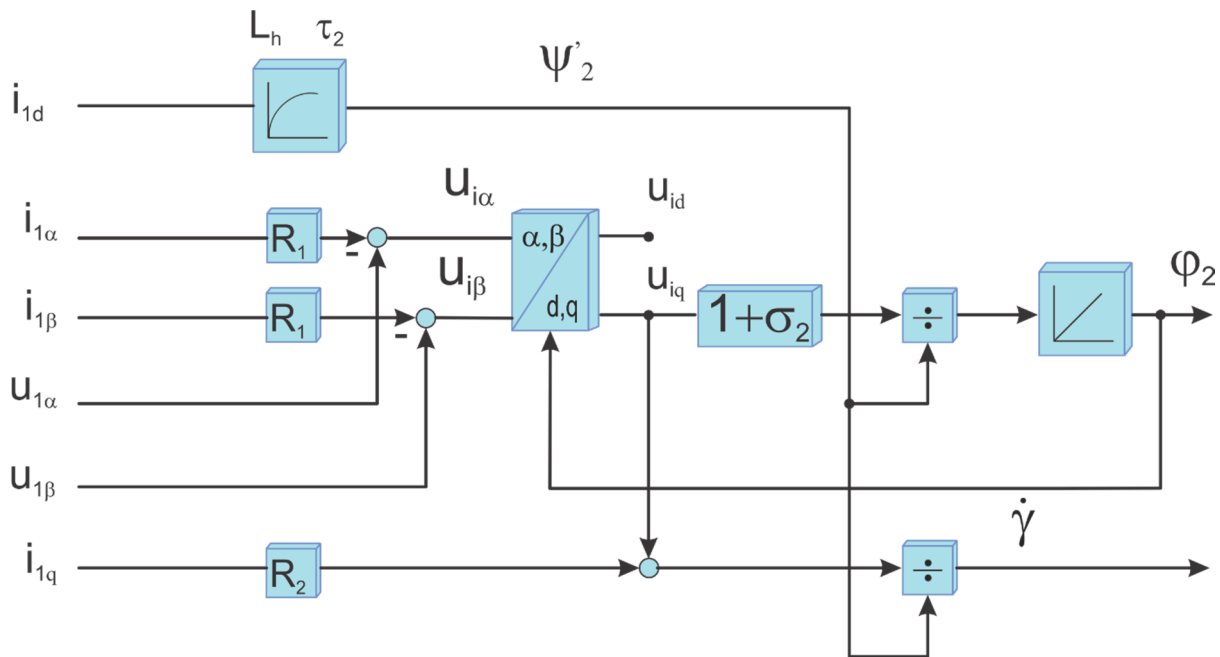


Figure 3-11 NFO scheme by assuming that  $\sigma$  and  $\sigma_2$  can be neglected

### 3.2.2.4.1 Advantages of the natural field orientation control method

By using the encoder-less natural field orientation theory, some advantages may be obtained:

- Natural field orientation is an alternative efficient control technique for the induction machine with the simplicity of implementation and control, even in an aggressive environment.

- Only one parameter of the motor needs to be known which the stator resistance is.
- Stable performance in the experimental results; which represents in both motoring and generating, as well as at zero frequency [55].
- The omission of the flux integrator, i.e. elimination of the two open-loop integrators, which causes the drift problem [121].

### 3.3 Model Reference Adaptive System (MRAS)

#### 3.3.1 Adaptive Method (AM)

Adaptive methods are based on the error comparison between data obtained by means of measurements in the considered system and the model data. This error is used for the correction of the model i.e. the model is adapted to the real system, it is adaptive. In another words, the procedure contains a comparison between the reference model and the adaptive model and this technique is called model reference adaptive system (MRAS approach) and its principal structure is depicted in Figure 3-12. [11] [122] [123].

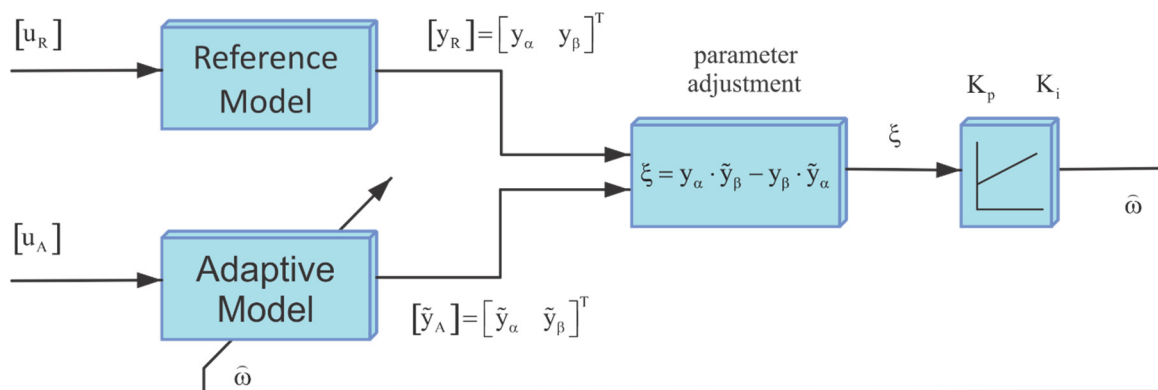


Figure 3-12 Basic structure of an adaptive control

#### 3.3.2 Model reference adaptive system method

Model reference adaptive system method uses actually two models. The first one is the reference model, which is derived from equations that do not contain the variable that has to be estimated value that looking for. In the present case the angular position of the rotor flux space phasor or the corresponding time derivative. The second model is the adaptive one, which follows the reference model and it does contains the variable to be identified. As shown in Figure 3-12 error between the output of the reference model and the output of the adaptive model is used as input to the adaptation algorithm that performs the speed estimation [11].

With the reference model is fed with  $[u_R]$  and its output is described by a vector  $[y_R] = [y_\alpha \ y_\beta]^T$ , conversely the adaptive model is fed by  $[u_A]$  and the output is  $[\tilde{y}_A] = [\tilde{y}_\alpha \ \tilde{y}_\beta]^T$ . The error can be calculated as:

$$\xi = y_\alpha \cdot \tilde{y}_\beta - y_\beta \cdot \tilde{y}_\alpha \quad (3.37)$$

where:

$y_\alpha$  and  $y_\beta$  are the outputs of the reference model;

$\tilde{y}_\alpha$  and  $\tilde{y}_\beta$  are the outputs of the adaptive model.

$\xi$  can be considered to be proportional to the angular deviation between  $[\tilde{y}_A]$  and  $[y_R]$  thus, it can therefore be used for the adaptation of the model. In the present case for the adaptation law, a linear PI controller is used to correct the error between the reference model and the adaptive model to zero. If, for instance, the speed is the variable to be compensated in the adaptive model, the following equation can be used [63]:

$$\hat{\omega} = \xi \left( K_p + \frac{K_i}{s} \right) \quad (3.38)$$

where:  $\hat{\omega}$  is the estimated speed,  $K_p$  and  $K_i$  are the proportional and integral parameters of the PI controller and  $s$  is the Laplace variable.

By substituting (3.38) in (3.37), the speed estimation is

$$\tilde{\omega}(t) = K_p (\tilde{y}_\alpha \cdot y_\beta - y_\alpha \cdot \tilde{y}_\beta) + K_i \int_0^t (\tilde{y}_\alpha \cdot y_\beta - y_\alpha \cdot \tilde{y}_\beta) d\tau \quad (3.39)$$

The estimated speed is changed until the error  $\xi$  between the reference and the adaptive models becomes zero, or  $\tilde{y}_\alpha \cdot y_\beta = y_\alpha \cdot \tilde{y}_\beta$  and thus the estimated speed is the actual speed of the rotor. The speed determination and the stability of the system, which the algorithm of the adaptation determines, depending on the choice of the PI controller parameters that are used in the adaptation algorithm.

### 3.3.2.1 MRAS when using voltage and current model

The principle of MRAS can be applied to the induction machine with the voltage model as reference and the current model as adaptive system. Such a structure is shown in Figure 3-13.

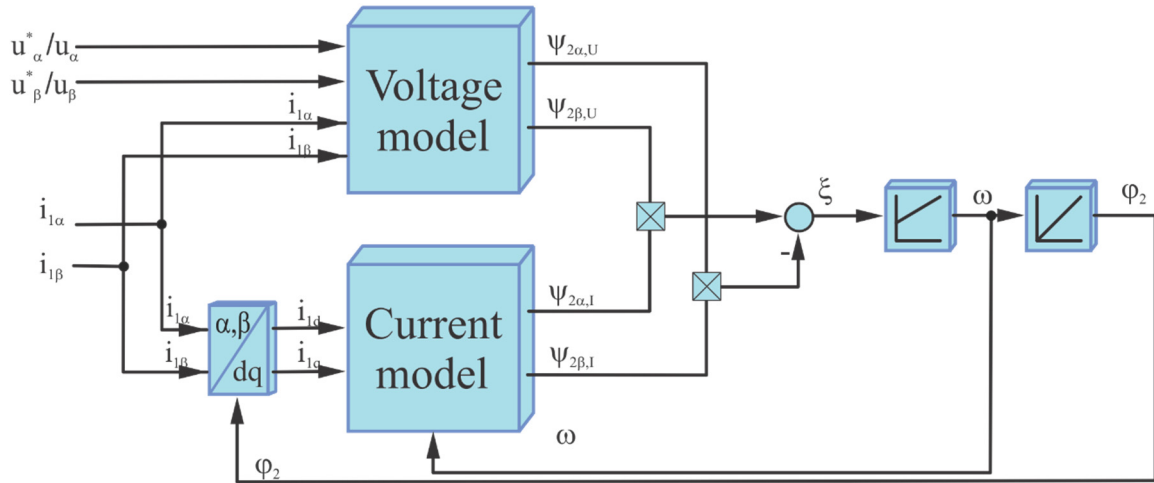


Figure 3-13 Block diagram of the MRAS when using voltage model

In this MRAS the output of the voltage model is  $[y_R] = [\psi'_{2\alpha,U} \quad \psi'_{2\beta,U}]^T$  being  $[\tilde{y}_A] = [\psi'_{2\alpha,I} \quad \psi'_{2\beta,I}]^T$  the output of the adaptive model. In the same manner an error  $\xi = \psi'_\alpha \cdot \psi_\beta - \psi'_\beta \cdot \psi_\alpha$  proportional to the angular displacement between the flux space phasors of each model. As is clearly shown in Figure 3-13 the voltage model as it was described in the previous section is fed with the actual or the calculated values of the stator voltages and with the values of the measured currents and delivers the rotor flux space phasor. The current model, as also described in previous sections, is adaptive, is fed with the measured currents and its equations contain the speed  $\omega$  as state variable. Therefore, the speed  $\omega$  can be used for the adaptation. It also delivers the rotor flux space phasor.

As depicted in the in Figure 3-13, a PLL is used in order to change the value of  $\omega$  in the adaptive current control until the error  $\xi$  is minimized.

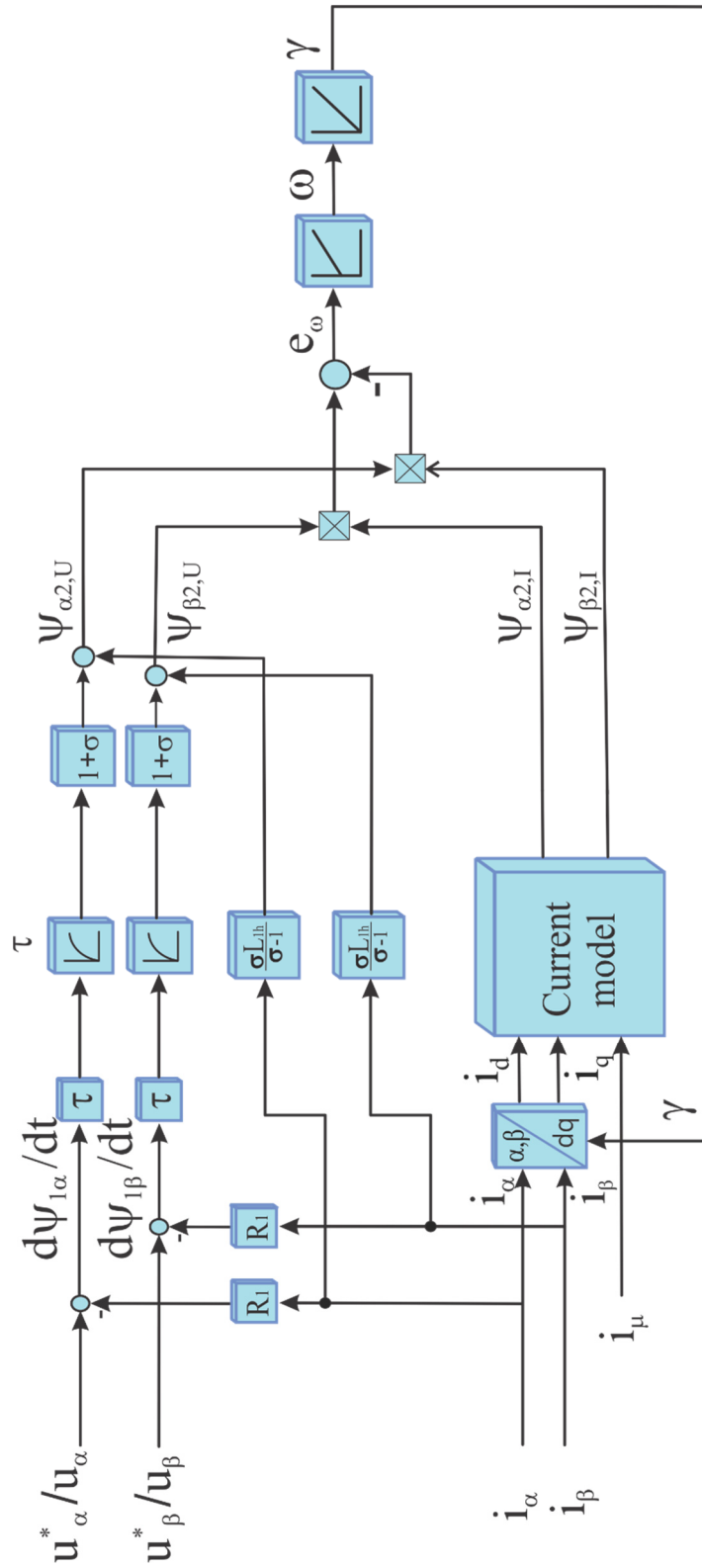


Figure 3-14 Model reference adaptive system with correction of the voltage model

### 3.3.2.2 MRAS with the NFO model as reference

Instead of the standard or enhanced voltage model, the model of the natural field orientation (NFO) can also be used in MRAS. Figure 3-15 shows the block diagram for the MRAS when using the natural field orientation model as a reference model.

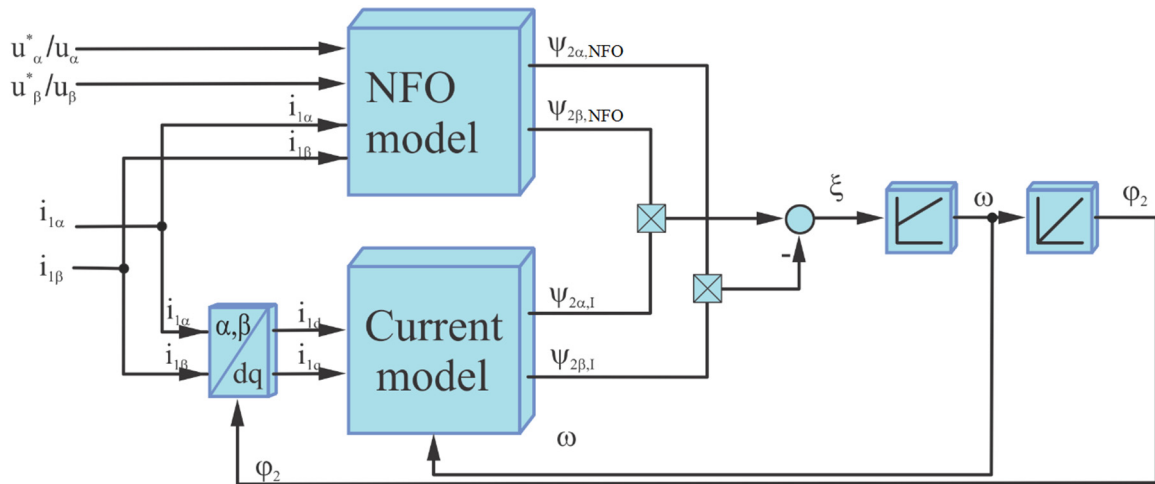


Figure 3-15 Block diagram of the MRAS when using NFO model

## 3.4 Summary of the chapter

This chapter presents a principle of the control of the induction machine. The sensorless control of the induction machine is also discussed and some control methods based on the fundamental wave models are presented. Thus, three different approaches for the calculation of the magnitude and the position of the rotor space phasor are introduced. A widely used, simple approach, which employs the rotor position in addition to the measured stator currents is the first model, which is called current model. In a second model represented by a simple approach without an additional speed sensor, the rotor flux and position can be calculated by using the terminal stator voltages and currents. The voltage model of the induction machine is an appropriate flux estimator model, due to its simplicity; here the stator resistance is only the important parameter of this model that has to be corrected. As also explained in this chapter an enhancement of the voltage can be achieved when it is fed by the voltage applied to the machine measured after the LC filter instead of the voltage reconstructed from the switching signals of the inverter.

The third model presented is the natural field orientation that is discussed as an efficient control technique for the induction machine. An enhanced natural field orientation that is fed with the measured terminal voltages of the machine is introduced as well.

The last section of the chapter deals with the principle of a model reference adaptive system together with the correction of the voltage model that is used in this work. Finally, the combination of the enhanced and the standard NFO is also presented in this chapter.



## **4 Enhancement of the Conventional Control Techniques**

### **4.1 Sinusoidal voltages and practicability of the measurement**

As explained in previous sections, the voltage source inverter produces a switched voltage that consist of a sequence of rectangular pulses that differ in the width (pulse width modulation). The output voltage exhibits a spectral composition that contains the fundamental sinusoidal wave with the desired amplitude, frequency and phase as well additional harmonics with frequencies and amplitudes that depend on the utilized modulation scheme, on the switching frequency and on the operation point of the inverter. In case of a sine-triangle or a space phasor modulation, the dominant harmonics are in the range of the switching frequency and it is multiple.

The shape of the pulses of the motor terminal voltage is not really rectangular but distorted. Its amplitude can be increased due to an effect caused by the high  $du/dt$  ratio when a transistor is turned on in the inverter. The physical explanation for the voltage increase is a wave reflection caused by the mismatching that appears between the impedance of the cable characteristic and the motor, which leads to a ringing voltage overshoot at the motor terminals. This increase of the voltage is dependent upon the  $du/dt$  at the inverter output, on the motor cable type, cross-section, length, shielded or unshielded, inductance and capacitance, and depends on the high frequency surge impedance of the motor as well.

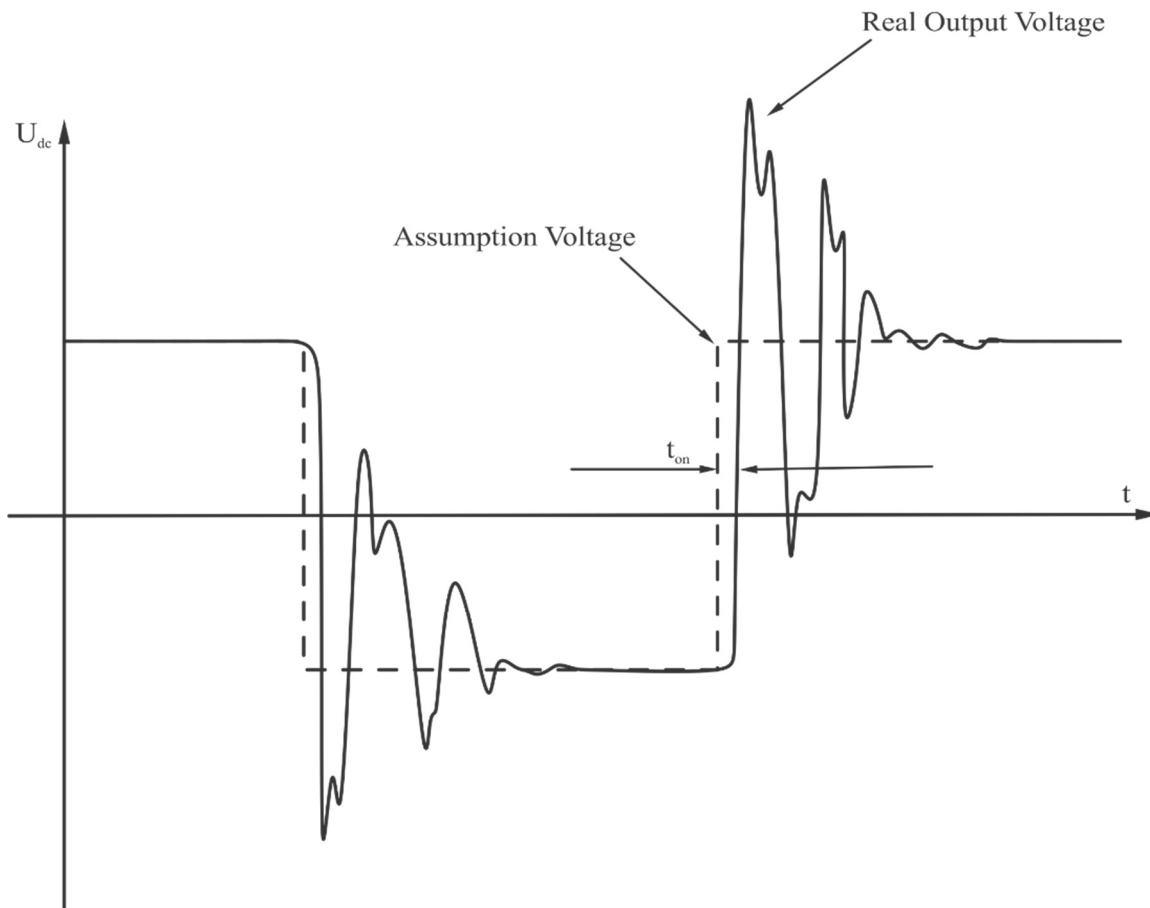


Figure 4-1 Sketch of the principal traces of the ideal (dotted line) and the real voltage (continuous line) on the terminals of the machine

In Figure 4-1 the voltage on the terminals of the machine is sketched together with its ideal wave form. As explained above, the overshoot depends on many parameters of the installation and on the wave impedance of the motor, but also on the steepness of the inverter voltage and in case of a full reflection leads to a voltage on the machine terminals with the double height of the inverter output.

A sine-wave filter can be used in order to reduce the harmonics contained in the inverter voltage applied to the machine that are produced by the pulse width modulation (PWM). As stated above, the harmonics in the inverter voltage are in the range of the switching frequency and its multiples. By adding a sine-wave filter between the inverter and the machine, the harmonics of the pulse shaped voltage of the inverter and the overshoot due to the wave reflection are reduced and the line-to-line voltage at the terminal of the machine becomes almost sinusoidal [97].

The effect of the filter can be seen in **Fehler! Verweisquelle konnte nicht gefunden werden.** and **Fehler! Verweisquelle konnte nicht gefunden werden.** that shows the

filter inductor voltage and the terminal stator voltage respectively. Regarding the influence of the inverter, the same behavior can be seen in the common mode voltage.

The sine-wave filter is designed to allow the low frequencies to pass, while the amplitude of the high frequency harmonics are reduced. As a result, not only the ripple of the voltage but also the ripple of the currents in the machine is significantly lower than in operation without filter.

Additional benefits of the filter are the damping of the acoustic noise, the reduction of the insulation stress and bearing currents in the machine leading to a prolonged machine lifetime.

Regarding the increase of voltage due to the reflections on the terminals of the machine, the length of the cable between machine and inverter plays an important role because it determines the wave impedance. Thus, the voltage peaks become higher if the machine is installed far from the drive and connected with long cables, in such cases, the sine-wave filters open up the possibility of using a long machine cable.

One of the objectives of the present work is the design and implementation of a three-phase, two-level voltage source inverter (VSI) equipped with silicon carbide (SiC)-switches and an output filter featuring sinusoidal output voltages and currents. The availability of SiC-switches in different ratings of voltage and current allows the realization of conventional inverters to be able to operate at higher switching frequencies up to 100 kHz or more. For the feeding of three-phase machines, these high switching frequencies are not really necessary in usual industrial applications. Nevertheless, the high switching frequency of the inverter can prove advantageous if the output voltages are appropriately filtered and become rather sinusoidal. In this way, some negative effects of the non-sinusoidal voltage can be attenuated, but it is expected that the performance of the sensorless control can also become better [1].

The high switching frequency that can be achieved with the SiC-switches gives the opportunity to design a small, low-cost LC filter for the output of the inverter. In this way, the harmonic content of the machine voltages is minimized and the measuring of the inverter output voltage becomes feasible, and in addition the measured voltages can be used instead of the reconstructed ones for the enhancement and a better performance of the voltage model as well of the natural field orientation as well as of the control scheme [1].

## 4.2 Enhancement of the standard voltage model

As illustrated in previous sections, the voltage model is a simple approach that can be used to calculate the rotor flux space phasor and its angular position without the need of an additional mechanical encoder since this model may only use the electrical measurable quantities i.e. the stator currents and terminal voltages of the machine.

In the case of the standard voltage model, it is assumed that the voltage set-points  $u_d$  and  $u_q$  respectively  $u_\alpha$  and  $u_\beta$  (i.e. the outputs of the current controller) correspond to the actual voltages on the machine terminals. This is a very common approach that is implemented in many commercially available inverters. Since there are discrepancies between the calculated signals and the actual voltages due to non-linearities of the inverter, the model has some drawbacks that can be, at least partially, compensated for: like dead time effect and drain source voltage  $u_{DS}$  drop. In the following some of these effects and non-linearities are discussed.

### 4.2.1 Dead time

One of the drawbacks that are accompanied when using the standard voltage model is the delay caused by the dead time. As it is well known, the stator voltages are not measured directly, but it is determined from the measured intermediate circuit voltage and the current switching state of the inverter. In particular, the inverter dead time must be taken into account, i.e. the transitional period from one switching state of one phase to the next. Figure 4-2 shows the gate signal in a case that does not include dead time and in a case of including dead time

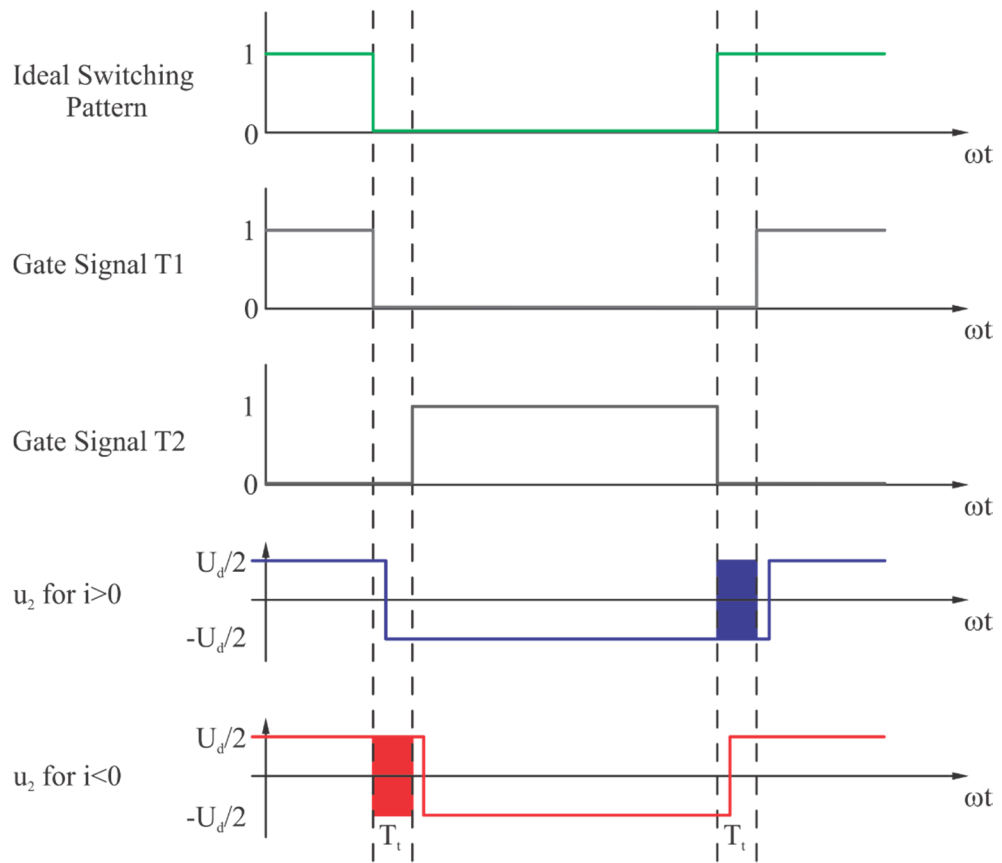
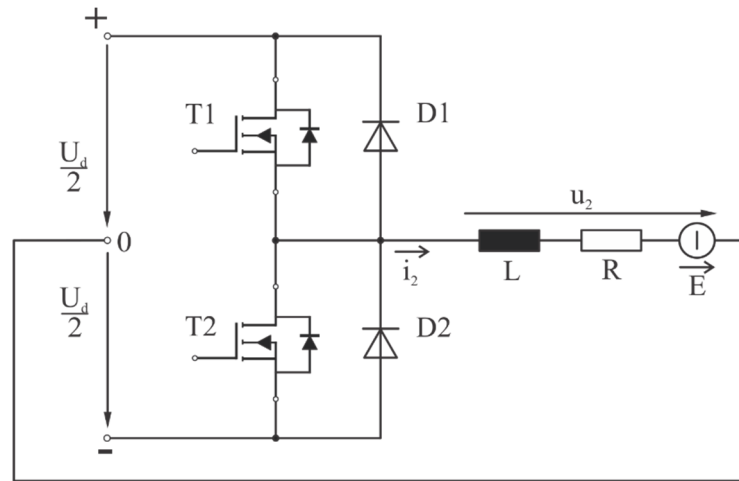


Figure 4-2 Gate signals with and without dead time

### 4.2.2 Transistor nonlinearity

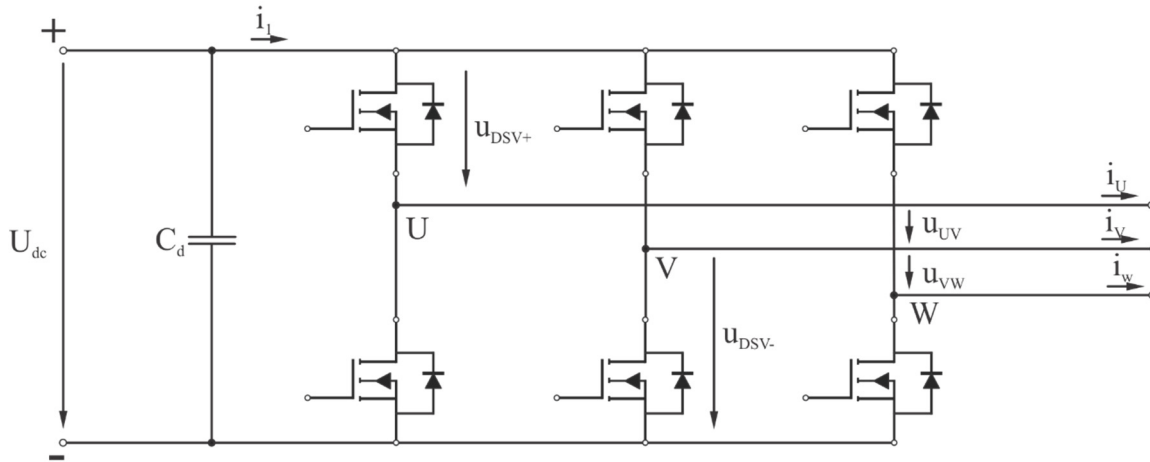


Figure 4-3 Output line to line voltage in conventional two-level inverter

The second common source for a discrepancy between the actual voltages and the calculated ones is the voltage drop drain-source  $u_{DS}$ . For any inverter and depending on the current; different values of  $u_{DS}$  may be calculated in order to compensate for current and temperature. The output line to line voltage in Figure 4-3 can be calculated according to:

$$u_{UV} = u_{dc} - u_{DSU+} - u_{DSV-} \quad (4.1)$$

where  $u_{DS}$  is a function of drain current ( $i_D$ ) and of the junction temperature ( $T_j$ ).

### 4.2.3 Delay in the signal processing

In all electronic circuits, there is a delay between the transmission and reception of analogue or digital signals caused by the non-ideal behavior of the electronic components. In a power electronic inverter, there is a delay between the calculated switching commands in the control and the real firing pulses in the gates of the switches. In the case of using fiber optic cables to send the gate signals, there is a delay in the optical cable and the optical receiver, besides a difference in the delay of the cables and the receiver in the different phases is also noticed. As each path has a different delay, the resulting firing signals can have a pattern as sketched in Figure 4-4.

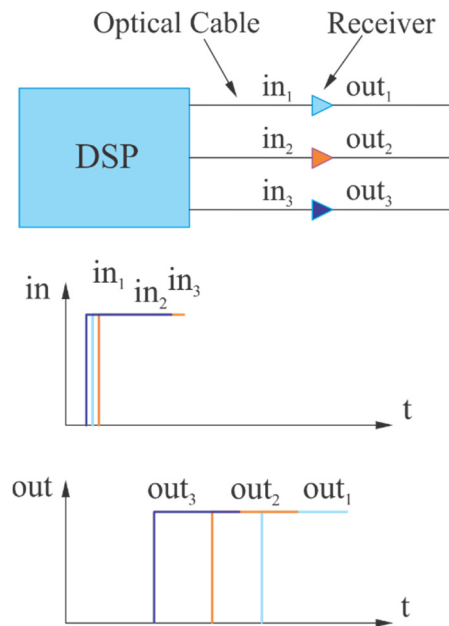


Figure 4-4 Delay of signal processing

Figure 4-5 shows the ideal output voltage  $u_{ideal}$ , and the associated switching signals of the upper and lower MOSFETs as well as the resulting real voltage  $u_{U0}$ . Figure 4-5 shows the most common delays in the inverter which are the drawbacks that are accompanied when using the standard voltage model that is fed by reference values of the voltages and has to be compensated in the voltage model.

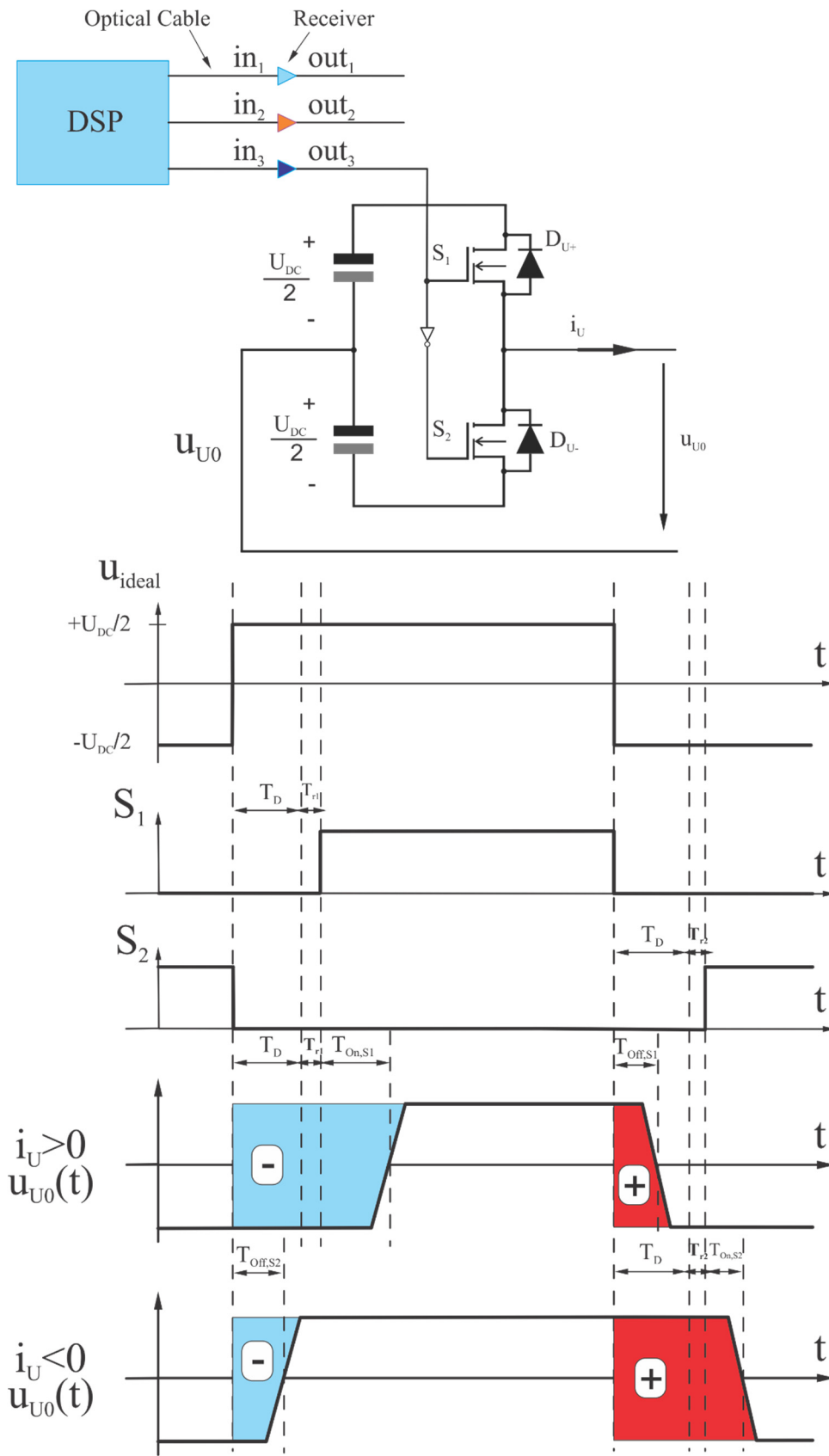


Figure 4-5 Distortion of the output voltage due to dead time, signal processing and switching delays, depending on the current direction



Where:

$u_{0,ideal}$  is the ideal output voltage

$T_D$  is the dead time.

$T_{on,S1}$  is the Switch-on delay of the upper MOSFET

$T_{off,S1}$  is the Switch-off delay of the upper MOSFET

$T_{on,S2}$  is the Switch-on delay of the lower MOSFET

$T_{off,S2}$  is the Switch-off delay of the lower MOSFET

$T_{r1}$  is the delay of the upper signal processing (optical receiver of the upper gate)

$T_{r2}$  is the delay of the lower signal processing (optical receiver of the lower gate)

In Figure 4-5, it is clearly shown that the output voltage is lower than the ideal voltage for  $i_u > 0$ , which is represented in blue, while the red shows that the output voltage is larger than the ideal voltage for  $i_u < 0$ . On the basis of the dead time, the switching delay time and the signal processing delay time is presented, however there is another effective turn-on and turn-off times for the three half-bridges.

Some of these effects can be compensated for, either by characterizing the inverter or by modelling the delays within the control. For instance, if the dead time of the inverter is known, the non-linear effect could be compensated for depending on the current direction. There are many proposals in the literature for alleviating this problem, some with satisfactory results and all with different efforts of implementation. Despite all of the sophisticated compensation techniques, it is evident that all these effects do not appear when the voltages are measured directly on the terminals of the machine and, therefore this is the approach chosen in this work.

### 4.3 Practical realization of the integrator

A core component in the implementation is the integrator, which is used for the calculation of the stator flux space phasor out of the stator voltages and currents. It is well known that the realization of this integration with electronic means (analogue or digital)

is difficult especially in the range of low frequencies. Independently of the use of measured voltages or of reconstructed ones, in the modelling of the voltage equation of the stator the integrator presents a drift that prevents the proper operation of the model; correspondingly some technics have been developed that limit or eliminate the drift of the integrator are further discussed in the following.

#### 4.3.1 Low gain feedback

In the practical implementation, the easiest way to prevent the drift caused by the integrator is to add a negative feedback. In this way the behavior of the open integration at low frequencies is acceptable. The resulting structure, which includes the integrator and the negative feedback element, behaves like a low-pass-filter (LPF) with a cut off frequency that determined by negative feedback element ( $k$ ). The new structure can be seen in Figure 4-6:

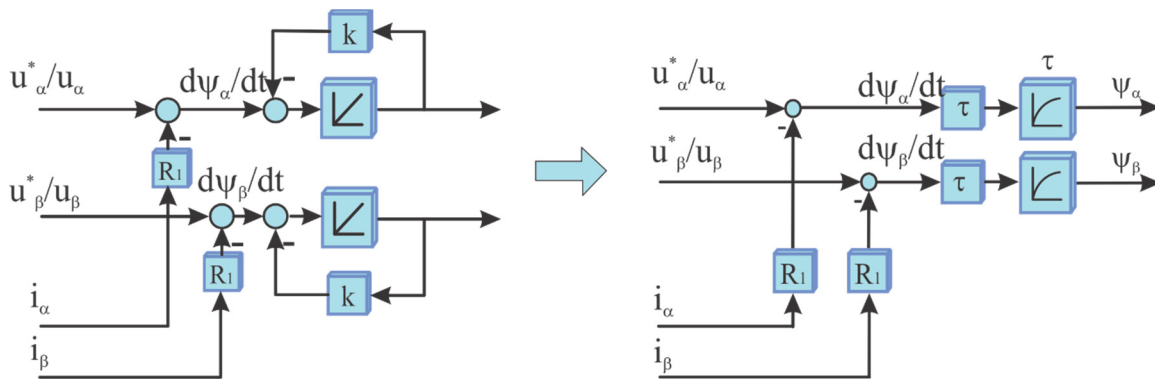


Figure 4-6 Equivalent block diagram with a LPF attenuation

As depicted in the same figure, the integrator in the left side can be approximated by a low-pass-filter with a transfer function  $G(s) = \tau / (1 + \tau s)$  as depicted in the right hand side [124]. Experiments have shown that  $\omega_c = 1/\tau$ ; the corner frequency of the low-pass-filter can be set to a lower value by using the enhanced voltage model. In this way the integration yields better results and stabilize the operation in the low frequency range.

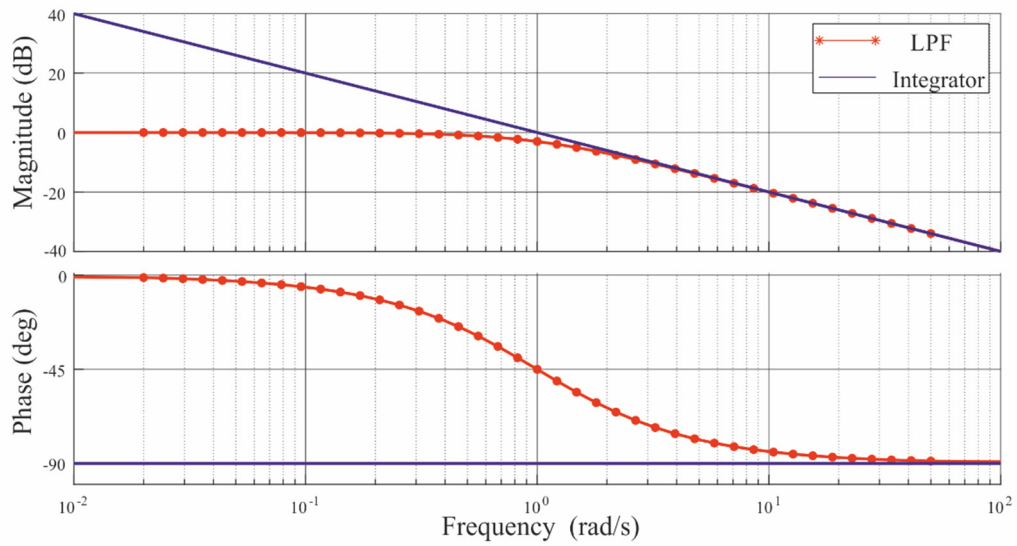


Figure 4-7 Bode diagram comparison between the pure integrator and the low-pass-filter with a cut-off frequency of 1 rad/s

The behavior of the approximated integration can be examined by using the Bode diagram presented in Figure 4-7 and compare the low pass filter (enhanced integrator in red) with a pure integrator (in blue). It can be seen that both have identical behavior at high frequencies. However, at low frequencies, i.e. below the cut-off frequency of the low pass, the gain of the modified integrator remains contrary to the pure integration. As a result, there is no drift. It can also be observed that above a certain frequency both have the same behavior.

### 4.3.2 Feedback with a PI element

An alternative way of damping can be achieved if a feedback with the proportional-integral element (PI) is used.

The influence of the DC offset is eliminated completely. The resulting Bode diagram is depicted in Figure 4-8 [67] [68]. In comparison to low gain feedback, the corner frequency may be reduced.

The green curve belongs to the modified integrator with values ( $T_N=0.1$ ,  $K_V=0.1$ ), while the red one corresponds to ( $T_N=1$ ,  $K_V=1$ ). For the sake of comparison, the blue line represents the pure integration. The determination of the parameters  $T_N$  and  $k_V$  has to be carried out wisely and must take the time constant of the system into account [124].

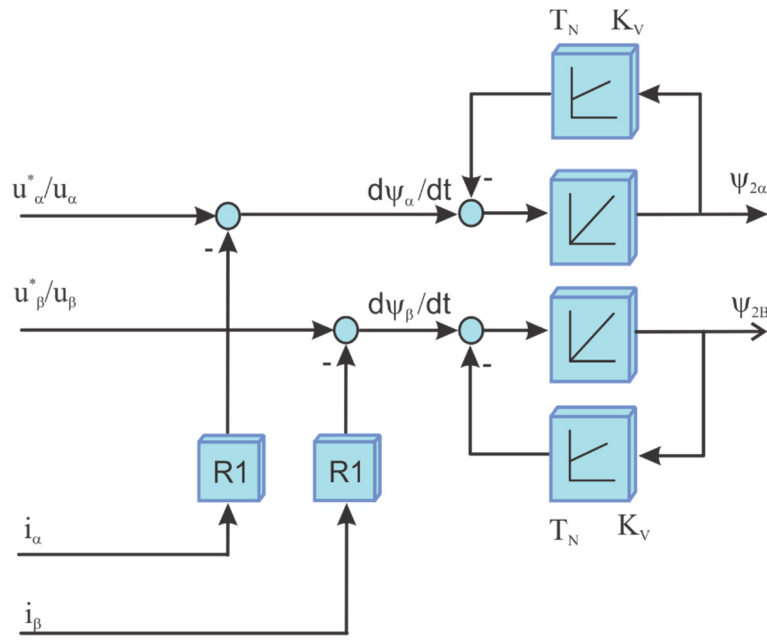


Figure 4-8 Block diagram of the integrator with a PI feedback

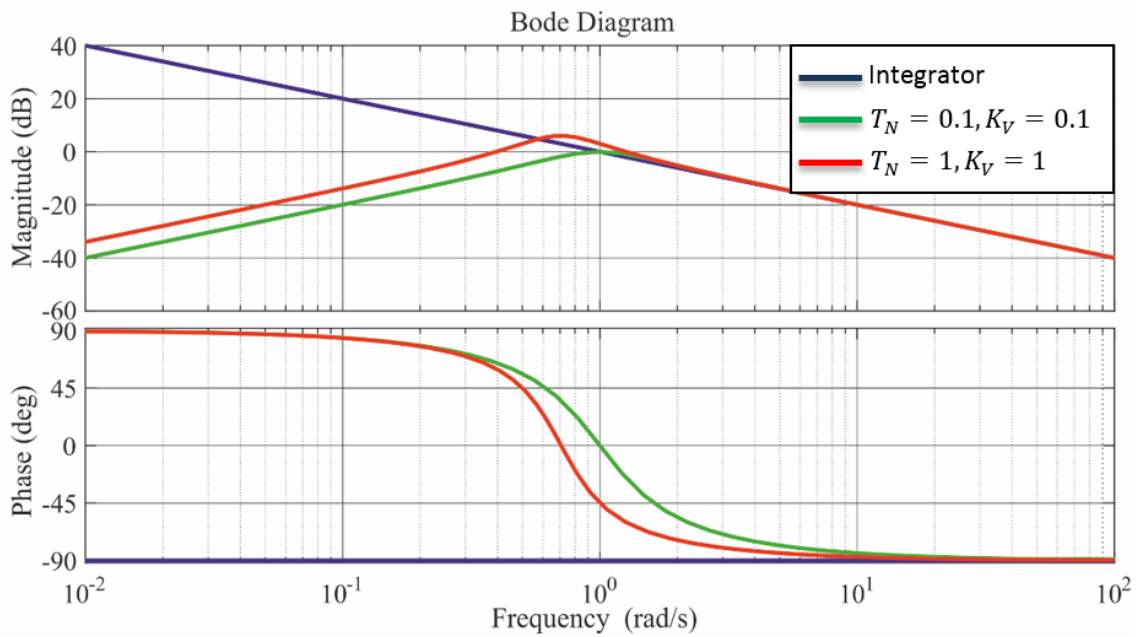


Figure 4-9 Bode diagram comparison between the pure integrator and PI feedback

#### 4.4 Measurement of the terminal voltages in the low speed range

In general, the stator voltage can be expressed as  $\underline{u}_1 = R_1 \cdot \underline{i}_1 + \frac{d\underline{\psi}_1}{dt}$ . At high speed is

$|R_1 \cdot \underline{i}_1| \ll \left| \frac{d\underline{\psi}_1}{dt} \right|$  and therefore  $\underline{u}_1 \approx \frac{d\underline{\psi}_1}{dt}$ . Thus in the high speed range, the induced volt-

age in the induction machine is high enough and the voltage model has no problem with the all the effects of non linearities, offset, or drift, as well as parameter uncertainties. In this range, the error produced by the non-ideal behavior of the inverter is small if compared with the value of the induced voltage; therefore the reconstruction of the voltage based on the reference values of the voltage is very good as can be seen in Figure 4-10.

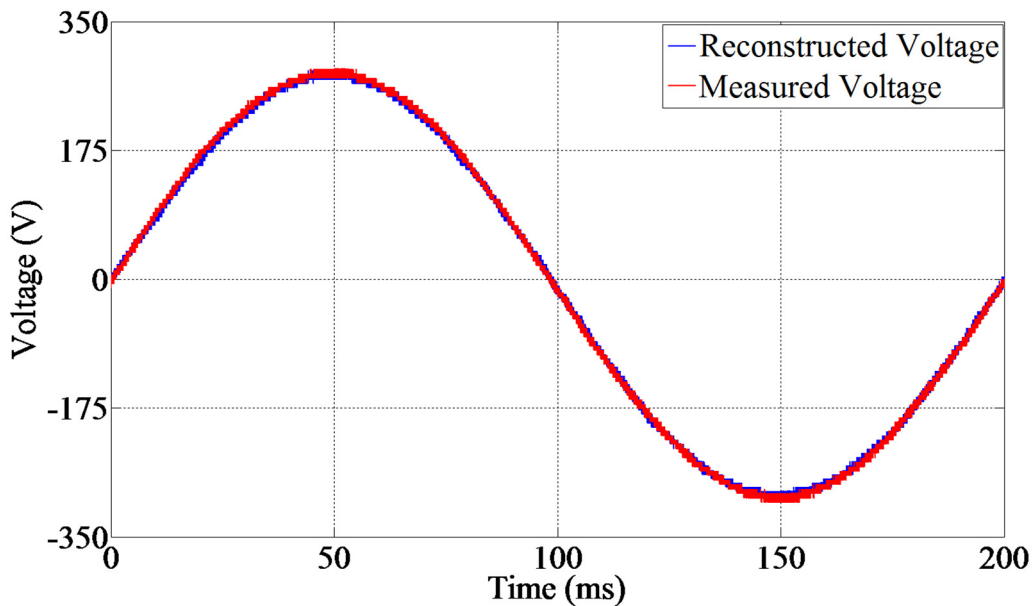


Figure 4-10 Comparison between measured and reconstructed voltages at high speed

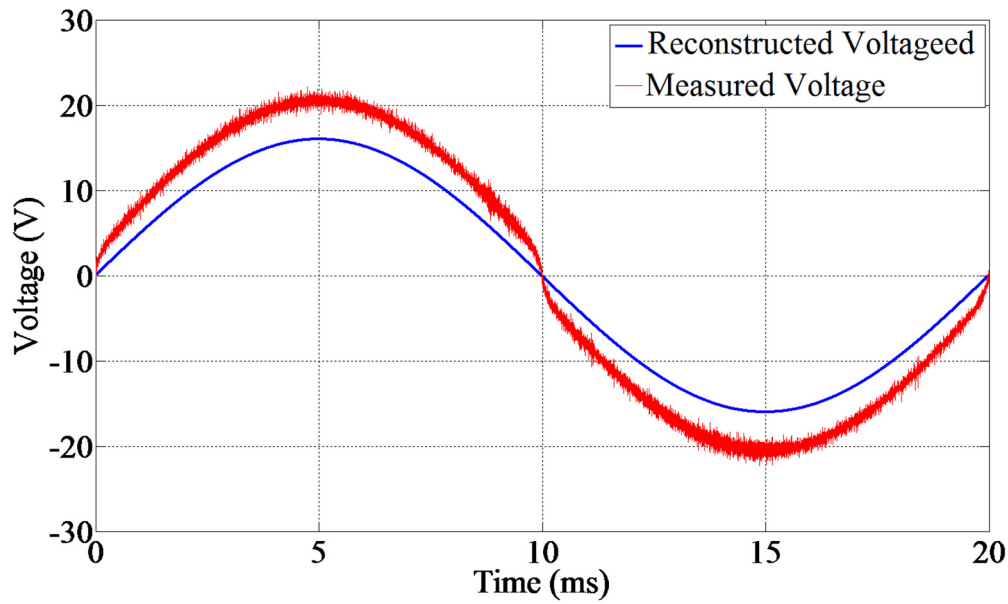


Figure 4-11 Comparison between measured and reconstructed voltages at low speed

On the other hand, if the model is working in the low speed range the reconstruction of the voltage is more critical, and not as precise, because the error, due to all the before mentioned physical effects, is in the same order of magnitude of the induced voltage and the task of reconstruction and compensation for the non-ideal behavior of the inverter based on the calculated voltages becomes very challenging. Figure 4-11 shows how the non-linearities affect the reconstructed voltages if the compensation does not work properly.

A SiC inverter with an output sinusoidal filter for feeding an induction machine produces almost sinusoidal voltages on the terminals of the machine. Thus, the voltage on the terminals of the machine can be measured with a galvanic separation and the measured values can be used in the voltage model that is here called the "enhanced" model. In this way a significant improvement in the estimation of the rotor flux space phasor can be expected, which will be confirmed by experiments as articulated in the next chapter.

One further approach that unfortunately could not be realized in the frame of this work, but that can improve the overall behavior of the whole scheme, is to use the reconstructed voltages in the high speed range and to design a special measurement electronic board to be activated in the low speed range. Today, precision isolation amplifiers are available which can ease this task and fulfil the demands of the mandatory galvanic

separation. Since the voltage measurement is only necessary in the low speed-low voltage range, the amplifier can be disconnected outside of the interesting range, offering in this way an optimum resolution and quality of the measurement.

#### **4.5 Mandatory experimental validation**

It is worth it to mention that the research topics addressed in this work deal with the practical problems related to suitability of models used in the sensorless control of the induction machine. A theoretical analysis of the phenomena and a standard simulation are not sufficient and therefore it is necessary to validate all theoretical considerations by means of experimentation. Thus, in the frame of this work, the digital simulation was used only for the design of the sinusoidal filter and for the general considerations, but not for the assessment of the different proposals.

#### **4.6 Summary of the chapter**

This chapter aims to describe the enhancement of the conventional control techniques. The advantages of adding a sine-wave filter connected between inverter and machine in order to reduce the harmonics in the output voltage and for obtaining an almost sinusoidal line-to-line voltage at the terminal of the machine is presented. In addition to the benefits of using a sine-wave filter, some other methods for the consideration and partial compensation of non-linearities and imperfections of the inverter in the control models are discussed. Some technics that have been developed in order to limit or eliminate the drift of the integrator are also briefly explained. A section is dedicated to explain the measurement of the terminal voltages in the low speed range and offers a proposal for the increase of the resolution and quality of the measurement.

## 5 Experimental Validation

In the following, the experimental results of the research work are discussed based on previously discussed theoretical concepts.

This chapter is divided into three sections: the first section is dedicated to a detailed description of the laboratory setup that consisted of a three-phase, two-level conventional voltage source inverter (VSI), equipped with silicon carbide (SiC)-switches and an output LC filter featuring sinusoidal output voltages. The second section shows the experimental results of the control schemes proposed in this work: the enhanced field oriented and sensorless control scheme using both voltage model and natural field orientation (NFO) schemes and the voltages measured on the terminals of the machine. Finally, the third section deals with the experimental results of the model reference adaptive system (MRAS) also proposed in this work and that used the enhanced voltage model (EUM), the natural field orientation (NFO) and enhanced natural field orientation (ENFO).

### 5.1 Experimental setup

Figure 5-1 shows an overview of the whole system, which consists of the control and power electronic parts, the mechanical structure with the examined induction machine, with a braking machine as a load and the different control and measurement interfaces.





### 5.1.1 Implementation of the controller and sensors

The induction machine is controlled by using a stand-alone single digital signal processor (DSP) controller board (TMS320F28335 eZdsp) which is particularly suitable for control tasks and exhibits the following main features:

- Processor capability of 32-bit floating-point microcontroller
- Operating speed of 150 MHz
- 68 K bytes RAM
- A flash memory of 512 K bytes
- SRAM memory with 256 K bytes
- Sixteen channels of 12-bit A/D converters with an input range from 0 to 3 volts.
- 18 PWM channels
- Analog, I/O, multiple connectors
- Operation with 5-volt
- Interrupt controller
- D/A converter (8 channels with 12 bits in addition to 4 PWM D / A channels)

The digital signal processor (DSP) was programmed using C-language and compiled to machine language by using the software of “code composer studio v3.3”.

The dedicated electronic signal conditioning circuits, (for example: A/D and D/A converter buffer circuits, encoder interface, optical transmitter circuit, protection circuits, etc.) were designed, realized and interfaced to the digital signal processor (DSP).

The stator currents of the induction machine were measured by using a LAH 50-P Hall-effect current transducer to provide a galvanic isolation of the detected current signals between the primary and the secondary circuits that is adjusted via a small board for signal conditioning including a protection circuit and A/D converters interface.

The inverter output currents (at the inductor of the LC filter) were measured by using the hall-effect, 120 KHz bandwidth current transformer probe which allows to measure AC and DC currents up to 150A.

The stator line to line voltages of the machine and the DC link voltage were measured by using 25 MHz active differential probes in order to get a higher resolution and a lower noise ratio. The probe allows measuring AC and DC voltages up to 1000 V. The con-

nection between the measured voltage signals above and the A/D buffer circuit was carried out with the use of a shielded cable in order to reduce the effect of noise on the performance of the system.

An incremental encoder with 2048 pulse/revolution was used especially for the purpose of comparison between control schemes with and without the encoder.

The gate drive signals were calculated by the digital signal processor (DSP) by applying a pulse width modulation scheme with a modulation frequency of 50 kHz. They were converted to switching pulses and transmitted to the power part via fiber optic communication interface in order to avoid the influence of EMI.

The communication between the digital signal processor unit and the computer is passed through a built-in standard USB interface.

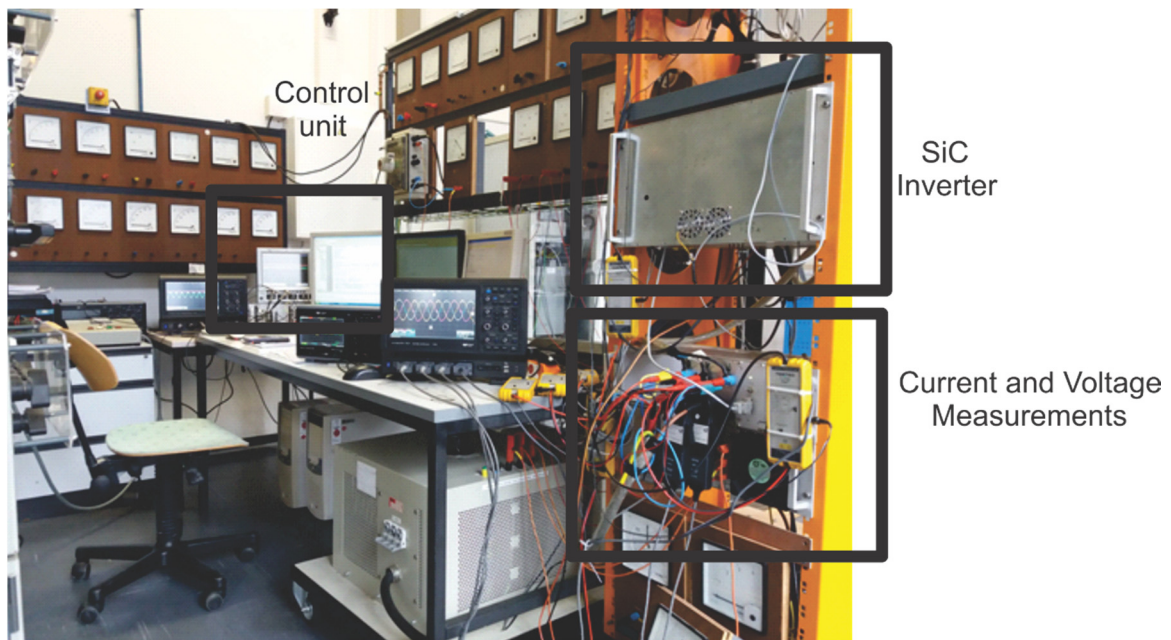


Figure 5-2 View of the inverter and control part of the laboratory set-up

### 5.1.2 SiC two-level inverter

A conventional two-level voltage source inverter equipped with SiC-MOSFETS was especially designed for the experimental laboratory set-up and is shown in Figure 5-3.

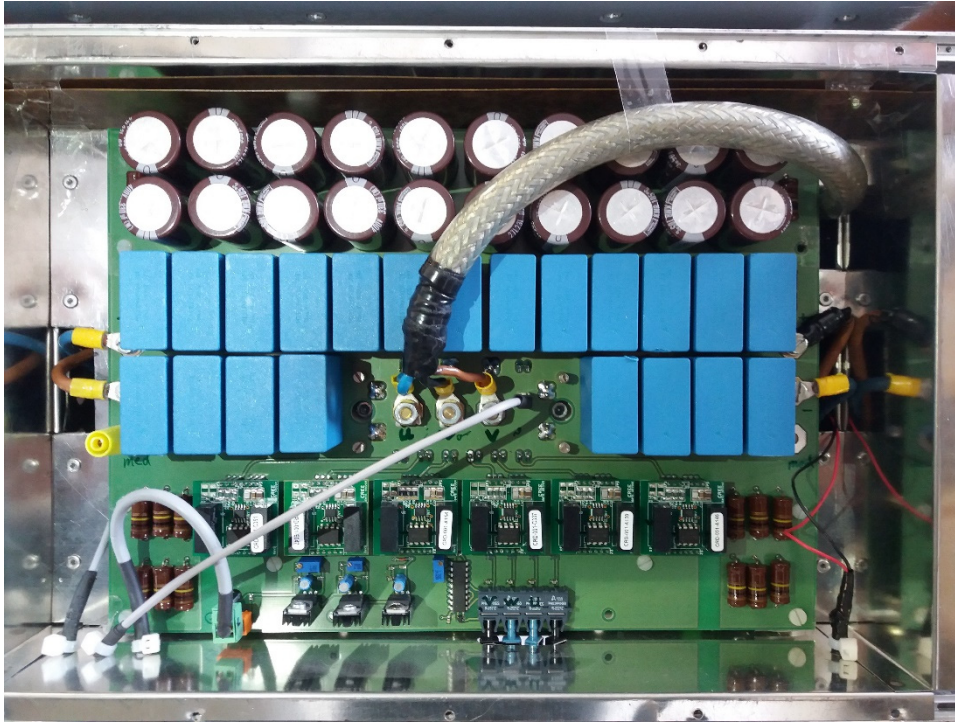


Figure 5-3 Three-phase silicon carbide (SiC) Inverter

One of the important issues to be considered in the design of the inverter is the selection of the power semiconductor switches. After some experiments with silicon carbide JFETS, they were discarded because of some technical limitations, in addition to the fact that the series of switches was discontinued by the manufacturer and there were no spares. Eventually, the CCS020M12CM2 SiC MOSFET 1,2kV/20A module from CREE was selected due to its suitability in dealing with the required design characteristics that are specified in Table 5-1.

Table 5-1 Inverter specifications

DC link voltage, $U_{dc}$	560V
Output power	7.5kW
Switching frequency $f_{sw}$	50kHz

The SiC inverter was constructed by using one of Six-pack model, and by observing all the manufacturer's recommendations regarding a proper assembly as mentioned in section (2.4.4). The DC link capacitor bank of the inverter consists of a combination of the series and parallel connected capacitors. Two groups of capacitors were used in the DC link: The first group contains polypropylene film capacitors, which have low loss characteristics at high switching frequencies with the lowest values of the equivalent inductance and each capacitor has a rating of 16  $\mu$ F. The second group is an arrangement of



electrolytic capacitors and the ratings of each capacitor is  $300\ \mu\text{F}$ . The total capacitance is  $3.636\ \text{mF}$ . Figure 5-4 shows the scheme of the capacitor bank.

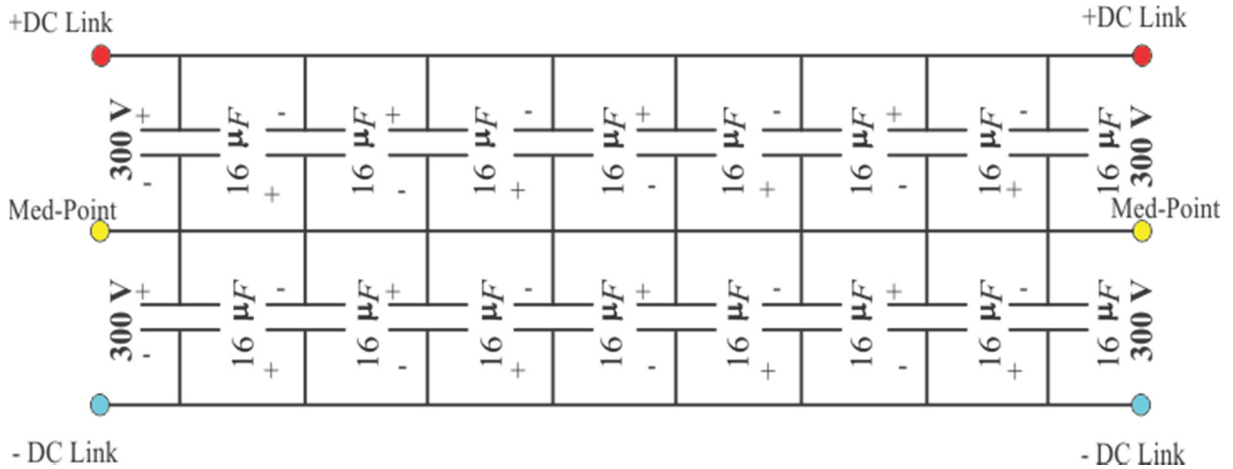


Figure 5-4 Schematic of the printed circuit board (PCB) of the DC-link capacitor bank

In order to avoid a shoot-through in the legs of the SiC-MOSFET-inverter, a dead-time is mandatory in which both the upper and lower switches in a phase-*leg* are off. The dead time was generated in the hardware and set to 250 nanoseconds. The gate driver circuit, dead time generator, and the DC link capacitor bank can be clearly seen in Figure 5-5.

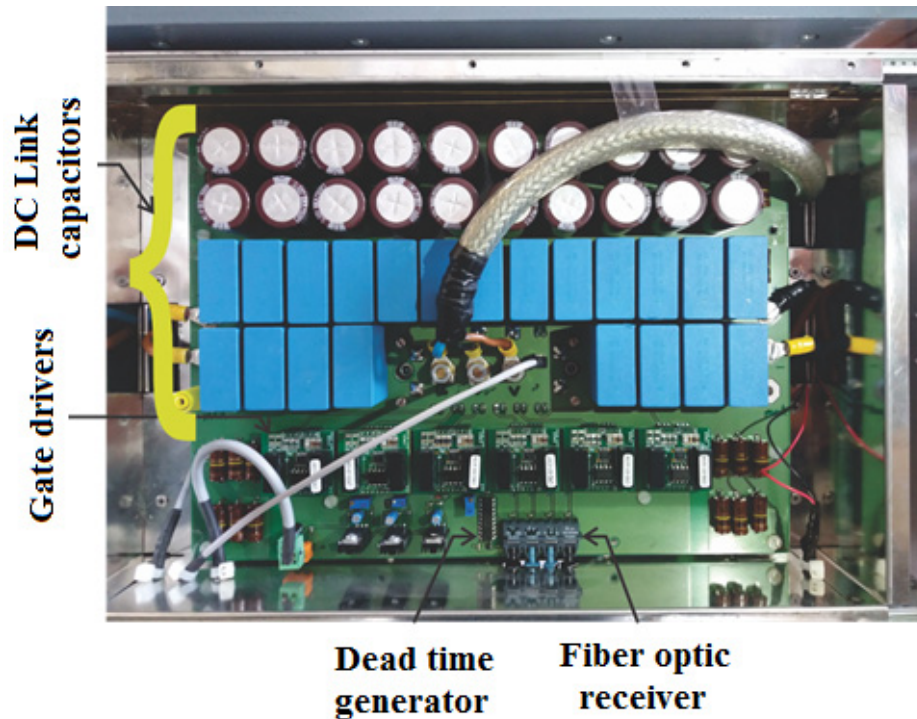


Figure 5-5 Main parts of the driver circuit

The dc-link of the inverter can be fed two different ways: either by a standard three phase rectifier bridge which only permits motor operation, or by a dc source which allows both motor and generator operation. The load machine inverter allows motor or generator operation as well.

### 5.1.3 Induction machine and load

In order to examine the behavior of the enhancement of the sensorless, field oriented control scheme, an induction machine with the data as given in Table 7-1 in the appendix with a built-in encoder was used. The encoder allows an easy commissioning and startup of the induction machine but it is not used once the sensorless control scheme is in operation. Moreover, the encoder provides a reference measurement for the sake of comparison between identification of the speed and encoder operation.

As a load a 21kW commercial servo drive was chosen, the experimental drive used for the investigation of the proposed control schemes was mechanically coupled to the commercial one as shown in Figure 5-6. The data of the induction machine, load machine, and the mechanical coupling are summarized in Table 7-1 in the appendix.

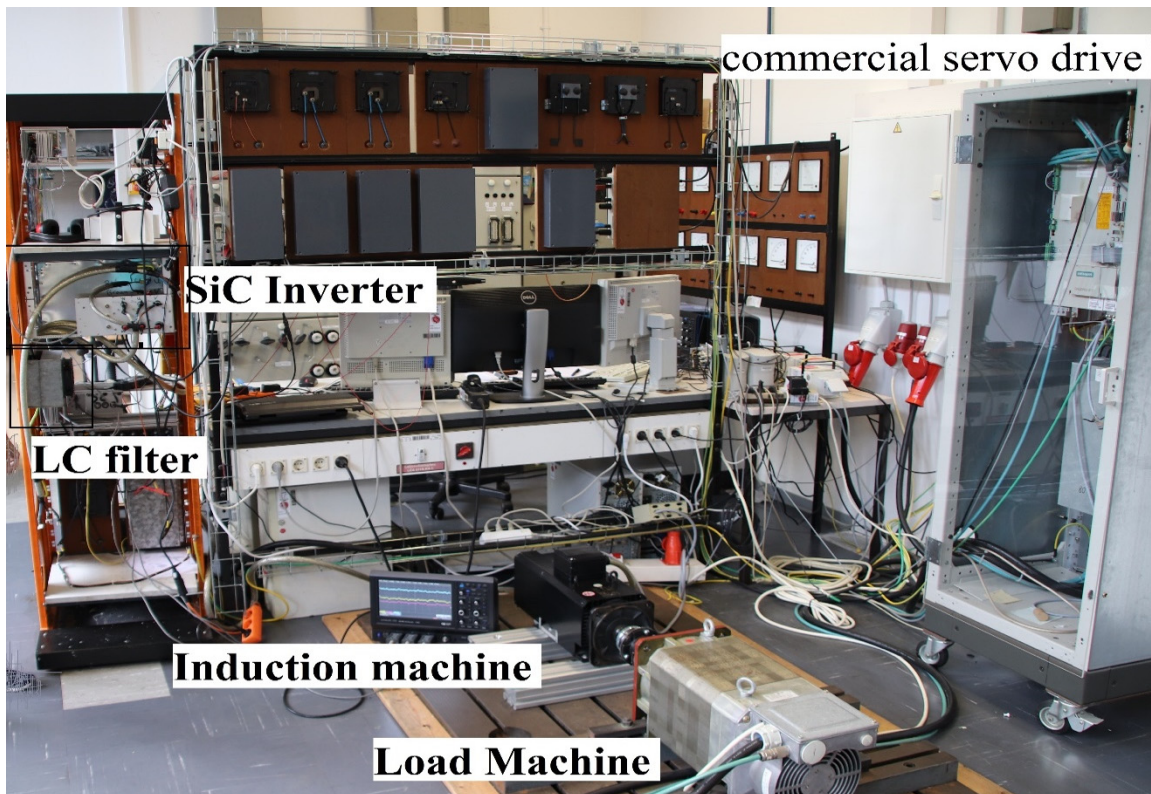


Figure 5-6 Mechanical setups, two induction machines (IMs) mechanically coupled

### 5.1.4 Filter design

One of the main objectives of this work is to obtain sinusoidal voltage by using a LC filter connected at the output of the inverter. As mentioned in sections 1.1, the high switching frequency of the inverter can be advantageous if the output voltages are appropriately filtered and become rather sinusoidal at the terminals of the induction machine.

Due to the high switching frequency inverter, the values of inductance and capacitance of the LC become smaller for the same ripple. In addition the losses are lower since the number of turns decreases.

In the present case for the filter used in the experimental set-up work, the inductors of the filter were constructed by using a standard copper Litz-wire, and the utilized capacitors are polypropylene ones for pulse applications with a rating of 0.22 each one.

The switching frequency of the inverter is  $f_s = 50kHz$  and according to the equations (2.76) and (2.78), the inductor and the capacitor values were set to  $L = 0.1 mH$  and  $C = 1.32 \mu F$  respectively. The cut-off frequency was set to  $14kHz$ . The filter was designed to handle a rated current of  $15 A$ , and a saturation current of  $35 A$ .

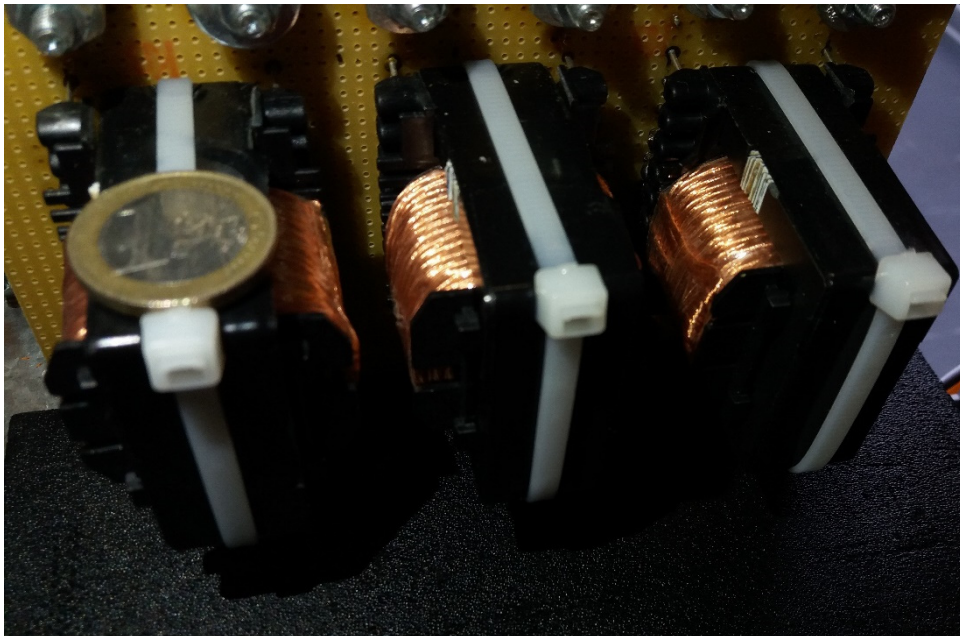


Figure 5-7 Three-phase LC power filter

## 5.2 Experimental results

### 5.2.1 General open loop behavior of voltage model

The experimental results are presented in this section to validate the proposed encoderless control techniques. First, the results of voltage and current measurement at the output of the inverter and on the terminal of the machines are shown. Further measurements show the difference between the measured and the reconstructed voltage as well as the identification of the flux space phasor with and without voltage measurement.

First the SiC inverter was operated with a linear Volts/ Hz open loop control. For practical reasons the DC-link voltage was limited to 300V. The speed was set to  $n = 500 \text{ min}^{-1}$ , the switching frequency of the inverter to 50kHz and the sampling time was 60  $\mu\text{s}$ .

Usually, the output voltage of the conventional two-level inverter is a pulsating one. In the case of an inverter with high switching frequency with a LC filter at the output, an almost sinusoidal voltage can be obtained as shown in Figure 5-8 and Figure 5-9.

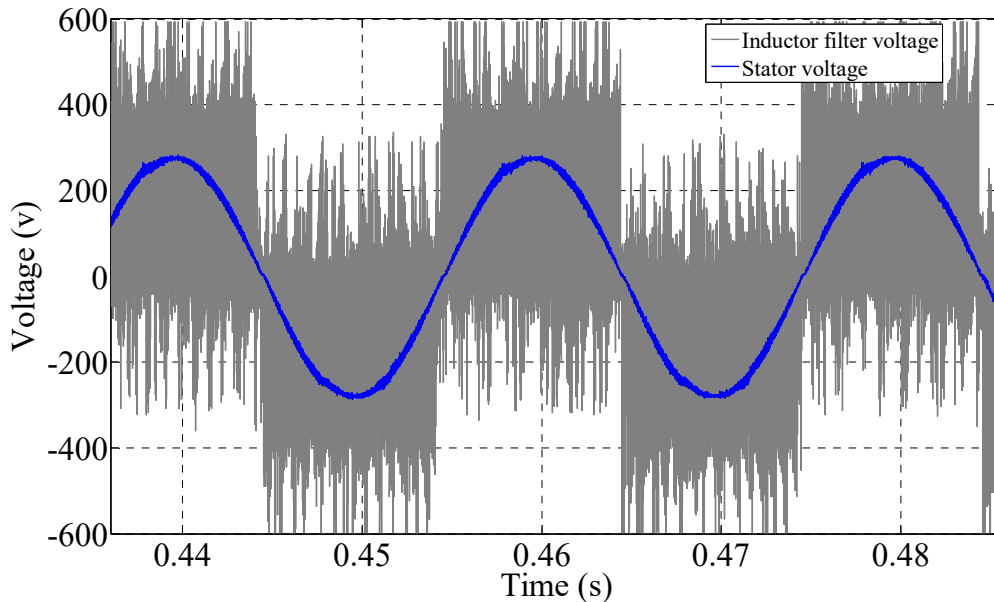


Figure 5-8 Inverter Line-Line voltage before and after the filter



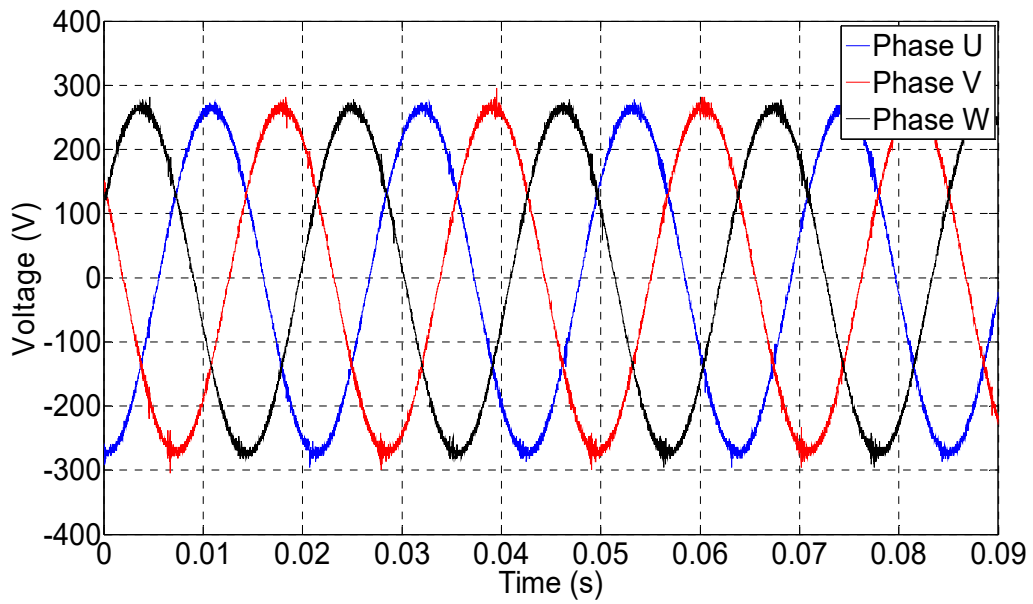


Figure 5-9 Stator voltages

Figure 5-10 depicts the inverter current before the filter, while Figure 5-11 shows the stator current flowing into the induction machine. The quality of the output voltage of the inverter is significantly dependent on the switching frequency. By increasing the switching frequency, the total harmonic distortion would definitely be reduced.

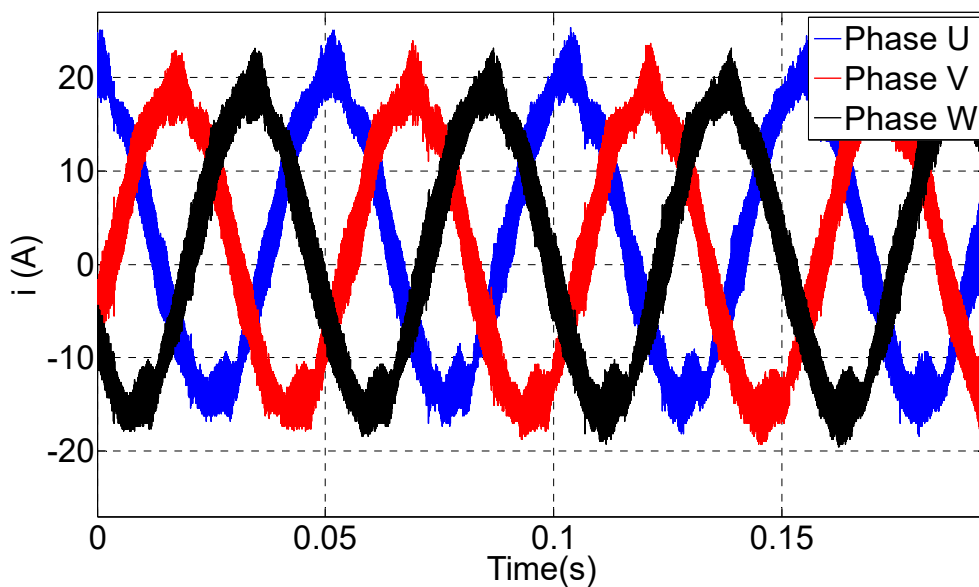


Figure 5-10 Inductor filter currents

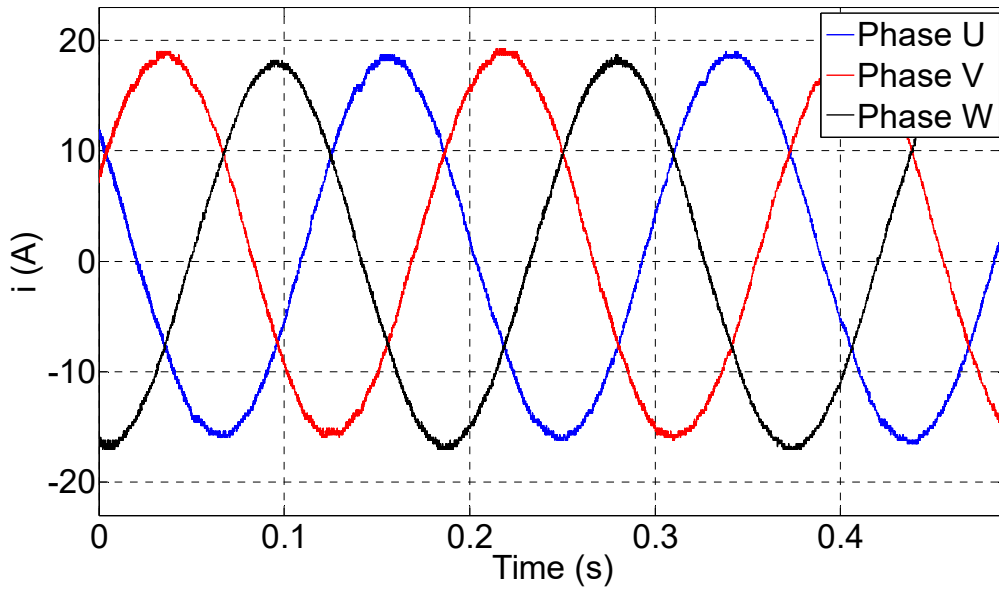


Figure 5-11 Stator currents

As already explained, in the standard voltage model used for the identification of the flux space phasor, the stator voltages are not measured directly, but they are determined from the measured intermediate circuit voltage and from the calculated switching states of the inverter. In particular, the inverter dead time in the legs of the inverter must be taken into account, i.e. the transitional period from one switching state of one phase to the next. Due to this non ideal behavior of the inverter there is an error in the output voltage that can be seen in Figure 5-12 that shows an especial measurement that illustrates the impact of the dead time. For the measurement, the inverter voltage is produced by using a sinus triangle PWM. The reference value of the voltage is sinusoidal and corresponds to the blue curve, yet the mean value of the output voltage is depicted in the red curve. It can be seen that the average voltage around zero exhibits an error caused by the dead time that must be compensated for, otherwise the voltage model is fed with inaccurate input signals. This measurement was carried out on an inverter with Si-IGBTs, the fundamental frequency was  $f_1 = 0.05 \text{ Hz}$  the dead time was  $3 \mu\text{s}$  and the switching frequency  $f_{sw}$  is 5000 kHz. Due to the very low output frequency, the character of the load is mainly resistive and the measured current can be considered to be an excellent approximation of the average value of the voltage.

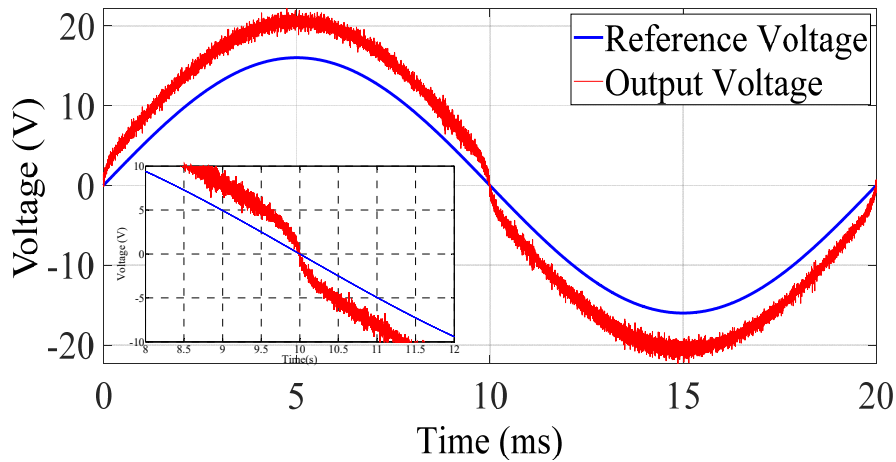


Figure 5-12 Mean value of the output voltage and its reference value in an inverter with standard Si- IGBTs

For the sake of comparison the same measurement was repeated on an inverter with SiC-MOSFET-switches, the dead time was set to 250 nanoseconds and the switching frequency  $f_{sw}$  is 50 kHz. The UDC was in both cases 100 V. Figure 5-13 shows the average output voltage for one period. It is important to notice that there is almost no effect of the dead time in this kind of inverters.

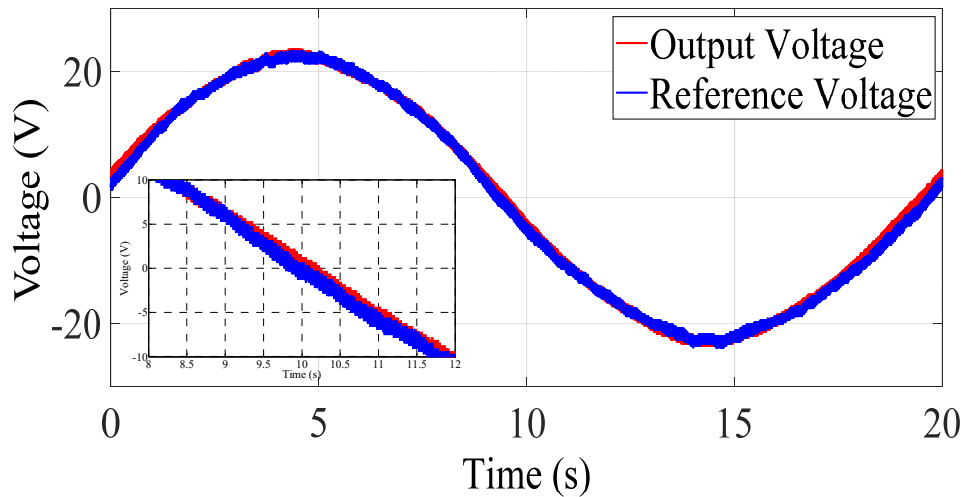


Figure 5-13 The output voltage of the SiC- switches inverter

### 5.2.2 Integration with proportional feedback

As illustrated in section (4.3), the structure of an integrator with proportional feedback corresponds to a first-order low-pass filter. Its transfer function is  $G(s) = \tau / (1 + \tau s)$  and its corner frequency is  $\omega_c = 1/\tau$ . The higher the time constant  $\tau$ , the lower the corner

frequency  $\omega_c$  and the higher the gain  $\tau$ ; i.e. the transfer function has a lower damping and if there is an eccentricity in  $\alpha, \beta$  -fluxes, the eccentricity is not damped well. On the other hand, the low-pass filter behaves like the integrator for lower frequency. Figure 5-14 shows the frequency response of two integrators with the time constant  $\tau = 0.1\text{ s}$  and  $\tau = 1\text{ s}$  that are used in the standard voltage model and in the enhanced voltage model respectively. So that  $\tau$  was selected as great as possible, but so small as necessary because of the necessary damping.

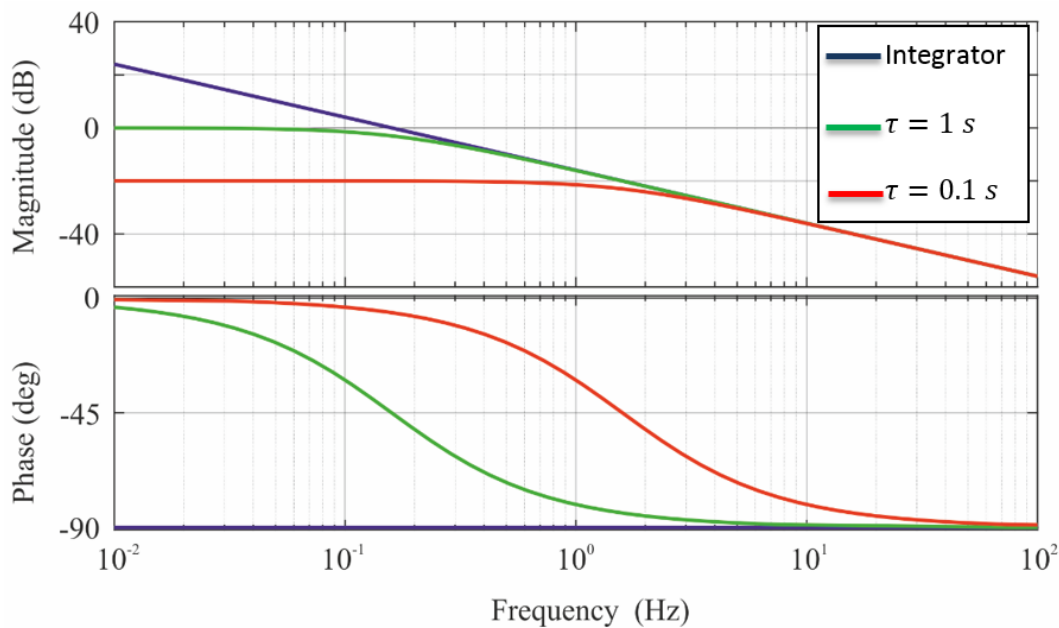


Figure 5-14 Frequency response of two different integrators with p-feedback

The experiments have shown that  $\omega_c$ , the corner frequency of the LPF can be set to a lower value by using the enhanced voltage model (EUM). In this way, the integration yields better results and a more stable operation in the low frequency range. In the current experimental setup, the time constant  $\tau$  of the standard model (UM) is set to  $0.1\text{ s}$  while it is set to  $1\text{ s}$  in the case of enhanced voltage model (EUM). The rotor flux in  $\alpha, \beta$  -coordinates is shown in Figure 5-15 and Figure 5-16, both at no load and  $15\text{ Nm}$  load respectively. The results were collected at a speed equal to  $300\text{ min}^{-1}$ .

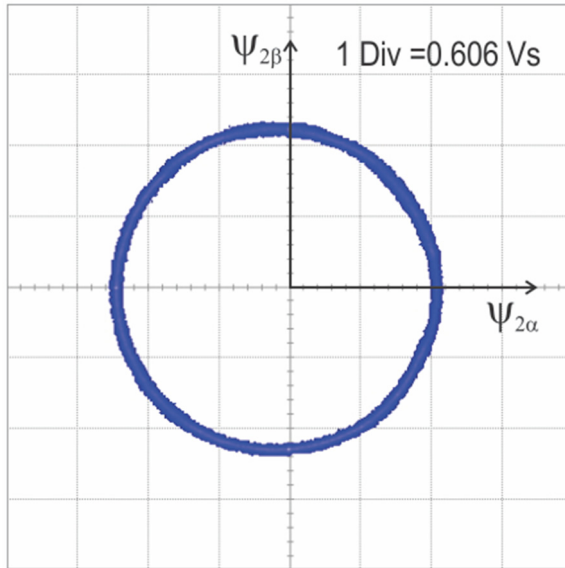


Figure 5-15 Rotor flux space phasor in  $\alpha, \beta$ -coordinates obtained with the SUM, at no load,  $n=300\text{min}^{-1}$

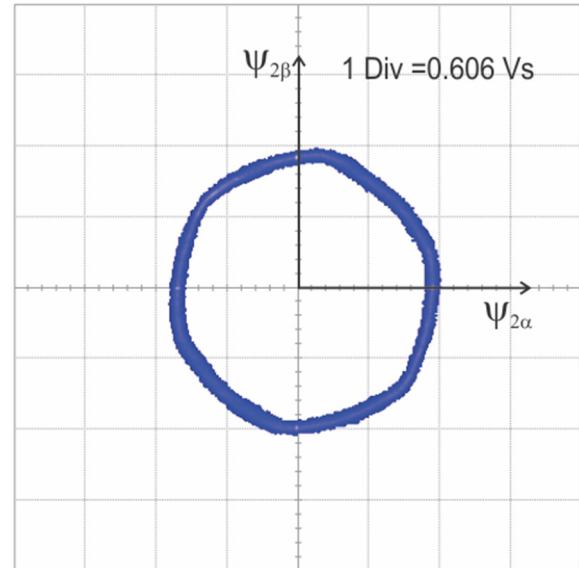


Figure 5-16 Rotor flux space phasor in  $\alpha, \beta$ -coordinates obtained with the SUM, at 15 Nm load,  $n=300\text{min}^{-1}$

For the enhanced UM, the time constant  $\tau$  is set to 1 s, the rotor fluxes in coordinate system at no load and at 15 Nm load are depicted in Figure 5-17 and Figure 5-18.

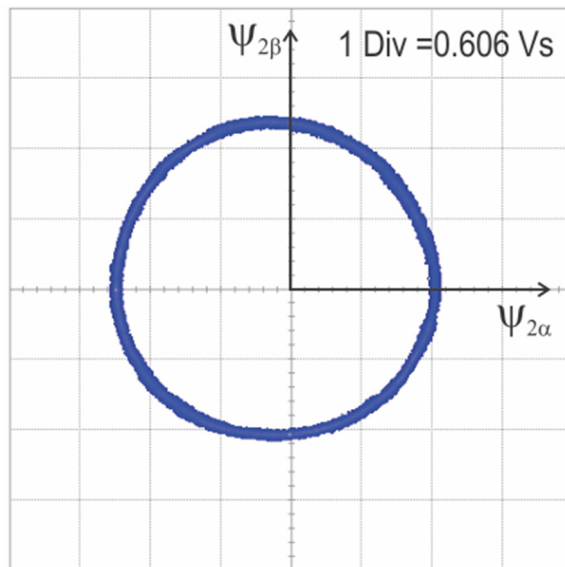


Figure 5-17 Rotor flux space phasor in  $\alpha, \beta$ -coordinates obtained with the EUM, no load,  $n=300\text{min}^{-1}$

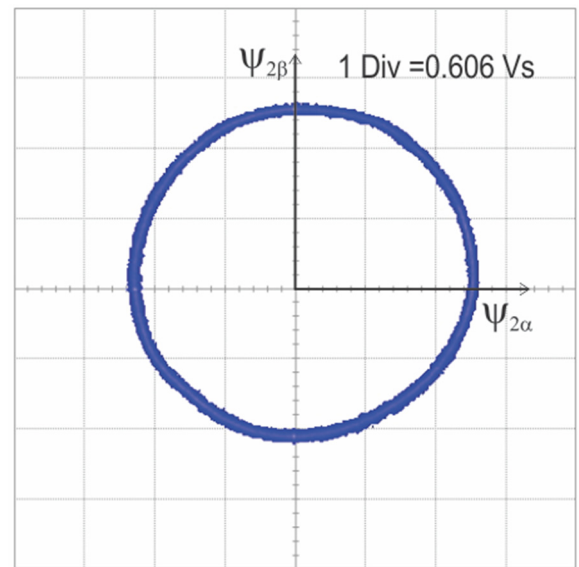


Figure 5-18 Rotor flux space phasor in  $\alpha, \beta$ -coordinates obtained with the EUM, 15 Nm load,  $n=300\text{min}^{-1}$

The rotor flux space phasor in  $\alpha, \beta$ -coordinates is obtained by using the SUM and the EUM are presented in Figure 5-19 and Figure 5-20. The measurements are carried out at a speed of  $15 \text{ min}^{-1}$  and confirm that the presented method in this experiment can

work down to lower frequencies, and that the traces of the flux are kept centered and closer to the circular shape with the EUM, while they take a hexagonal shape in case of the SUM.

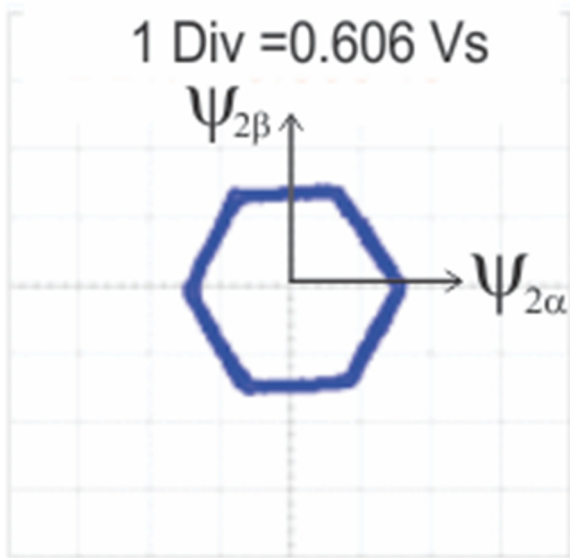


Figure 5-19 Rotor flux space phasor in  $\alpha, \beta$ -coordinates obtained with the SUM at  $15 \text{ min}^{-1}$  and load=5 Nm

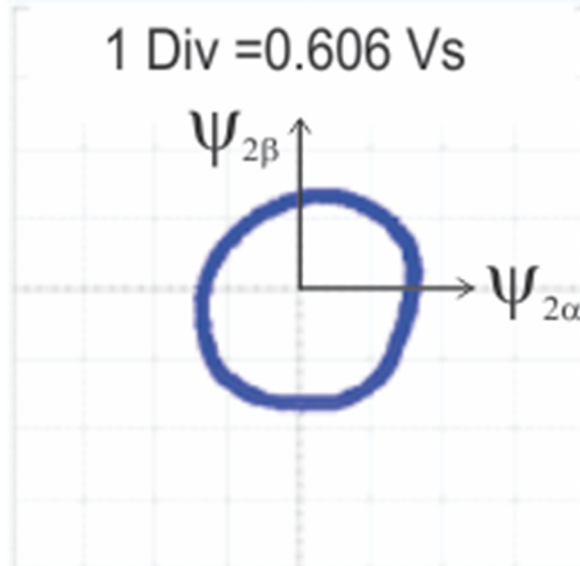


Figure 5-20 Rotor flux space phasor in  $\alpha, \beta$  polar coordinates by using the EUM at  $15 \text{ min}^{-1}$ , load=5 Nm

### 5.2.3 Field oriented control schemes

The following experimental results were obtained in a closed loop field oriented control scheme implemented according to the classical model as discussed in (3.2.2). The experiments were carried out within the parameters and settings as presented in the appendix.

#### 5.2.3.1 Identification of the rotor flux space phasor

The next series of experiments is related to the identification of the rotor flux space phasor. As already explained in previous sections, in field oriented control techniques the voltage model can be used almost without restrictions in the high-speed range. For the following measurements the drive was operated by using the current model with an encoder as basis of comparison. The induction machine was operated with a field oriented control under no load conditions and the orientation angle obtained with a conventional current model. Figure 5-21 to Figure 5-28 show the rotor flux space phasor of the induction machine in  $\alpha, \beta$ -coordinates, calculated by means of the voltage model, at

constant speed of  $n^* = 500 \text{ min}^{-1}$  as well as for the case of low speed of  $n^* = 10 \text{ min}^{-1}$ . For the sake of a qualitative comparison the flux space phasor was calculated based on the current model as well and depicted in the same figure.

At high speed,  $n^* = 500 \text{ min}^{-1}$ , the voltage model behaves like a current model, i.e. the similarity in the behavior becomes clear from the experimental results illustrated in Figure 5-21.

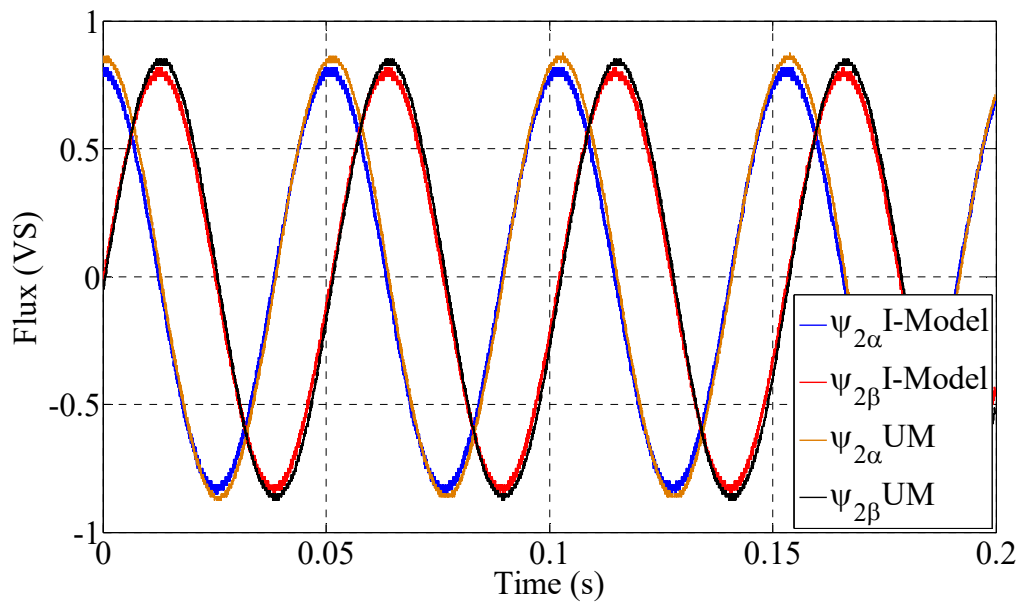


Figure 5-21 Rotor flux space phasor in  $\alpha, \beta$ -coordinates obtained with the SUM and with the current model at  $n=500 \text{ min}^{-1}$

As expected at a low speed,  $n = 10 \text{ min}^{-1}$ , the SUM shows a very weak behavior as it can be seen in Figure 5-22. The physical explanation for that is that the induced voltage at low speed is very low and in the order of magnitude of the errors caused by the imperfections of the inverter. For the measurements of the stator voltages fed to the voltage model were reconstructed by using the output of the current controller.

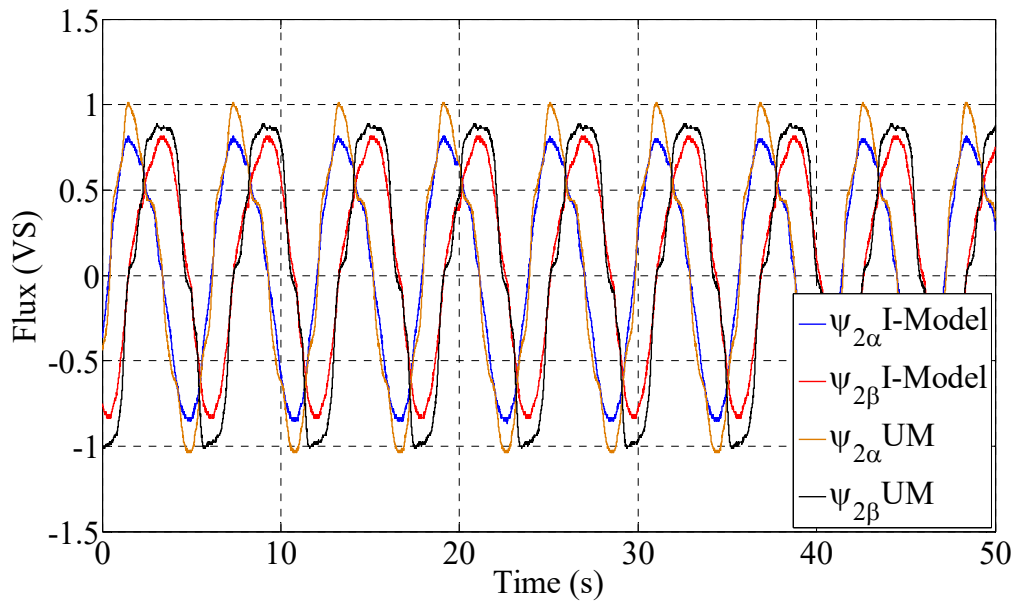


Figure 5-22 Rotor flux space phasor in  $\alpha, \beta$ -coordinates obtained with the SUM and with the current model at  $n=10 \text{ min}^{-1}$

As already mentioned a number of times, the main objective of this work is the investigation of a possible enhancement of the voltage model by using the voltages measured at the terminals of the induction machine. For the following series of experiments an almost sinusoidal voltage was obtained by adding a LC filter at the output of the inverter, which was used instead of the reconstructed in order to enhance the voltage model. Figure 5-23, shows the rotor flux space phasor in  $\alpha, \beta$ -coordinates obtained with the EUM and with the current model at  $n=500 \text{ min}^{-1}$ . The EUM shows very good results which look like those of the current model; i.e. the experimental results in Figure 5-23 confirm the good performance of the enhanced voltage model at higher speed.



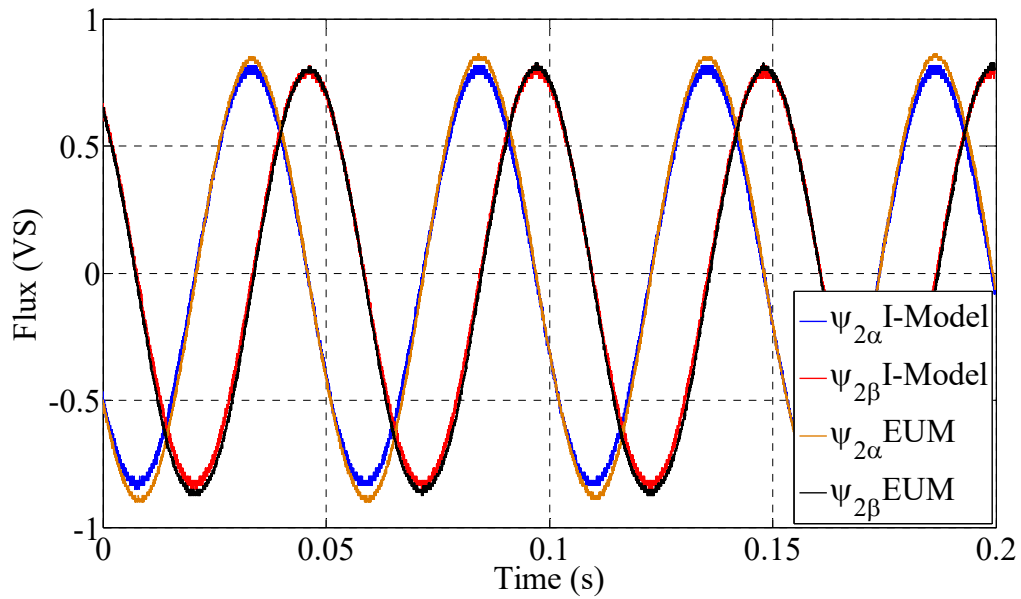


Figure 5-23 Rotor flux space phasor in  $\alpha, \beta$ -coordinates obtained with the EUM and with the current model at  $n=500 \text{ min}^{-1}$

Unlike the results, which are obtained from the classical voltage model that is presented in Figure 5-22, the enhanced voltage model shows better behavior at low speed,  $n=10 \text{ min}^{-1}$ . Rotor flux space phasor in  $\alpha, \beta$ -coordinates obtained with the EUM and with the current model at  $n=10 \text{ min}^{-1}$  is presented in Figure 5-24.

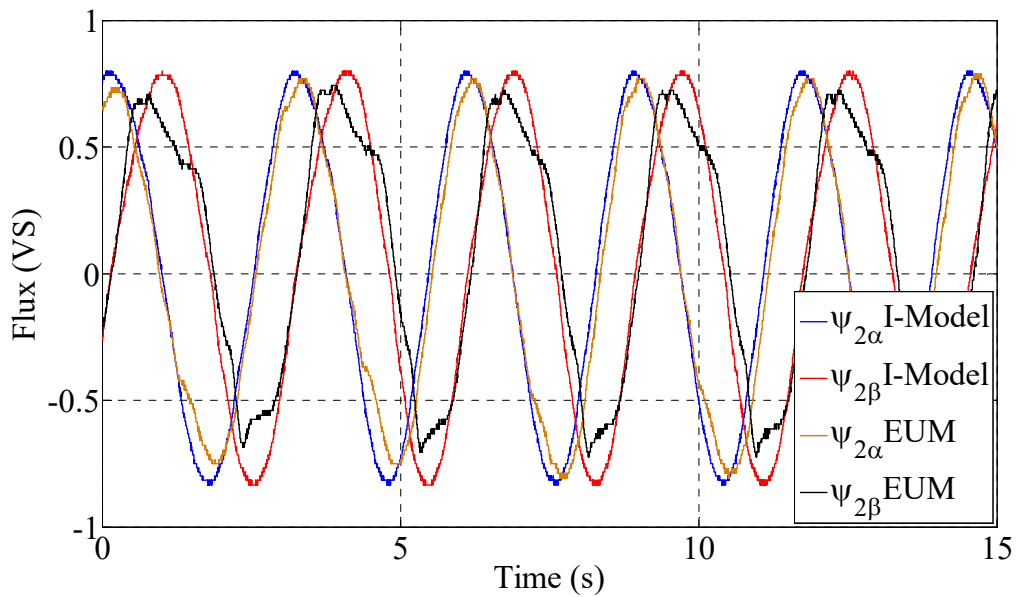


Figure 5-24 Rotor flux space phasor in  $\alpha, \beta$ -coordinates obtained with the EUM and with the current model at  $n=10 \text{ min}^{-1}$

A further topic examined in this work is the behavior of the sensorless natural field orientation (NFO) control scheme for the induction machine. This technique allows the machine to work until a minimum stator frequency. This model was presented in section 3.2.2) and was promoted in the literature as suitable control scheme for the induction machine.

The rotor flux space phasor in  $\alpha, \beta$ -coordinates obtained with the NFO and with the current model at  $n=500 \text{ min}^{-1}$  can be seen in Figure 5-25. The measurement show no notable difference between NFO and the above shown measurements.

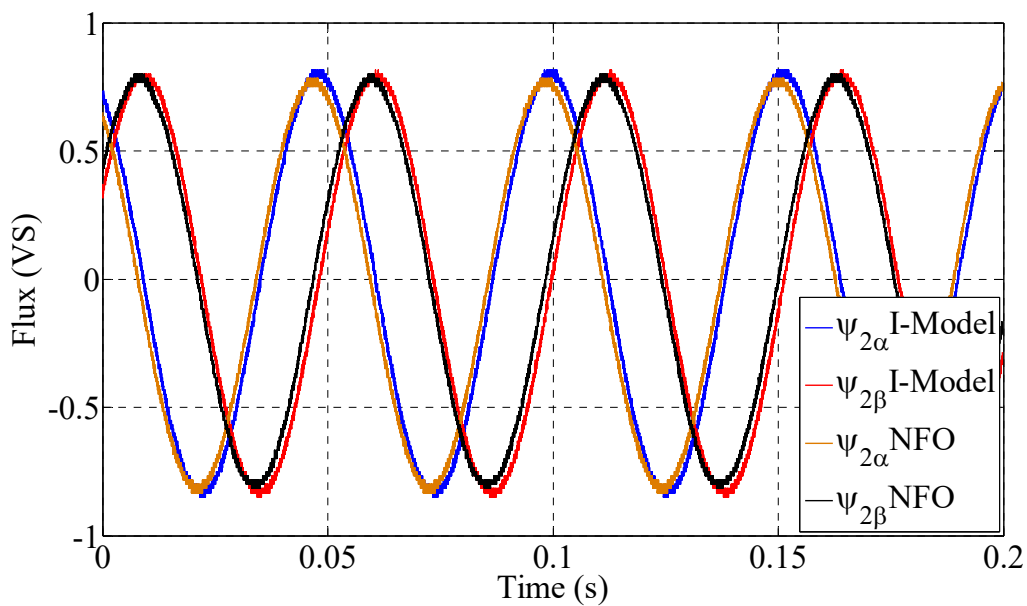


Figure 5-25 Rotor flux space phasor in  $\alpha, \beta$ -coordinates obtained with the NFO and with the current model at  $n=500 \text{ min}^{-1}$

The efficient NFO control technique for the induction machine can also be used in the lower frequency range. Thus, the speed was set to  $n=10 \text{ min}^{-1}$ , and the rotor flux space phasor was calculated by the NFO model and is presented in Figure 5-26. This model produces very good results as compared with the classical voltage model, as demonstrated in before mentioned figure.

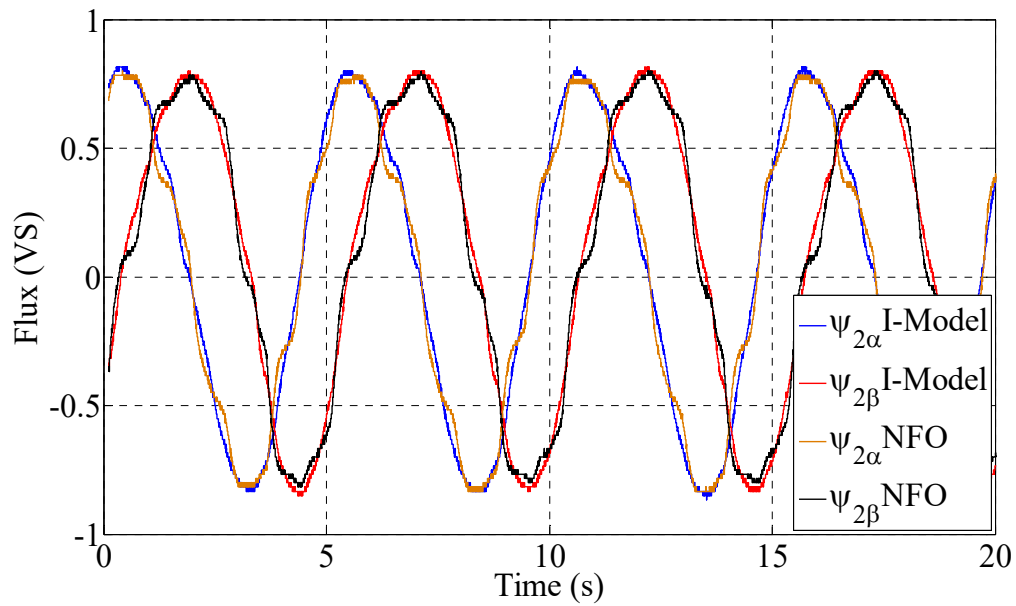


Figure 5-26 Rotor flux space phasor in  $\alpha, \beta$ -coordinates obtained with the NFO and with the current model at  $n=10 \text{ min}^{-1}$

Again the benefits of obtaining almost sinusoidal currents and voltages from an inverter equipped with silicon carbide (SiC)-switches and an output filter were examined for the case of the NFO. The almost sinusoidal output voltages can be used to calculate the induced voltages of the induction machine in the NFO model instead of using the reconstructed ones. Figure 5-27 exhibits the rotor flux that obtained from both the current model and from the enhanced NFO (ENFO). In this case, the speed was  $n= 500 \text{ min}^{-1}$ , which is the higher-speed case.

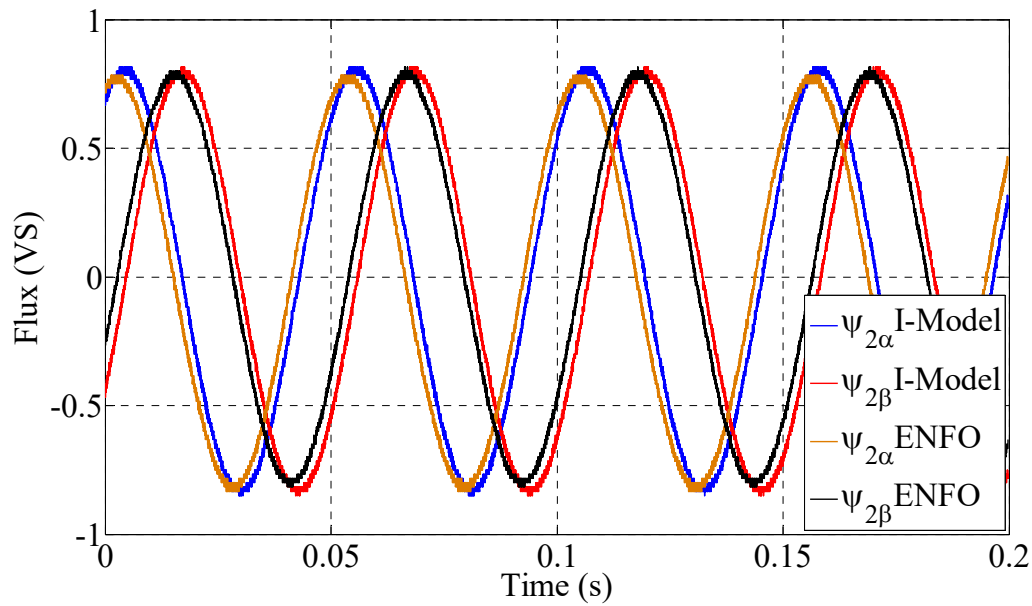


Figure 5-27 Rotor flux space phasor in  $\alpha, \beta$ -coordinates obtained with the ENFO and with the current model at  $n=500 \text{ min}^{-1}$

For the assessment of the lower speed range, the reference speed was reduced to  $n=10 \text{ min}^{-1}$ , and the system was tested under the same conditions; the enhanced NFO (ENFO) model gives some improvement in extending the range of operation of a sensorless field oriented control scheme. Figure 5-28 displays the rotor flux space phasor in  $\alpha, \beta$ -coordinates obtained with the ENFO and with the current model at  $n=10 \text{ min}^{-1}$ .

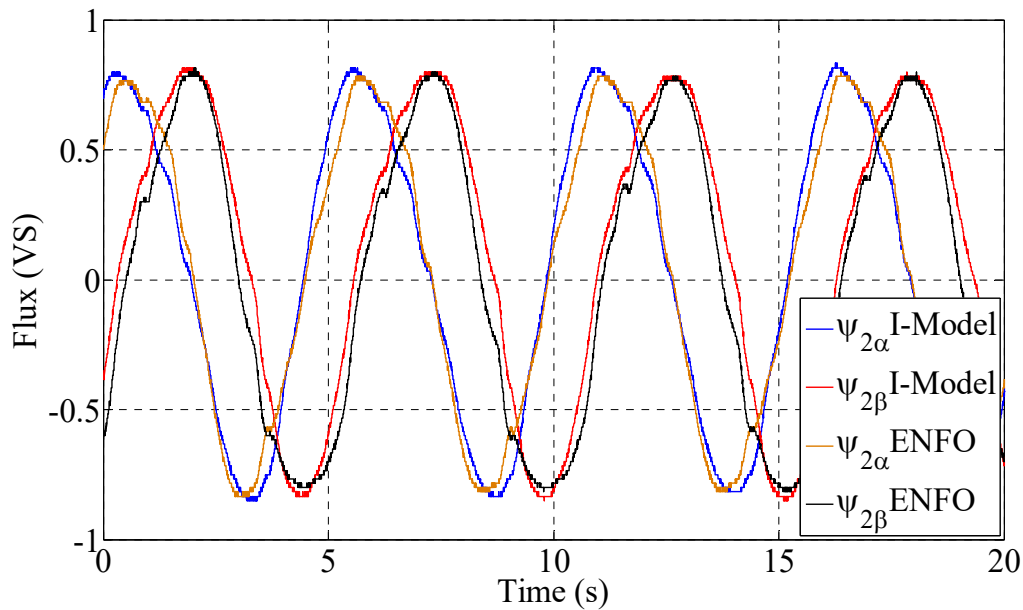


Figure 5-28 Rotor flux space phasor in  $\alpha, \beta$ -coordinates obtained with the ENFO and with the current model at  $n=10 \text{ min}^{-1}$

### 5.2.3.2 Field oriented torque control with different voltage models

This section focus on the experimental analysis of the encoder-less field oriented control by using different models for the identification of the rotor flux space phasor considered above.

First, a classical field oriented control scheme according to 3.1.1 that utilizes different voltage models for the calculation of the stator and the rotor flux space phasor was implemented. The drive could be actively loaded by a servo 7.5 kW dynamometer with high dynamics that is rigidly coupled to the unit under test. The current model with measured mechanical rotor position was used in most of the measurements only for the sake of comparison. The control loop was closed by using the methods considered in the previous sections.

In the following experiments, the drive used as a load is operated in speed control mode while the induction machine under test is operated in torque control mode with a constant torque producing current  $i_{1q}$  equal to its maximum value for each velocity point. The speed of the braking machine was progressively reduced from  $500 \text{ min}^{-1}$  down to zero and the torque of the induction machine under test was measured. The experiments were repeated for five different models: current model (with encoder as the base of com-

parison), standard voltage model, enhanced voltage model, standard natural field orientation (NFO Model) which uses the reconstructed terminal voltages and enhanced natural field orientation (ENFO Model) that uses the voltages measured on the terminals of the induction machine. In all cases, as it can be observed in Figure 5-29, the same stator current was applied but different torque values result due to the imprecise models. The higher the torque the better the model. Figure 5-29 show the results of these experiments.

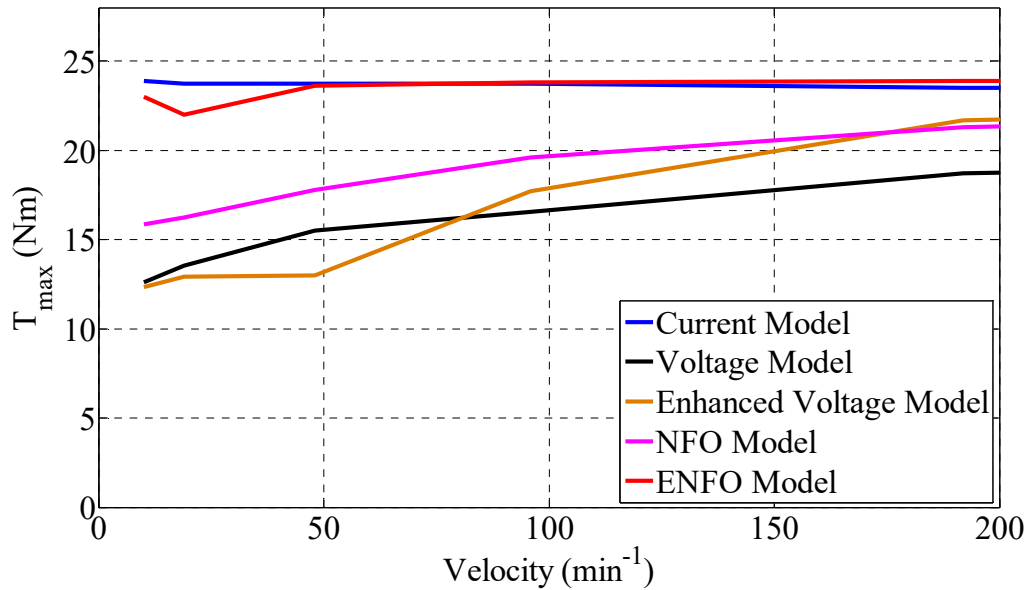


Figure 5-29 Relationship between the maximum achievable value of the produced torque at constant current  $i_{1q}$  and the speed for different models

It can be clearly seen that the enhanced natural field orientation (ENFO Model) shows a similar behavior to the current model and can better handle higher torque values especially at lower operating speeds.

In an additional experiment the case of a speed reversal of the load machine, while the induction machine is operated in torque control mode (same operation mode as in the previous case) by using ENFO, was examined. Figure 5-30 to Figure 5-34 show the results of the mechanical speed, the mechanical angle of the rotor shaft, the identified angular position of the rotor flux space phasor, the phase currents of the machine and the torque producing component  $i_{1q}$  of the stator current space phasor that is kept at its maximum value.

The measurements of the steady state and the dynamic performance of the encoder-less enhanced natural field orientated control scheme (ENFO) in torque operation mode is better than all the other examined schemes under the same test conditions.

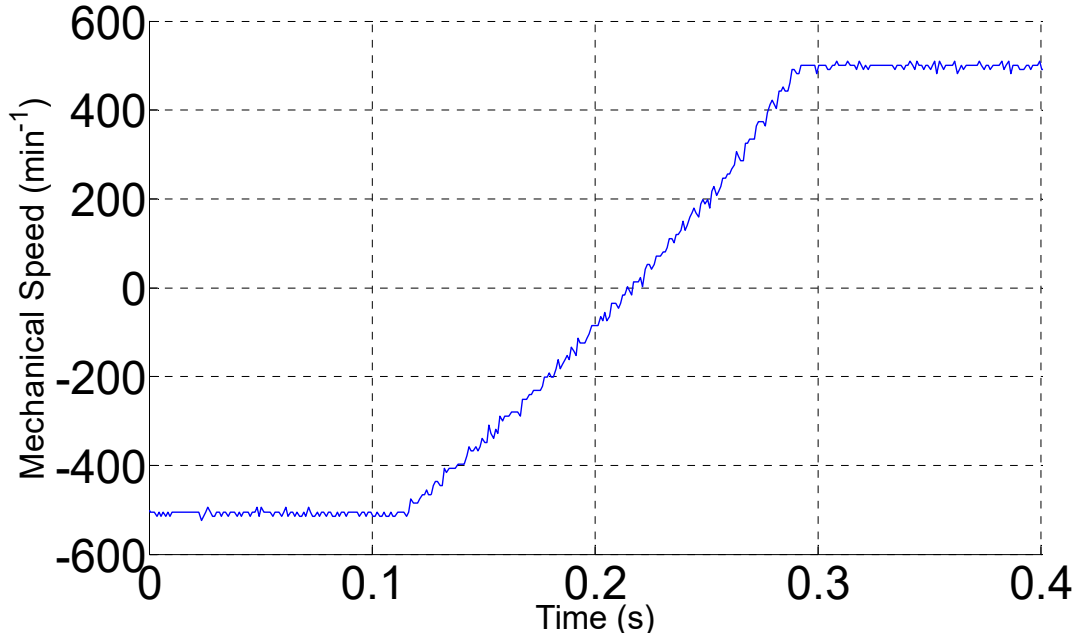


Figure 5-30 Speed for a speed reversal between  $-500 \text{ min}^{-1}$  and  $500 \text{ min}^{-1}$

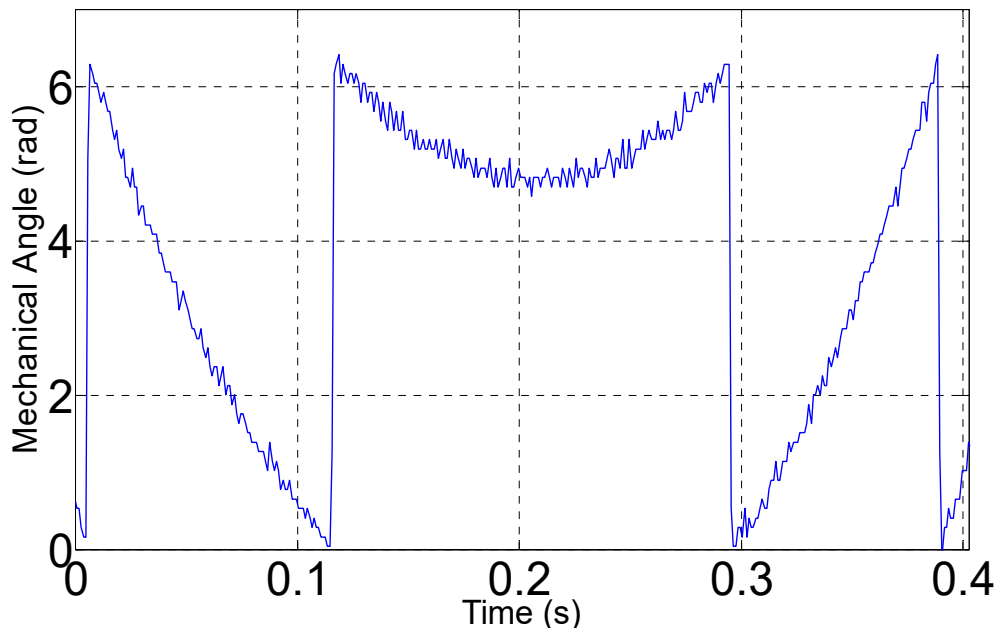


Figure 5-31 Mechanical angle  $\gamma$  of the rotor shaft between  $-500 \text{ min}^{-1}$  and  $500 \text{ min}^{-1}$

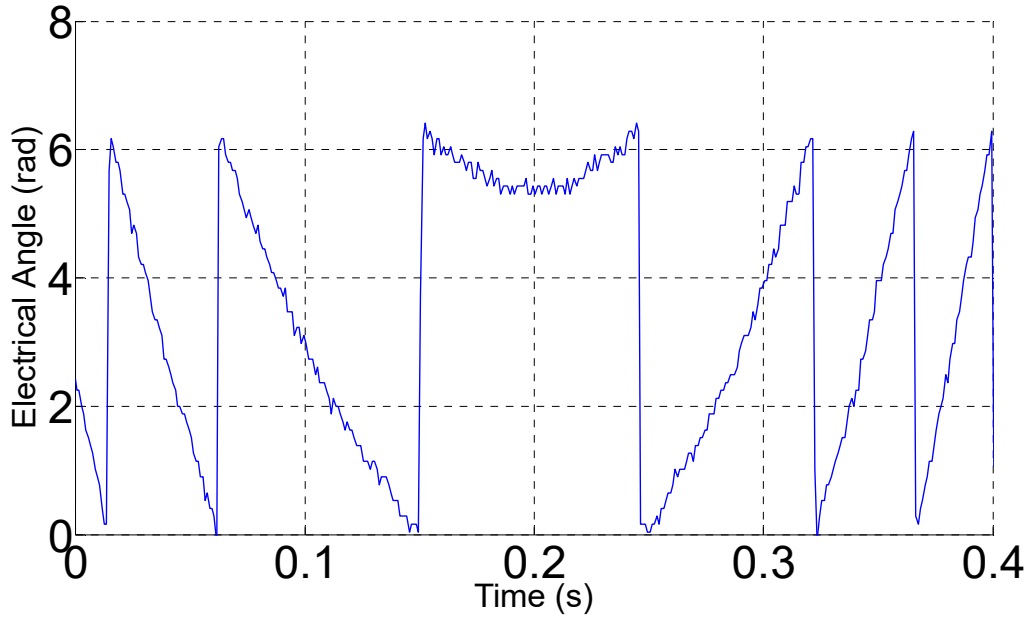


Figure 5-32 Orientation angle  $\Phi_2$  for a speed reversal between  $-500 \text{ min}^{-1}$  and  $500 \text{ min}^{-1}$

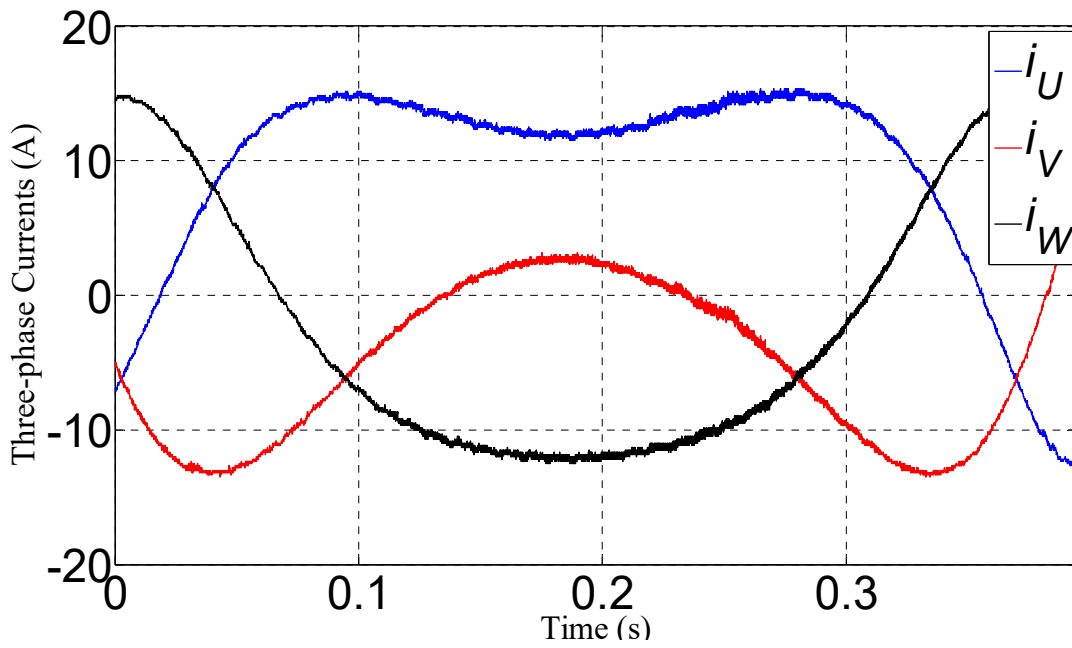


Figure 5-33 Stator currents for a speed reversal between  $-500 \text{ min}^{-1}$  and  $500 \text{ min}^{-1}$



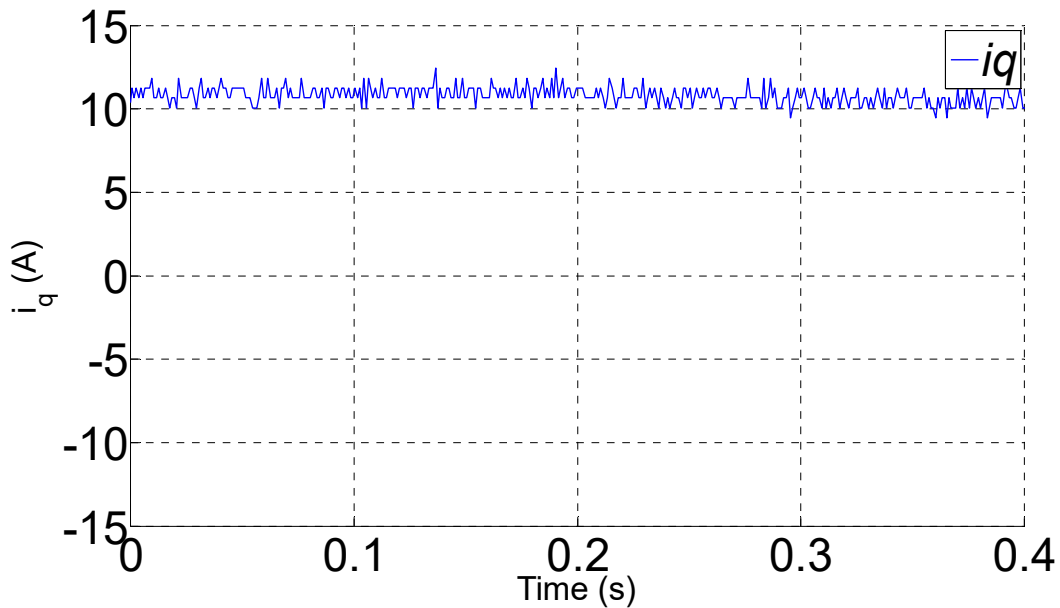


Figure 5-34  $i_{1q}$  for a speed reversal between  $-500 \text{ min}^{-1}$  and  $500 \text{ min}^{-1}$

#### 5.2.4 Model reference adaptive system

Although the mechanical speed of the drive can be obtained by using (3.36), the sensorless control of the speed under the NFO scheme was very sensitive to parameter variations and was therefore discarded. Thus, work was subsequently focused on a Model Reference Adaptive Control (MRAC) that uses the measured terminal voltage and delivers better results.

The results presented in this section show the encoder-less operation by using a classical model reference adaptive system. The following experimental results show the behavior of the implemented control for different reference systems: the standard voltage model (SUM), enhanced voltage model (EUM), natural field orientation (NFO) and enhanced natural field orientation (ENFO).

In the next series of experiments the model reference adaptive system as presented in section (4.3) was selected to obtain the position of the rotor flux space phasor and the speed of the machine and to perform a field oriented control of the drive. As shown in Figure 3-12, the basic structure of the MRAS consists of two models: the current model as an adaptive model and the voltage model as a reference model. In order to extend the range of the MRAS, a reference enhanced voltage model is defined which is fed with measured (instead of calculated stator) voltages. The standard current model based on

the measured rotor position was used as a base model for the sake of comparison in most measurements.

The first series of experiments were dedicated to the comparison among the standard voltage model (SUM), enhanced voltage model (EUM), natural field orientation and enhanced natural field orientation in steady state and in dynamic behavior.

#### 5.2.4.1 Steady state behavior of the MRAS with different reference model

In the following experimental results, the induction machine under examination was in speed control mode while the load machine was set to torque control mode. The speed of the machine was progressively reduced from  $500 \text{ min}^{-1}$  down to zero and the load torque was adjusted to its desired value. Two different cases of load were examined, a low load at  $i_q = 2 \text{ A}$  ( $M_L \approx 15\% M_N$ ) and high load at  $i_q = 12$  ( $M_L \approx 90\% M_N$ ). The average error ( $\Delta n$ ) between the measured speed and the identified speed was calculated during the experiments.

The measurements were repeated for the four different models as reference models. Figure 5-35 shows the results of the speed control mode at low load of  $i_q = 2 \text{ A}$  ( $M_L \approx 15\% M_N$ ). It can be clearly seen that the enhanced natural field orientation (ENFO Model) shows the best behavior in the test when it is used as a reference model especially in the low speed range.

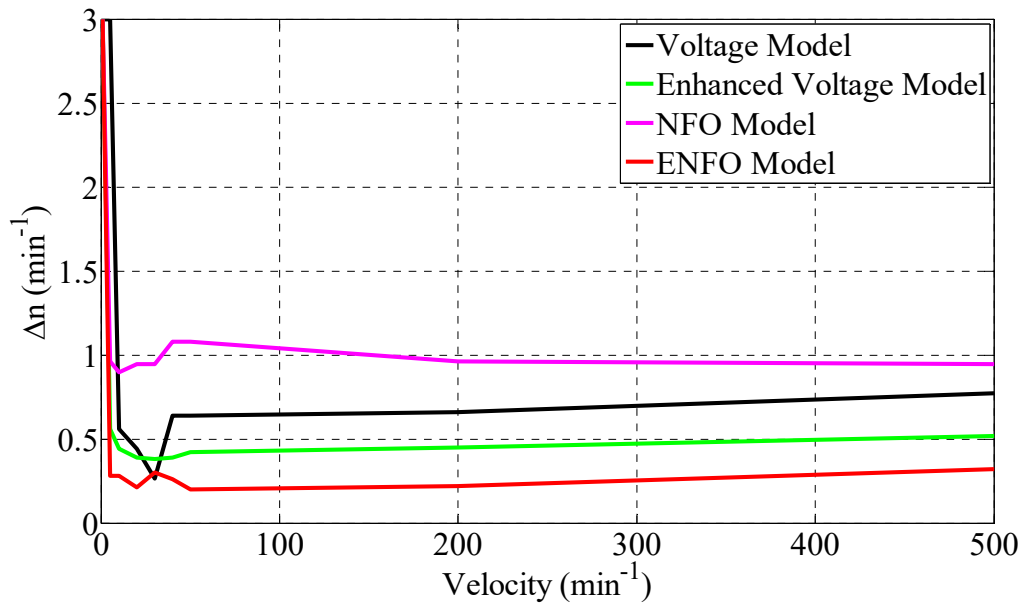


Figure 5-35 Relationship of the average error ( $\Delta n$ ) between the measured and the identified speed and for different speeds and models at  $i_q=2A$  ( $M_L \approx 15\%M_N$ )

Further tests were carried out for a higher load of  $i_q = 12 A$  ( $M_L \approx 90\%M_N$ ). When using the standard natural field orientation (NFO Model), fed by the reconstructed terminal voltages as a reference model, the average speed error ( $\Delta n$ ) between the measured speed and the identified speed shows the worst results, whereas MRAS shows the minimum average speed error ( $\Delta n$ ) when using the enhanced natural field orientation model (ENFO).

Figure 5-36 show the relationship between average error ( $\Delta n$ ) between the measured and the identified speed and for different speeds and models at  $i_q=12A$  ( $M_L \approx 90\%M_N$ ).

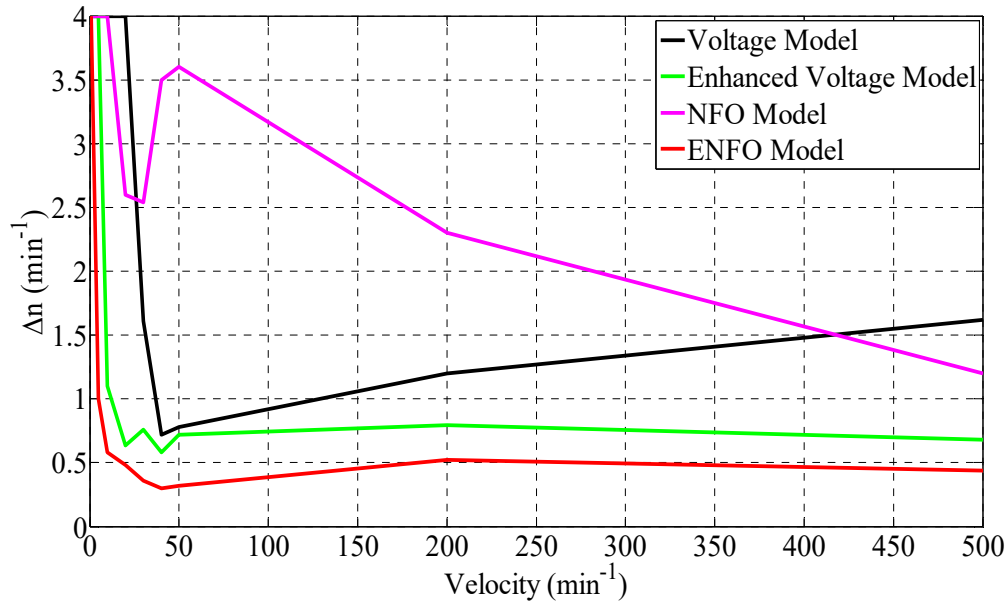


Figure 5-36 Relationship between average error ( $\Delta n$ ) between the measured and the identified speed and for different speeds and models at  $i_q=12A$  ( $M_L \approx 90\%M_N$ )

These experimental results carried out on the laboratory setup confirm that a significant enhancement of the steady behavior of the MRAS control scheme can be achieved if the voltages measured on the terminals of the machine are fed to the different models instead of the calculated ones. The best results in this series of experiments were obtained with the natural field orientation model fed with the measured stator voltages.

## 5.2.4.2 Dynamic behavior

### 5.2.4.2.1 Speed Reversal

For this experiment, the control of the drive system was carried out without a speed encoder by using the enhanced natural field orientation in an MRAS and a field oriented control scheme. The speed reference was changed from a set point of  $n^* = -300 \text{ min}^{-1}$  to of  $n^* = 300 \text{ min}^{-1}$ . The estimated speed value from the MRAS was used instead of the actual speed value for the speed control. The results are illustrated in Figure 5-37 to Figure 5-40, which show the reference and the actual speed, the stator current component  $i_{1q}$  that is responsible to produce torque and is kept at its maximum value, the identified angular position of the rotor flux space phasor and the phase currents of the machine. The measurements have shown that the steady state and the dynamic performance of the encoder-less enhanced natural field orientated control scheme (ENFO) in speed

control mode is better than all the other examined schemes under the same test conditions.

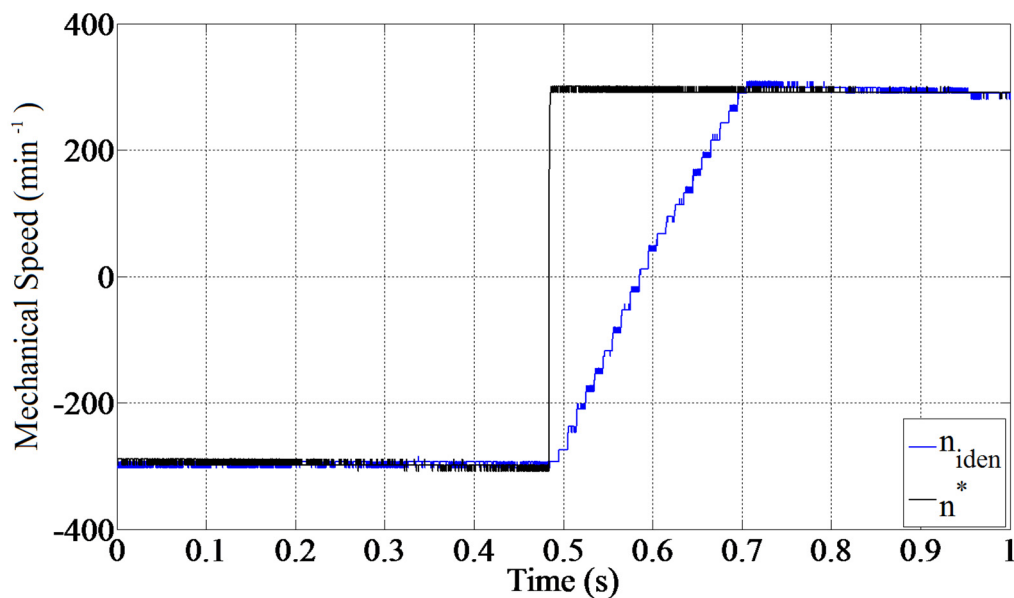


Figure 5-37 Reference and estimated speed during speed reversal at 300 min<sup>-1</sup>

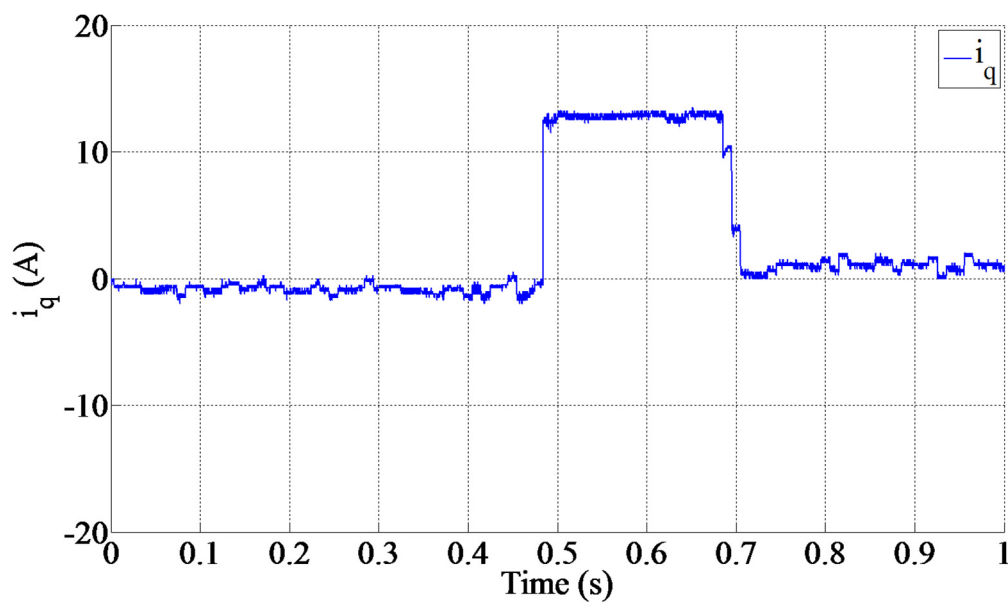


Figure 5-38 Torque producing component of the stator space phasor during speed reversal at 300 min<sup>-1</sup>

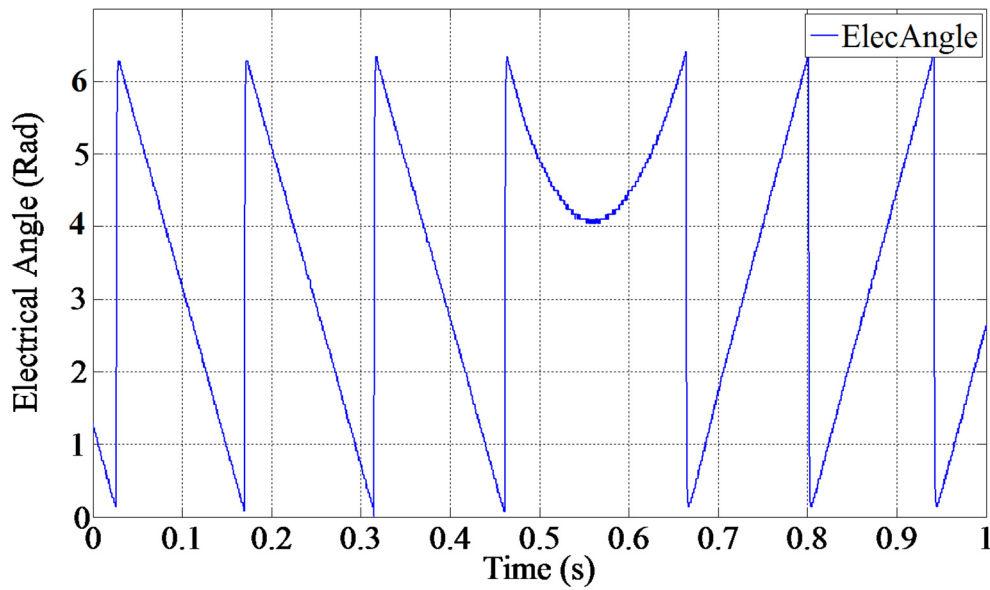


Figure 5-39 electrical anngle during speed reversal at  $300 \text{ min}^{-1}$

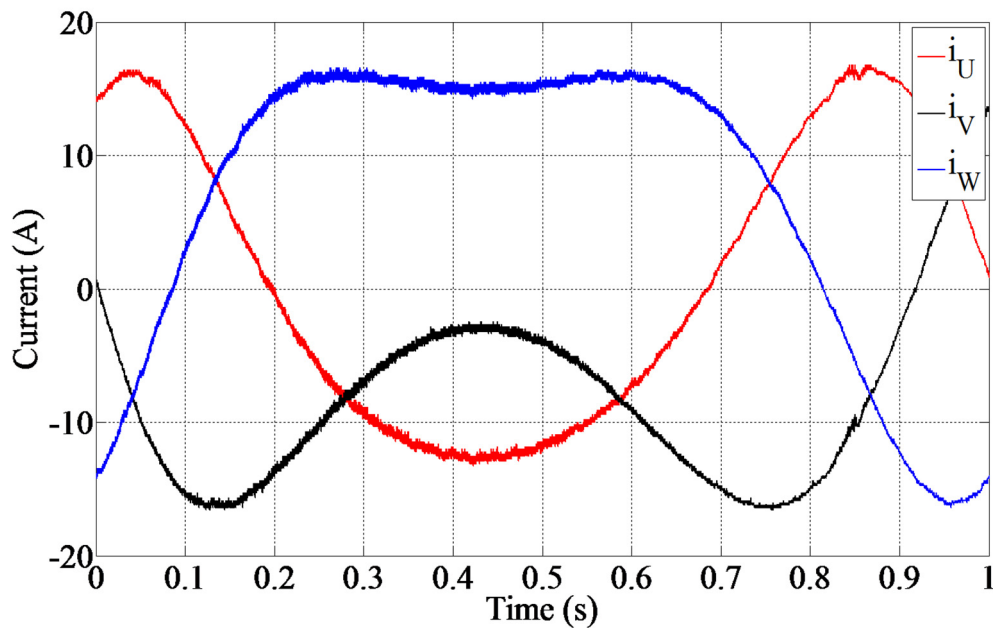


Figure 5-40 Phase currents during speed reversal at  $300 \text{ min}^{-1}$

#### 5.2.4.2.2 Current control

The behavior of the current control in sensorless operation was examined as well. Figure 5-41 shows the step response of the  $i_q$ -controller. As can be seen, the behavior is satisfactory although slower than that in operation with an encoder. The measurement was

carried out for a small step of  $50 \text{ min}^{-1}$  in the reference speed with the drive rotating at  $250 \text{ min}^{-1}$ .

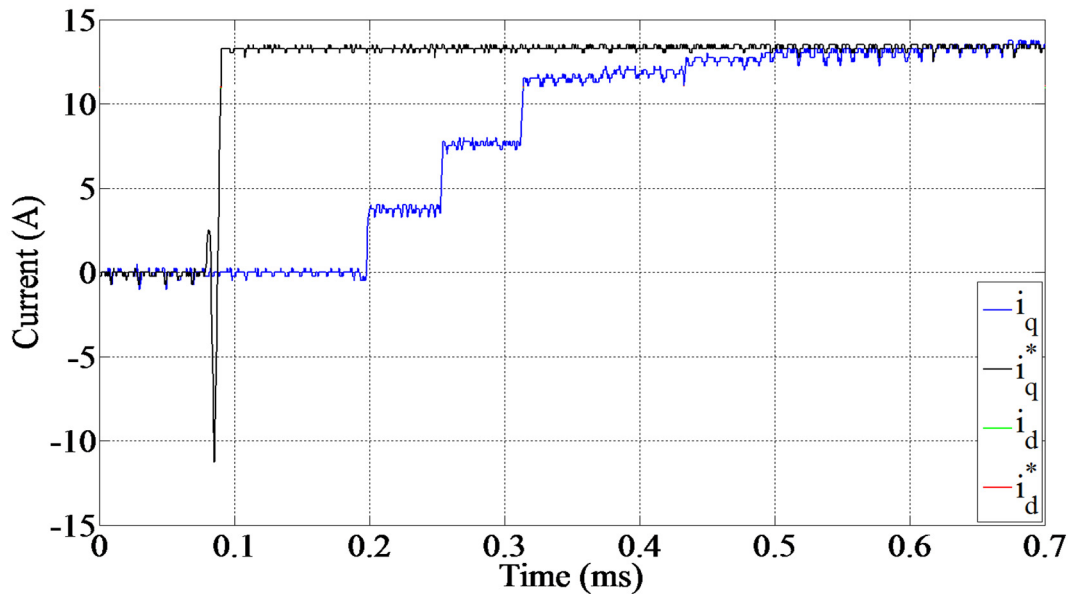


Figure 5-41 Step response of the  $i_q$  controller for a step on the speed reference from  $n^* = 250 \text{ min}^{-1}$  to  $n^* = 300 \text{ min}^{-1}$

#### 5.2.4.2.3 Disturbance rejection

Further measurements are related to the disturbance rejection under MRAS sensorless control and by applying different models for the estimation of the orientation angle. Figure 5-42 shows the response to a step load when the induction machine is speed controlled. It shows the dynamic behavior of the measured speed and of the identified speed of the MRAS when the standard voltage model is used as a reference. At the instant of switching the load level from zero to  $19 \text{ Nm} = 90 \% M_N$ , there is a drop in the speed and after the settling time it reaches the initial value. As it can be clearly seen, the red curve of the identified is a good estimate of the measured (the black curve) during the transient.

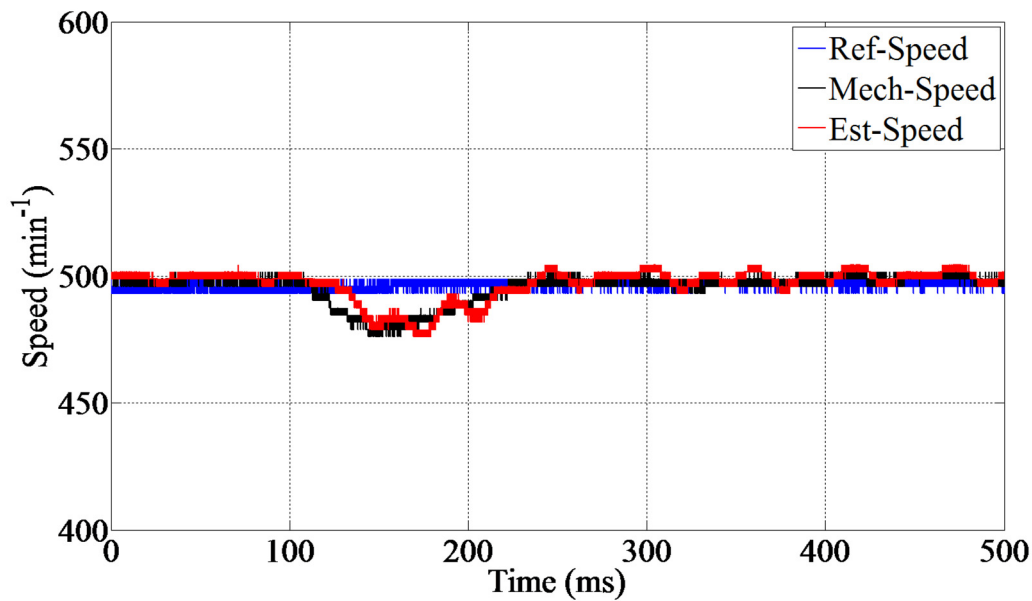


Figure 5-42 Disturbance rejection of a step on the load at  $n^*=500 \text{ min}^{-1}$  for the case of MRAS when using the standard voltage model: Reference (blue), actual speed (black) and estimated speed in red

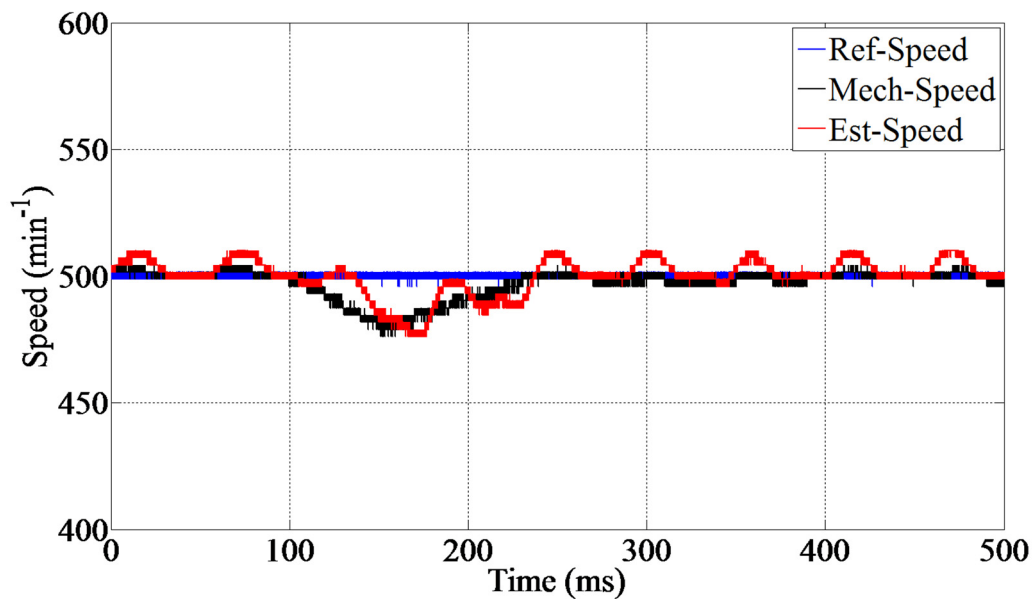


Figure 5-43 Disturbance rejection of a step on the load at  $n^*=500 \text{ min}^{-1}$  for the case of MRAS when using the enhanced voltage model: Reference (blue), actual speed (black) and estimated speed in red

As in the other measurements, an enhanced model was also used in which the sinusoidal voltages obtained after the LP filter were used in the voltage model. This enhanced model was used as a reference model for the speed estimation in the MRAS. Figure 5-43 shows the response of the measured speed and identified speed of the MRAS in addition



to the reference speed for the case of a step load. Also here the behavior is acceptable although the estimated speed contains an undesired oscillation.

The behavior of the MRAS was also examined for the case that the NFO (Natural Field Orientation model) is used as reference. Firstly, the standard natural filed orientation model that uses the reconstructed terminal voltages was used as a reference model. Figure 5-44 show the reference speed, the estimated speed and the measured speed for the case of a step from zero to  $19 \text{ Nm} = 90 \% M_N$ , on the load.

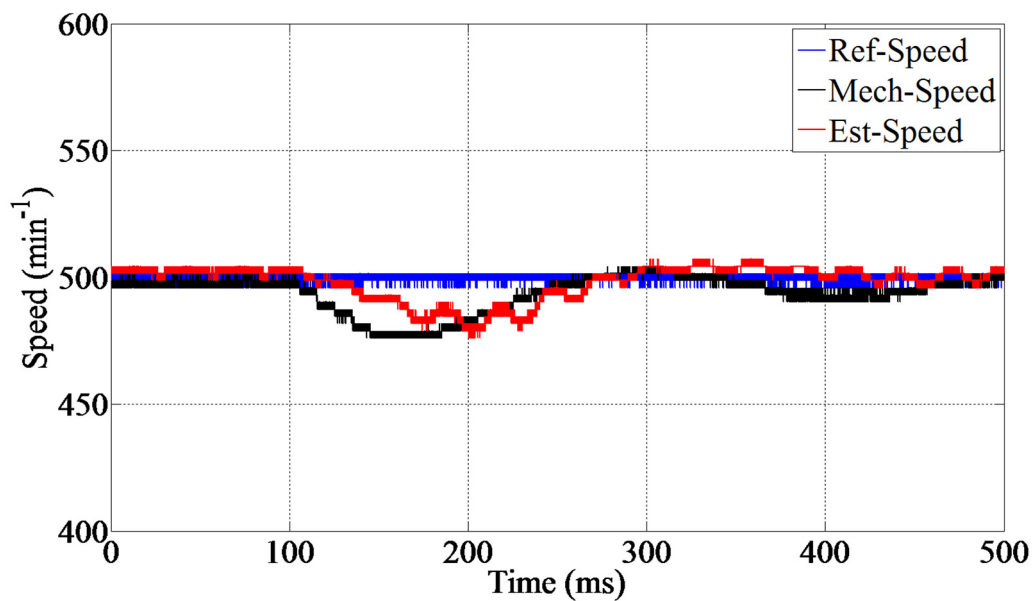


Figure 5-44 Disturbance rejection of a step on the load at  $n^*=500 \text{ min}^{-1}$  for the case of MRAS when using the NFO as a reference model: Reference (blue), actual speed (black) and estimated speed in red

Secondly, to enhance the encoder-less operation, the measured stator voltages of the machine (after the LP filter) were used in order to improve the NFO. The dynamic performance for a disturbance rejection in speed control mode is presented in Figure 5-45, it shows the reference speed, the estimated speed and the measured speed for the case of a step from zero to  $19 \text{ Nm} = 90 \% M_N$  on the load.

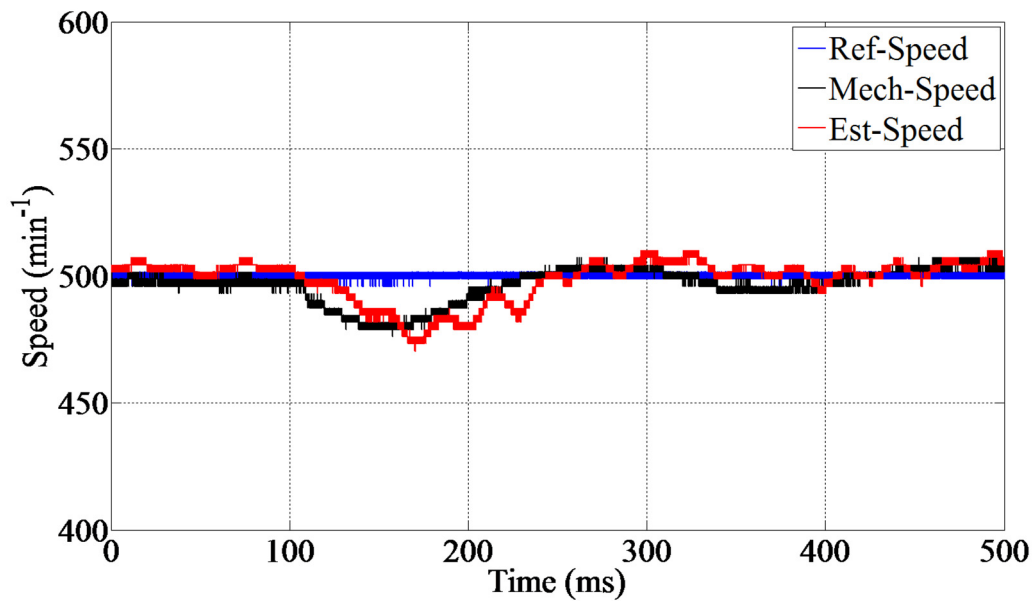


Figure 5-45 Disturbance rejection of a step on the load at  $n^*=500 \text{ min}^{-1}$  for the case of MRAS when using the NFO as a reference model: Reference (blue), actual speed (black) and estimated speed in red

#### 5.2.4.2.4 Elevator profile

After testing the steady state and the dynamic performance of the model reference adaptive system while using different models for a further series of experiments, a speed profile was defined as depicted in Figure 5-46. It consists of two ramps for acceleration up to  $300 \text{ min}^{-1}$  and down to zero. The profile exhibits two periods of constant velocity: zero and  $300 \text{ min}^{-1}$ . This kind of speed profile represents the operation of a lift. Especially important is the zero velocity period, which is the most demanding in sensorless control.

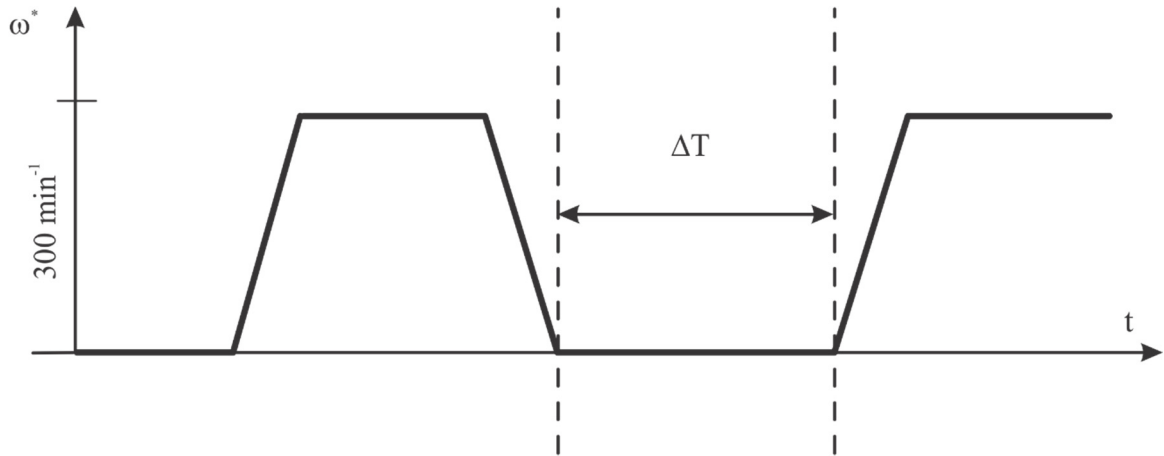


Figure 5-46 Reference speed profile for testing the encoder-less MRAS scheme in the different variants

Again the experiments were carried out by using the different reference models like in the former case and also by implementing reference models with and without measurement of the terminal voltages. In all figures the reference speed corresponds to the blue trace, while the red and the black traces correspond to the estimated and to the actual speed (measured with the encoder) respectively.

In all experimental tests, the same operation conditions were applied besides the profile was repeated 20 times to make sure that the MRAS is stable and working well, while the maximum speed is  $300 \text{ min}^{-1}$ , and  $M_L \approx 90\% M_N$  the maximum load was applied, i.e.  $i_q = 12\text{A}$ .

In Figure 5-47 the response to the lift profile with the standard voltage model, i.e. with reconstruction of the terminal voltages, is shown. It can be seen that the acceleration after the operation at zero speed is not satisfactory even if a rather small time of  $\Delta t = 500 \text{ ms}$  is set in the speed profile. If the time is further increased, the control becomes unstable. The same measurement, but using the EUM and illustrated in Figure 5-48, shows that period of zero speed can be increased up to  $\Delta t = 1.2 \text{ s}$ . Thus, the system is enhanced.

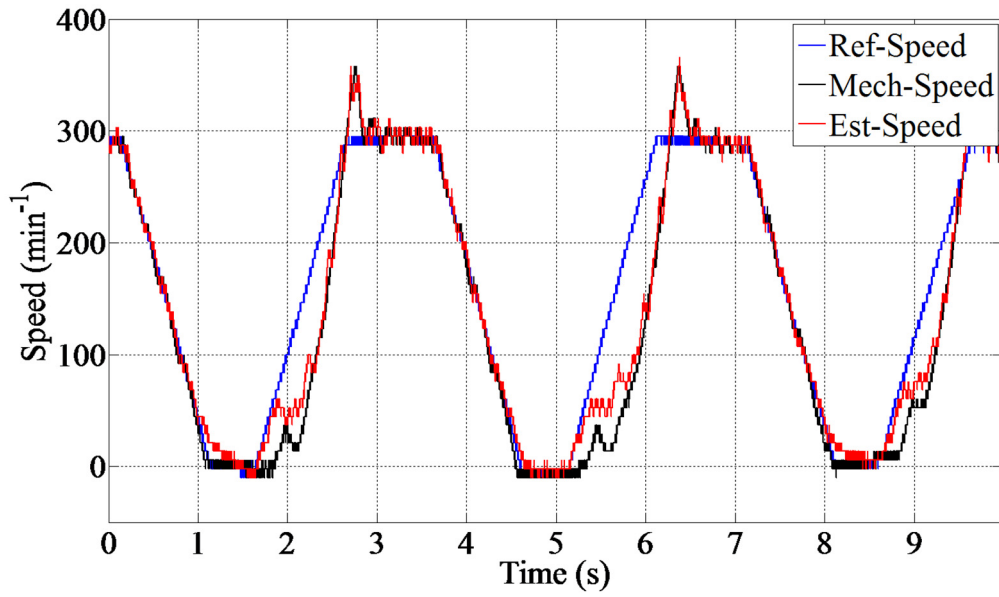


Figure 5-47 Encoder-less MRAS speed response when using the SU-Model as a reference and when applying a  $M_L \approx 90\% M_N$ , ( $\Delta t = 0.5$  s)

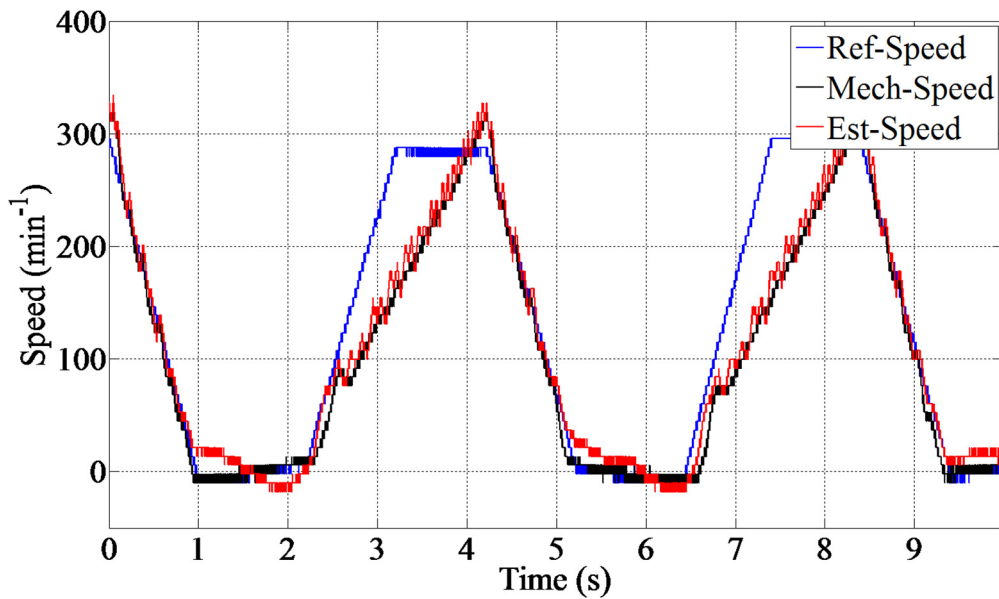


Figure 5-48 Encoder-less MRAS speed response when using the EU-Model as a reference and when applying a  $M_L \approx 90\% M_N$ , ( $\Delta t = 0.5$  s)

Similar experiments were performed by using the NFO as reference model. As shown in Figure 5-49, the behavior is also not satisfactory and only a maximum  $\Delta t = 50$  ms could be achieved. If the  $\Delta t$  is increased, the drives cannot follow the reference anymore as shown in Figure 5-50.

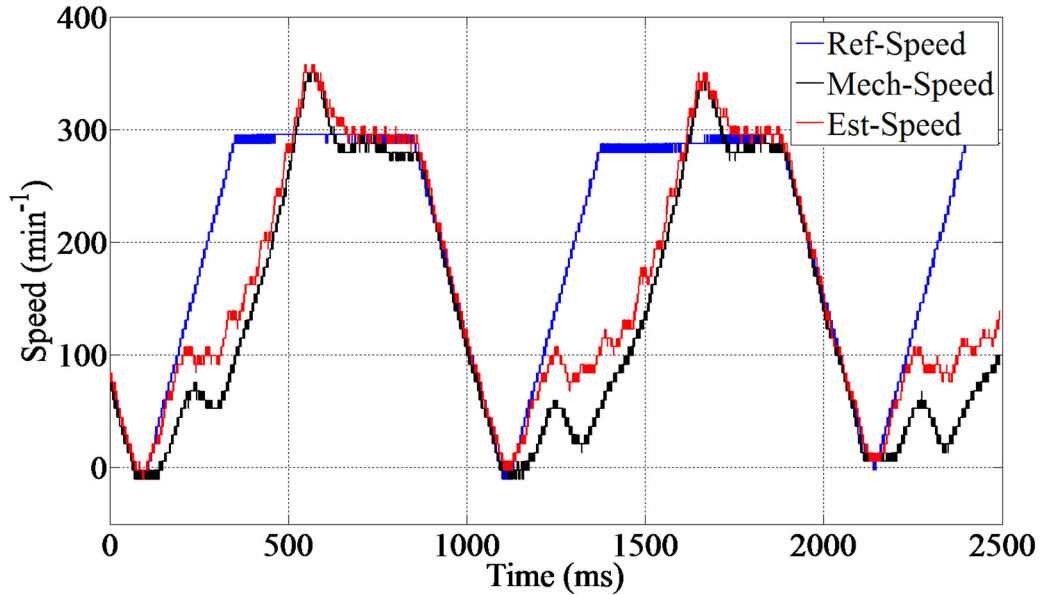


Figure 5-49 Encoder-less MRAS speed response when using the NFO-Model as a reference and when applying a  $M_L \approx 90\% M_N$ , ( $\Delta t = 50$  ms)

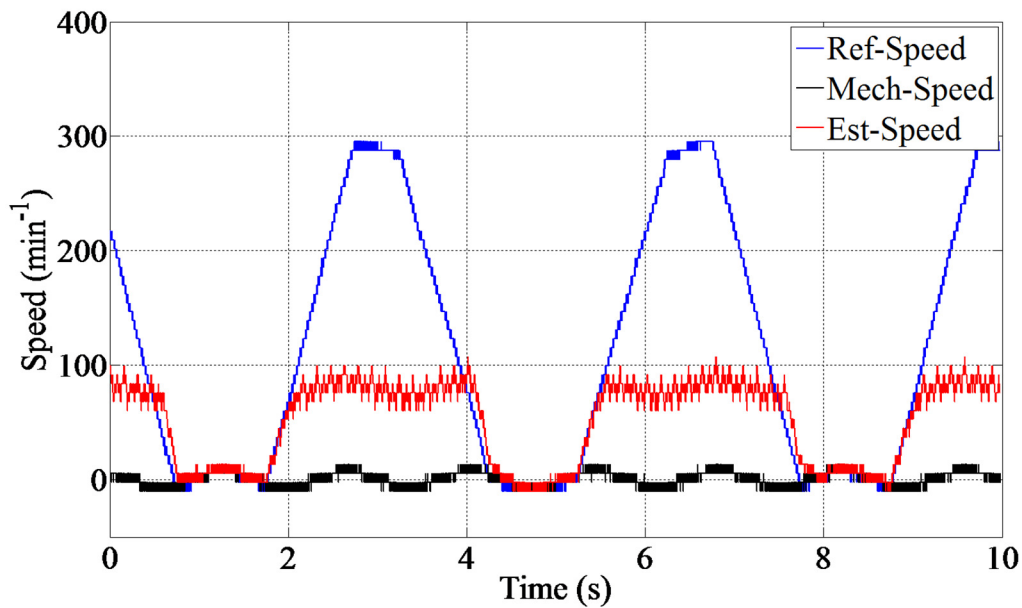


Figure 5-50 Encoder-less MRAS speed response when using the NFO-Model as a reference and when applying a  $M_L \approx 90\% M_N$ , ( $\Delta t > 50$ ms)

Contrary to the depiction in Figure 5-51, by using the MRAS with NFO as a reference model, and by enhancing it with the measurement of the terminal voltages to an ENFO which delivers a satisfactory behavior, the drive will follow the reference value of the speed even in the long zero periods for more than 10 s. As shown in Figure 5-52, in the zero phase of the speed profile the machine rotates with a very low speed corresponding to the slip that is necessary to produce the desired torque and the space phasor of the stator currents is at a standstill like in the case of a dc-brake, as depicted in Figure 5-53. It is remarkable that the drive can be operated without any problem or any loss of stability for long phases  $\Delta t$  of zero reference speed. The drive can be braked to the lowest speed and accelerated according to the profile without any kind of limitation.

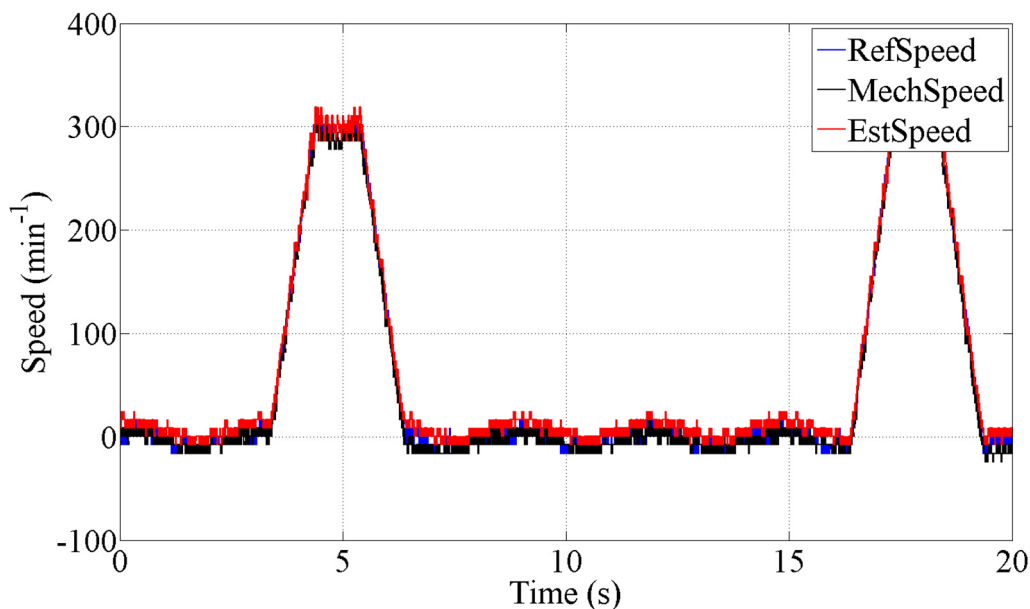


Figure 5-51 Encoder-less MRAS speed response when using the NFO-Model as a reference and when applying a  $M_L \approx 90\% M_N$ , ( $\Delta t = 10$  s)

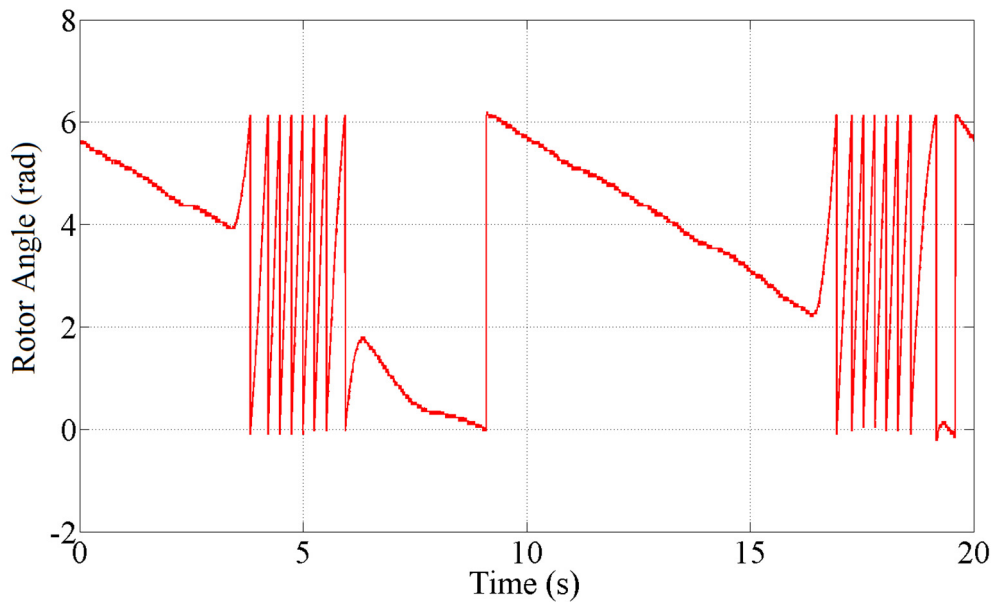


Figure 5-52 Mechanical angle for the encoder-less MRAS operation when using the ENFO-Model as a reference and when applying a  $M_L \approx 90\% M_N$ , ( $\Delta t = 10$  s)

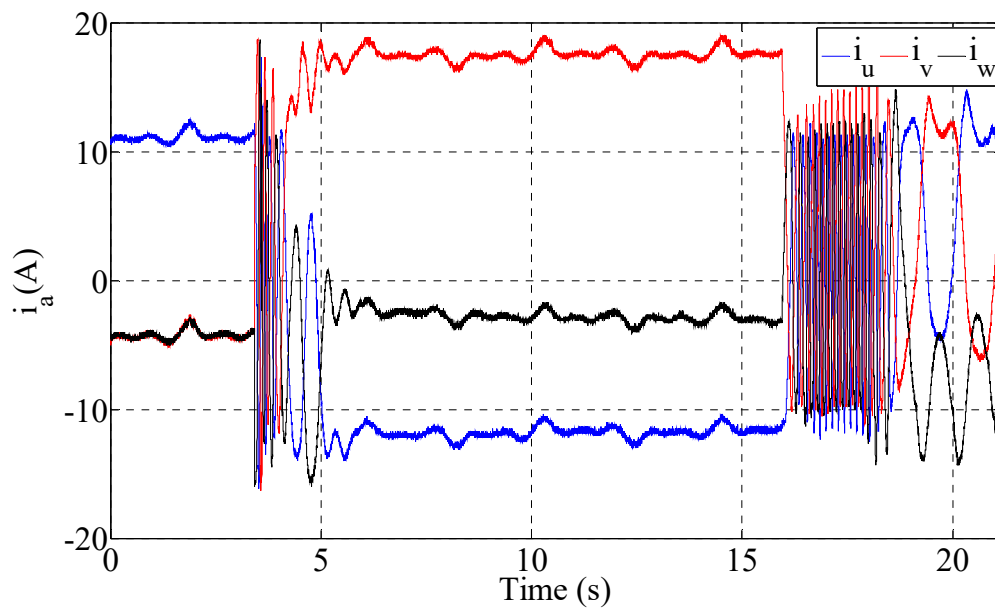


Figure 5-53 Stator currents in case of the encoder-less MRAS operation when using the ENFO-Model as a reference and when applying a  $M_L \approx 90\% M_N$ , ( $\Delta t = 10$  s)

The same experiment can be carried out by using the MRAS with ENFO as reference model and no load i.e.  $M_L = 0$ . In that case when the reference speed is zero, the machine is at a standstill and the shaft does not rotate anymore. Figure 5-54 and Figure

5-55 illustrate this behavior. Further measurements with larger periods  $\Delta t$  up into the range of minutes deliver similar results as depicted in Figure 5-56 and Figure 5-57.

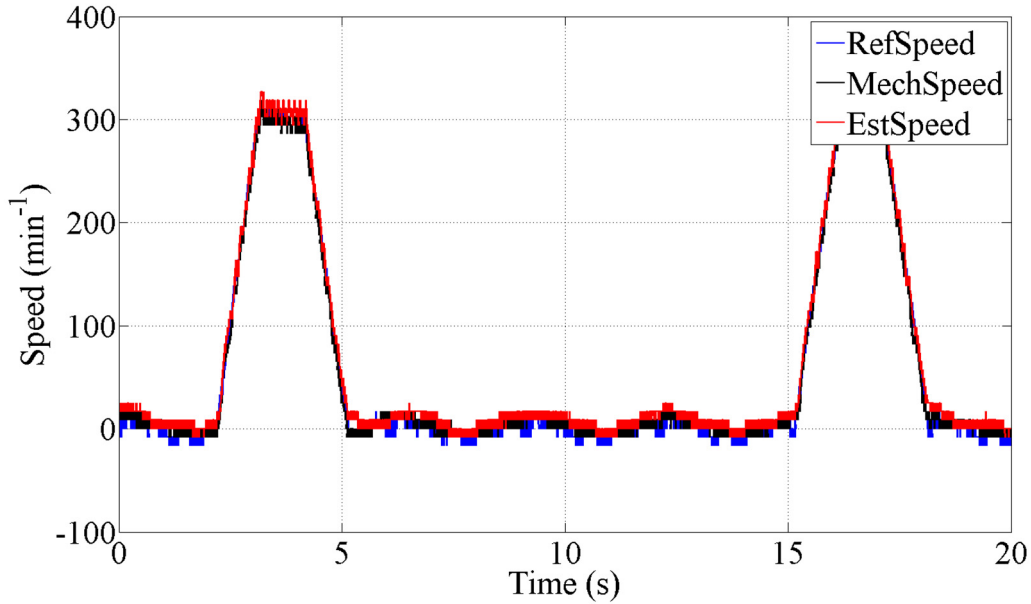


Figure 5-54 Encoder-less MRAS speed response when using the NFO-Model as a reference and when applying a  $M_L = 0$ , ( $\Delta t = 10$  s)

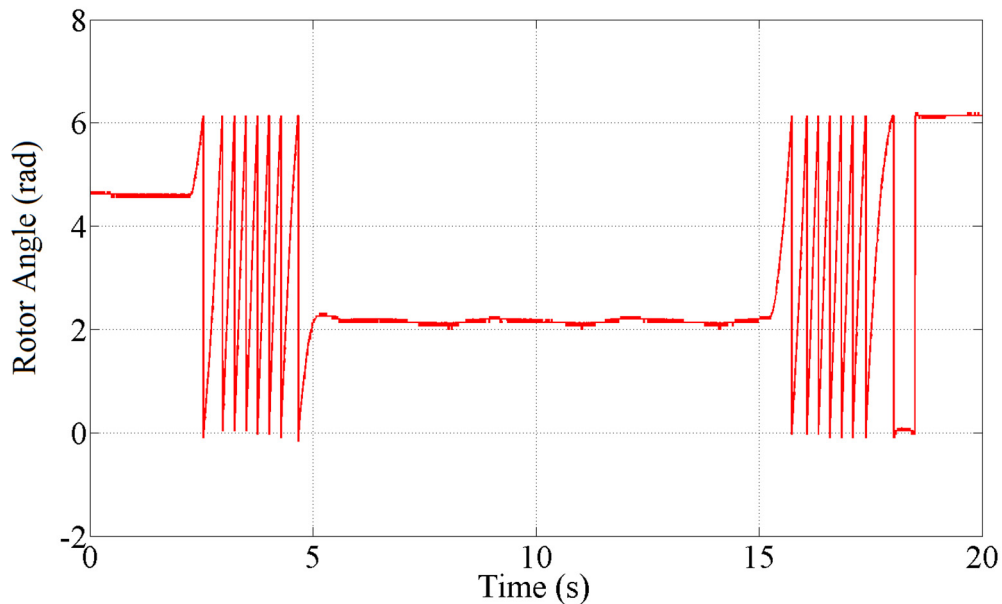


Figure 5-55 Mechanical angle for the encoder-less MRAS operation when using the ENFO-Model as a reference and when applying a  $M_L = 0$ , ( $\Delta t = 10$  s)



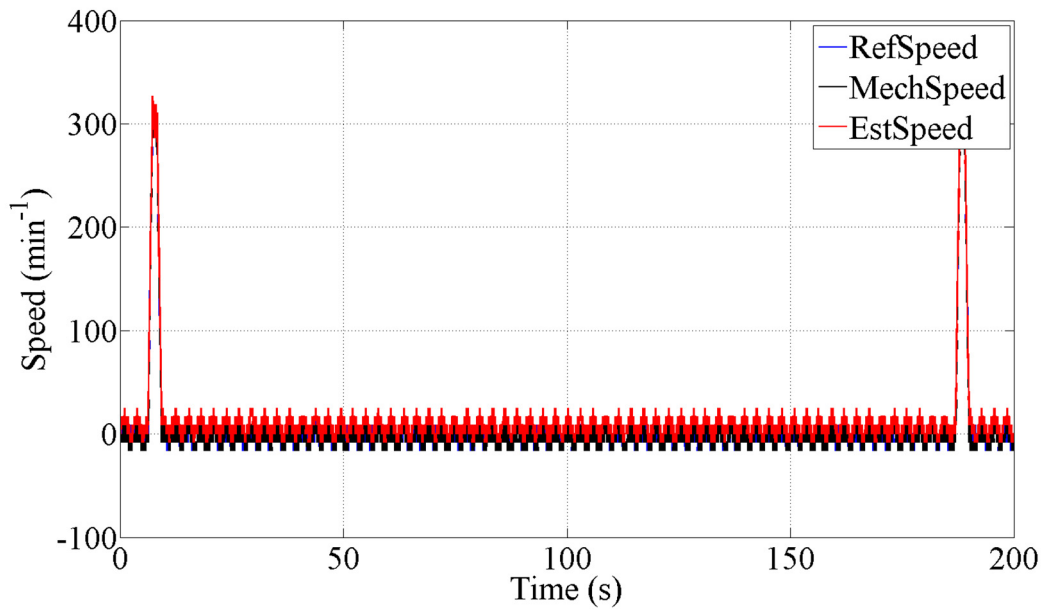


Figure 5-56 Encoder-less MRAS speed response when using the NFO-Model as a reference and when applying a  $M_L = 0$ , ( $\Delta t = 3$  min)

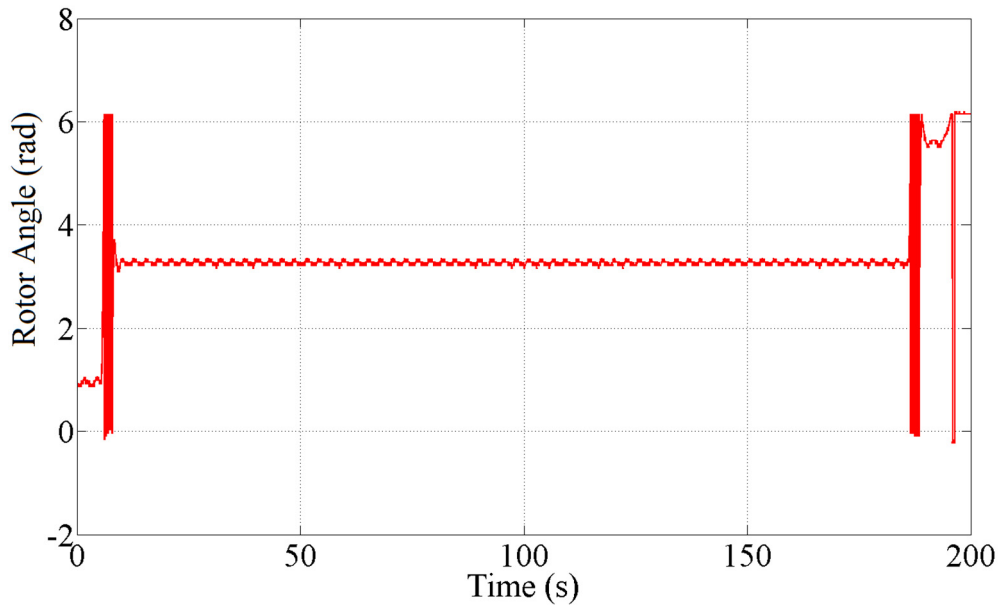


Figure 5-57 Mechanical angle for the encoder-less MRAS operation when using the ENFO-Model as a reference and when applying a  $M_L = 0$ , ( $\Delta t = 3$  min)

Based on these measurements it can be concluded that the model reference adaptive control with the enhanced natural field orientation scheme as reference model exhibits a very good behavior down to very low speed.

### 5.3 Summary of the chapter

This chapter presents the experimental results for the sensorless control techniques of the induction machine discussed in the previous chapters. It is divided into three sections: the first section is dedicated to the detailed description of the laboratory setup that consist of a three-phase, two-level conventional voltage source inverter (VSI), equipped with silicon carbide (SiC)-switches and an output LC filter featuring almost sinusoidal output voltages. The experimental results of the control schemes proposed in this work: the enhanced field oriented and sensorless control scheme using both voltage model and natural field orientation (NFO) schemes and the voltages measured on the terminals of the machine are presented in the second section of this chapter. Finally, the experimental results of the model reference adaptive system (MRAS) also proposed in this work and that uses the standard voltage model (SUM), the enhanced voltage model (EUM), the natural field orientation (NFO) and the enhanced natural field orientation (ENFO) as a reference model were included in the third section.

In a further step, this chapter documents a speed profile that consists of two ramps for acceleration up to  $300 \text{ min}^{-1}$  and down to zero. The profile exhibits two periods of constant velocity: zero and  $300 \text{ min}^{-1}$ . This kind of speed profile represents the operation of a lift. Especially important is the zero velocity period, which is the most demanding in sensorless control.

## 6 Conclusions

This work examines a SiC inverter with an output filter for feeding an induction machine. The aim of the work is to obtain almost sinusoidal voltages on the terminals of the machine with the purpose of the enhancement of the voltage model that is used for the estimation of the rotor flux space phasor in field oriented control schemes. In this way the measured terminal voltages can be used instead of the reconstructed ones as is common in industrial implementations. In addition the proposal presented in the literature many years ago, the so-called "natural field orientation" NFO, is combined with a model reference adaptive system (MRAS) control scheme and implemented by using the measured terminal voltages.

The numerous experimental results of measurements carried out on a laboratory setup, comparing the different control schemes for the case of an implementation with reconstructed and with measured stator voltages, show that the utilization of the measured voltages lead to a significant enhancement of the steady state and dynamic performance of the induction machine drive, especially in the very low speed range.

In addition, based on the comparative measurements it can be concluded that a MRAS together with the NFO (and with the utilization of the measured voltages instead of the reconstructed ones) exhibits very good behavior in the lowest speed range and contributes in this way to the enhancement of sensorless control schemes for the asynchronous machine.

## 7 Appendix

### Parameters of the laboratory drive system

Table 7-1 Parameters of the laboratory drive system

Driven Induction machine (IM) parameters	
Manufacturer	ABB
Nominal Power	7.5 KW
Nominal Voltage	400 V
Nominal Current	17 A
Nominal Speed	1800-9000 min <sup>-1</sup>
Nominal Frequency	60 Hz
Pole pairs	2
Winding resistance $R_1$	3.004 $\Omega$
Winding resistance	1.566 $\Omega$
Winding inductance $L_{1\sigma}$	4.438 mH
Winding inductance $L_{2\sigma}'$	4.598 mH
Mutual inductance $L_{1h}$	146.4 mH
$\cos(\varphi)$	0.82
Moment of inertia	0.0195 kgm <sup>2</sup>
Mechanical coupling parameters	
Moment of inertia	0.0064 kgm <sup>2</sup>
Load Induction machine (IM) parameters	
Manufacturer	Siemens
Nominal Power	21 kW
Moment of inertia	0.109 kgm <sup>2</sup>

## 8 References

- [1] H. Al-Badrani, S. Feuersaenger, and M. Pacas, "VSI with Sinusoidal Voltages for an Enhanced Sensorless Control of the Induction Machine," in *PCIM Europe 2018; International Exhibition and Conference for Power Electronics, Intelligent Motion, Renewable Energy and Energy Management*, 2018, pp. 1–7.
- [2] C. Sintamarean, F. Blaabjerg, H. Wang, and Y. Yang, "Real field mission profile oriented design of a SiC-based PV-inverter application," in *2013 IEEE Energy Conversion Congress and Exposition*, 2013, pp. 940–947.
- [3] S. Wall, R. h Ruan, C. g Wang, and J. r Xie, "Evaluation of three-phase solar inverters using SiC devices," in *2016 18th European Conference on Power Electronics and Applications (EPE'16 ECCE Europe)*, 2016, pp. 1–10.
- [4] J. Holtz and J. Quan, "Drift- and parameter-compensated flux estimator for persistent zero-stator-frequency operation of sensorless-controlled induction motors," *IEEE Trans. Ind. Appl.*, vol. 39, no. 4, pp. 1052–1060, Jul. 2003.
- [5] M. Depenbrock and C. Evers, "Model-based speed identification for induction Machines in the whole operating range," *IEEE Trans. Ind. Electron.*, vol. 53, no. 1, pp. 31–40, Feb. 2005.
- [6] B. K. Bose, *Power Electronics and Motor Drives : Advances and Trends*. Amsterdam: Academic. p. 22., 2006.
- [7] B. Drury, *The Control Techniques Drives and Controls Handbook (2nd ed.)*. Stevenage, Herts, UK: Institution of Engineering and Technology. p. xxx., 2009.
- [8] K. Hasse, "Zum Dynamischen Verhalten der Asynchronmaschine bei Betrieb mit variabler Ständerspannung," *ETZ- Band 89*, pp. 77–81, 1968.
- [9] F. Blaschke, "Das Prinzip der Feldorientierung, Grundlage für die Transvektor-Regelung von Drehfeldmaschinen," *Siemens-Zeitschrift 45*, pp. 757–760, 1971.
- [10] D. W. Novotny and T. A. Lipo, *Vector Control and Dynamics of AC Drives*. Oxford University Press, UK, 1999.
- [11] P. Vas, *Sensorless Vector and Direct Torque Control*. Oxford University Press, 1998.
- [12] C. Schauder, "Adaptive speed identification for vector control of induction motors without rotational transducers," *IEEE Trans. Ind. Appl.*, vol. 28, no. 5, pp. 1054–1061, Sep. 1992.
- [13] J. Holtz, "Sensorless Control of Induction Machines #8212;With or Without Signal Injection?," *IEEE Trans. Ind. Electron.*, vol. 53, no. 1, pp. 7–30, Feb. 2006.

- [14] T. Szalai, G. Berger, and J. Petzoldt, "Stabilizing Sensorless Control Down to Zero Speed by Using the High-Frequency Current Amplitude," *IEEE Trans. Power Electron.*, vol. 29, no. 7, pp. 3646–3656, Jul. 2014.
- [15] M. A. Vogelsberger, S. Grubic, T. G. Habetler, and T. M. Wolbank, "Using PWM-Induced Transient Excitation and Advanced Signal Processing for Zero-Speed Sensorless Control of AC Machines," *IEEE Trans. Ind. Electron.*, vol. 57, no. 1, pp. 365–374, Jan. 2010.
- [16] M. Schroedl, "Sensorless control of AC machines at low speed and standstill based on the 'INFORM' method," in *IAS '96. Conference Record of the 1996 IEEE Industry Applications Conference Thirty-First IAS Annual Meeting, 1996*, vol. 1, pp. 270–277 vol.1.
- [17] T. Orłowska-Kowalska and M. Dybkowski, "Stator-Current-Based MRAS Estimator for a Wide Range Speed-Sensorless Induction-Motor Drive," *IEEE Trans. Ind. Electron.*, vol. 57, no. 4, pp. 1296–1308, Apr. 2010.
- [18] Y. B. Zbede, S. M. Gadoue, and D. J. Atkinson, "Model Predictive MRAS Estimator for Sensorless Induction Motor Drives," *IEEE Trans. Ind. Electron.*, vol. 63, no. 6, pp. 3511–3521, Jun. 2016.
- [19] H. Kubota, K. Matsuse, and T. Nakano, "New adaptive flux observer of induction motor for wide speed range motor drives," in *[Proceedings] IECON '90: 16th Annual Conference of IEEE Industrial Electronics Society, 1990*, pp. 921–926 vol.2.
- [20] L. Harnefors and M. Hinkkanen, "Complete Stability of Reduced-Order and Full-Order Observers for Sensorless IM Drives," *IEEE Trans. Ind. Electron.*, vol. 55, no. 3, pp. 1319–1329, Mar. 2008.
- [21] K. Wang, W. Yao, K. Lee, and Z. Lu, "Regenerating Mode Stability Improvements for Combined Voltage and Current Mode Flux Observer in Speed Sensorless Induction Machine Control," *IEEE Trans. Ind. Appl.*, vol. 50, no. 4, pp. 2564–2573, Jul. 2014.
- [22] M. Depenbrock and C. Evers, "Model-based speed identification for induction Machines in the whole operating range," *IEEE Trans. Ind. Electron.*, vol. 53, no. 1, pp. 31–40, Feb. 2006.
- [23] S. Tamai, H. Sugimoto, and Y. Masao, "Speed sensorless vector control of IM with model reference adaptive system," *Conf Rec IEEEIAS Annu.*, pp. 189–195, 1987.
- [24] S. Beineke, J. Schirmer, J. Lutz, H. Wertz, A. Bähr, and J. Kiel, "Implementation and applications of sensorless control for synchronous machines in industrial inverters," in *2010 First Symposium on Sensorless Control for Electrical Drives, 2010*, pp. 64–71.

- [25] M. Pacas, "Sensorless Drives in Industrial Applications," *IEEE Ind. Electron. Mag.*, vol. 5, no. 2, pp. 16–23, Jun. 2011.
- [26] A. R. Munoz and T. A. Lipo, "Complex vector model of the squirrel-cage induction machine including instantaneous rotor bar currents," *IEEE Trans. Ind. Appl.*, vol. 35, no. 6, pp. 1332–1340, Nov. 1999.
- [27] W. Leonhard, *Control of Electrical Drives*. © Springer-Verlag Berlin Heidelberg 1996, 1996.
- [28] Paul, O. Wasynczuk, S. Sudhoff, and S. Pekarek, *Analysis of Electric Machinery And Drive Systems*. John Wiley & Sons, Inc., Hoboken, New Jersey., 2013.
- [29] F. Blaschke and T. Salzmann, "rotating field machine drive," *United State Pat. US 4388577 A*, Jul. 1981.
- [30] M. P. Kazmierkowski, R. Krishnan, and F. Blaabjerg, *Control in Power Electronics Selected Problems. Supply Chain Design and Management*, 2002, M. Govil and J. M. Proth, 2002.
- [31] M. Hinkkanen and J. Luomi, "Modified integrator for voltage model flux estimation of induction motors," *IEEE Trans. Ind. Electron.*, vol. 50, no. 4, pp. 818–820, Aug. 2003.
- [32] K. Zhao and X. You, "Speed estimation of induction motor using modified voltage model flux estimation," in *2009 IEEE 6th International Power Electronics and Motion Control Conference*, 2009, pp. 1979–1982.
- [33] Z. Xing, Q. Wenlong, and L. Haifeng, "A New Integrator for Voltage Model Flux Estimation in a Digital DTC System," in *TENCON 2006 - 2006 IEEE Region 10 Conference*, 2006, pp. 1–4.
- [34] K. Zhao, F. Lin, and X. You, "A modified voltage model flux estimation of induction motors," in *2008 International Conference on Electrical Machines and Systems*, 2008, pp. 94–97.
- [35] P. Brandstetter and M. Kuchar, "Rotor flux estimation using voltage model of induction motor," in *2015 16th International Scientific Conference on Electric Power Engineering (EPE)*, 2015, pp. 246–250.
- [36] J. W. Finch and D. Giaouris, "Controlled AC Electrical Drives," *IEEE Trans. Ind. Electron.*, vol. 55, no. 2, pp. 481–491, Feb. 2008.
- [37] E. Serna and M. Pacas, "Detection of rotor asymmetries of induction machines in an encoderless control scheme," in *2009 IEEE International Symposium on Industrial Electronics*, 2009, pp. 523–528.

- [38] E. Serna and J. M. Pacas, "Detection of Rotor Faults in Field Oriented Controlled Induction Machines," in Conference Record of the 2006 IEEE Industry Applications Conference Forty-First IAS Annual Meeting, 2006, vol. 5, pp. 2326–2332.
- [39] H. Rehman, "Design of voltage model flux observer," IEE Proc. - Electr. Power Appl., vol. 151, no. 2, pp. 129–134, Mar. 2004.
- [40] E. T. Serna Calvo, "Diagnostics of Rotor Asymmetries in Inverter-Fed, Variable Speed Induction Machines," PhD Diss. Univ. Siegen, 2009.
- [41] "Saul Dufoo Ochoa, 'Diagnostics of rotor asymmetries in inverter fed induction machines,' Ph.D. Thesis, University of Siegen, Germany, 2012."
- [42] H. A. Toliyat and T. A. Lipo, "Transient analysis of cage induction machines under stator, rotor bar and end ring faults," IEEE Trans. Energy Convers., vol. 10, no. 2, pp. 241–247, Jun. 1995.
- [43] M. Ahmad, High Performance AC Drives. Modeling Analysis and Control. London, UK, 2010.
- [44] M. Popescu, "Induction Motor Modelling for Vector Control Purposes," Hels. Univ. Technol., 2000.
- [45] E. Serna and M. Pacas, "Diagnosis of rotor asymmetries in induction machines with different field oriented schemes," in 2008 34th Annual Conference of IEEE Industrial Electronics, 2008, pp. 1143–1148.
- [46] K. D. Hurst, T. G. Habetler, G. Griva, and F. Profumo, "Zero-speed tachless IM torque control: simply a matter of stator voltage integration," IEEE Trans. Ind. Appl., vol. 34, no. 4, pp. 790–795, Jul. 1998.
- [47] J. Hu and B. Wu, "New integration algorithms for estimating motor flux over a wide speed range," in PESC97. Record 28th Annual IEEE Power Electronics Specialists Conference. Formerly Power Conditioning Specialists Conference 1970-71. Power Processing and Electronic Specialists Conference 1972, 1997, vol. 2, pp. 1075–1081 vol.2.
- [48] T. Ohtani, N. Takada, and K. Tanaka, "Vector control of induction motor without shaft encoder," in Conference Record of the IEEE Industry Applications Society Annual Meeting, 1989, pp. 500–507 vol.1.
- [49] J. Holtz, "Sensorless control of induction motor drives," Proc. IEEE, vol. 90, no. 8, pp. 1359–1394, Aug. 2002.



- [50] J. Holtz and J. Quan, "Sensorless vector control of induction motors at very low speed using a nonlinear inverter model and parameter identification," in Conference Record of the 2001 IEEE Industry Applications Conference. 36th IAS Annual Meeting (Cat. No.01CH37248), 2001, vol. 4, pp. 2614–2621 vol.4.
- [51] R. Jönsson, "Method and apparatus for controlling an AC motor," U. S. Pat. 4458193, Jul. 1984.
- [52] R. Jönsson, "Method and apparatus for controlling an ac induction motor by indirect measurement of the air-gap voltage," U. S. Pat. 5294876, Mar. 1994.
- [53] S. Peresada, A. Tilli, S. Kovbasa, M. Montanari, and F. Ronchi, "Simple sensorless vector control of induction motors with natural field orientation," in The 27th Annual Conference of the IEEE Industrial Electronics Society, 2001. IECON '01, 2001, vol. 1, pp. 641–646 vol.1.
- [54] R. E. Betz and G. Mirzaeva, "Frame Alignment Stability Issues in Natural Field Orientation," IEEE Trans. Ind. Appl., vol. 44, no. 2, pp. 575–593, Mar. 2008.
- [55] G. Mirzaeva and A. Rojas, "Advanced Control Strategies for Stability Improvement of Natural Field Orientation," in 2008 IEEE Industry Applications Society Annual Meeting, 2008, pp. 1–8.
- [56] G. Mirzaeva and R. E. Betz, "Slow speed performance of an NFO-controlled induction machine," in 2007 Australasian Universities Power Engineering Conference, 2007, pp. 1–6.
- [57] P. Kadaník, "NFO Speed Control of Induction Motor without Shaft Encoder," *Komunkáce Communcion*399.
- [58] G. Mirzaeva and R. E. Betz, "Natural Field Orientation Concept: a Tutorial," in 2007 IEEE International Electric Machines Drives Conference, 2007, vol. 2, pp. 1276–1281.
- [59] G. Mirzaeva and R. E. Betz, "An Improved Natural Field Orientation Control of a Current Fed Induction Machine," in 2007 IEEE International Electric Machines Drives Conference, 2007, vol. 1, pp. 424–429.
- [60] "R. Jönsson and W. Leonhard, 'Control of an induction motor without a mechanical sensor, based on the principle of natural field orientation (NFO),' in International Power Electronics Conference, IPEC'95, April 1995, pp. 1–6."
- [61] G. Mirzaeva and R. E. Betz, "Parameter Sensitivity Issues in Natural Field Orientation," in 2007 IEEE Industry Applications Annual Meeting, 2007, pp. 2050–2057.

- [62] R. Jönsson, O. Glenberg, H. Hemark, and R. Johansson, “Natural Field Orientation (NFO) for Control of the AC Induction Motor,” EPE - Toulouse, 2003.
- [63] B. K. Bose, *Modern Power Electronics and AC Drives*, 1st Edition. Prentice Hall PTR, 2002.
- [64] R. Kumar, S. Das, P. Syam, and A. K. Chattopadhyay, “Review on model reference adaptive system for sensorless vector control of induction motor drives,” IET Electr. Power Appl., vol. 9, no. 7, pp. 496–511, 2015.
- [65] M. Rashed and A. F. Stronach, “A stable back-EMF MRAS-based sensorless low-speed induction motor drive insensitive to stator resistance variation,” IEE Proc. - Electr. Power Appl., vol. 151, no. 6, pp. 685–693, Nov. 2004.
- [66] M. N. Marwali and A. Keyhani, “A comparative study of rotor flux based MRAS and back EMF based MRAS speed estimators for speed sensorless vector control of induction machines,” in , Conference Record of the 1997 IEEE Industry Applications Conference, 1997. Thirty-Second IAS Annual Meeting, IAS '97, 1997, vol. 1, pp. 160–166 vol.1.
- [67] J. Kaukonen, “Salient Pole Synchronous Machine Modelling in an Industrial Direct Torque Controlled Drive Application.” Dissertation, Lappeenranta University of Technology, Lappeenranta, Finland, 1999.
- [68] M. Niemelä, “Position Sensorless Electrically Excited Synchronous Motor Drive for Industrial Use Based on Direct Flux Linkage and Torque Control.” Dissertation, Lappeenranta University of Technology, Lappeenranta, Finland, 1999.
- [69] S. M. Gadoue, D. Giaouris, and J. W. Finch, “MRAS Sensorless Vector Control of an Induction Motor Using New Sliding-Mode and Fuzzy-Logic Adaptation Mechanisms,” IEEE Trans. Energy Convers., vol. 25, no. 2, pp. 394–402, Jun. 2010.
- [70] R. Julius and M. John, “Economics of high efficiency SiC MOSFET based 3-ph motor drive,” PCIM Eur., May 2014.
- [71] J. Millán, P. Godignon, X. Perpiñà, A. Pérez-Tomás, and J. Rebollo, “A Survey of Wide Bandgap Power Semiconductor Devices,” IEEE Trans. Power Electron., vol. 29, no. 5, pp. 2155–2163, May 2014.
- [72] B. Ozpineci and L. M. Tolbert, *Comparison of Wide-Bandgap Semiconductors for Power Electronics Applications*. .
- [73] “D. Stephani, ‘Today’s and tomorrow’s industrial utilization of silicon carbide power devices,’ presented at the 10th Eur. Conf. Power Electron. Appl., Toulouse, France, 2003, Paper 1199.”

- [74] T. Funaki et al., "Power Conversion With SiC Devices at Extremely High Ambient Temperatures," *IEEE Trans. Power Electron.*, vol. 22, no. 4, pp. 1321–1329, Jul. 2007.
- [75] P. Ning, F. Wang, and K. D. T. Ngo, "High-Temperature SiC Power Module Electrical Evaluation Procedure," *IEEE Trans. Power Electron.*, vol. 26, no. 11, pp. 3079–3083, Nov. 2011.
- [76] R. Wang et al., "A High-Temperature SiC Three-Phase AC - DC Converter Design for #x003E; 100/spl deg/C Ambient Temperature," *IEEE Trans. Power Electron.*, vol. 28, no. 1, pp. 555–572, Jan. 2013.
- [77] R. J. Callanan et al., "Recent progress in SiC DMOSFETs and JBS diodes at Cree," in 2008 34th Annual Conference of IEEE Industrial Electronics, 2008, pp. 2885–2890.
- [78] J. Colmenares, D. P. Sadik, P. Hilber, and H. P. Nee, "Reliability Analysis of a High-Efficiency SiC Three-Phase Inverter," *IEEE J. Emerg. Sel. Top. Power Electron.*, vol. 4, no. 3, pp. 996–1006, Sep. 2016.
- [79] M. Lechler and B. Piepenbreier, "Regenerative SiC frequency converter with compact Z-source DC-link and sinusoidal output voltage," in Automation and Motion International Symposium on Power Electronics Power Electronics, Electrical Drives, 2012, pp. 1506–1511.
- [80] J. Rabkowski, T. Sak, R. Strzelecki, and M. Grabarek, "SiC-based T-type modules for multi-pulse inverter with coupled inductors," in 2017 11th IEEE International Conference on Compatibility, Power Electronics and Power Engineering (CPE-POWERENG), 2017, pp. 568–572.
- [81] H. Barth and W. Hofmann, "Decrease of SiC-BJT driver losses by one-step commutation," in 2014 International Power Electronics Conference (IPEC-Hiroshima 2014 - ECCE ASIA), 2014, pp. 2881–2886.
- [82] D. Murthy-Bellur, E. Ayana, S. Kunin, and B. Palmer, "High-frequency split-phase air-cooled SiC inverter for vehicular power generators," in 2015 IEEE Transportation Electrification Conference and Expo (ITEC), 2015, pp. 1–5.
- [83] C. Chen, M. Su, Z. Xu, and X. Lu, "SiC-based automotive traction drives, opportunities and challenges," in 2017 IEEE 5th Workshop on Wide Bandgap Power Devices and Applications (WiPDA), 2017, pp. 25–30.
- [84] M. A. Masrur, "Toward Ground Vehicle Electrification in the U.S. Army: An Overview of Recent Activities," *IEEE Electrification Mag.*, vol. 4, no. 1, pp. 33–45, Mar. 2016.

- [85] J. Guzinski, H. Abu-Rub, and P. Strankowski, *Variable Speed AC Drives with Inverter Output Filters*. John Wiley & Sons, Ltd, 2015.
- [86] Schaffner, “Sine wave filter solutions for motor drive applications (Application Note).,” Retrieved Schaffner Website <https://www.schaffner.com/fileadmin/mediadownloads/applicationnote/SchaffnerANFiltersolutionsformotordrivesapplications.pdf>.
- [87] P.- Gath and M. Lucas, “Designing LC filters for AC-motor drives,” in *IAS '95. Conference Record of the 1995 IEEE Industry Applications Conference Thirtieth IAS Annual Meeting, 1995*, vol. 2, pp. 1050–1052 vol.2.
- [88] A. Muetze and C. R. Sullivan, “Simplified Design of Common-Mode Chokes for Reduction of Motor Ground Currents in Inverter Drives,” p. 9.
- [89] A. von Jouanne and P. N. Enjeti, “Design considerations for an inverter output filter to mitigate the effects of long motor leads in ASD applications,” *IEEE Trans. Ind. Appl.*, vol. 33, no. 5, pp. 1138–1145, Sep. 1997.
- [90] H. Akagi, H. Hasegawa, and T. Doumoto, “Design and performance of a passive EMI filter for use with a voltage-source PWM inverter having sinusoidal output voltage and zero common-mode voltage,” *IEEE Trans. Power Electron.*, vol. 19, no. 4, pp. 1069–1076, Jul. 2004.
- [91] A. Simion, Livadaru, and A. Munteanu, “Mathematical Model of the Three-Phase Induction Machine for the Study of Steady-State and Transient Duty Under Balanced and Unbalanced States.”
- [92] H. Späth, *Elektrischen Maschinen*. Springer Verlag Berlin, Heidelberg, 1973.
- [93] K. Späth, *Steuerverfahren für Drehstrommaschinen - Theoretische Grundlagen*. Springer Verlag Berlin, Heidelberg, 1983.
- [94] P. K. Kovacs, *Transient Phenomena in Electrical Machines*. Elsevier Science Ltd, 1984.
- [95] J. Stepina, “Raumzeiger als Grundlage der Theorie der elektrischen Maschinen,” *Electrotech. Z. ETZ- Arch. Bd8* Pp 584–588, 1967.
- [96] L. Serrano-Lribarnegaray, “Ersetzen der Mathematischen durch die Physikalischen Raumzeiger zur Untersuchung stationärer und dynamischer Vorgänge in rotierenden elektrischen Maschinen,” *ETZ Arch. Bd8* Pp 347–352, 1986.
- [97] P. M. P. Palma, “Finite Set Model Predictive Control of the PMSM with Sine-Wave Filter,” PhD Thesis Siegen-Ger. Univ. Siegen, p. 2015.

- [98] T. Barbieri, J. Casady, E. Ayerbe, T. McNutt, and L. Kegley, "EVs Race to Adopt Silicon Carbide Power," Wolfspeed CREE Co., Jun. 2016.
- [99] "ROHM Semiconductor – Advantages of Silicon Carbide Diodes, MOSFETs and Modules," FTM - Future Technology Magazine, 01-Jan-2015. .
- [100] M. Eull, M. Preindl, and A. Emadi, "Analysis and design of a high efficiency, high power density three-phase silicon carbide inverter," in 2016 IEEE Transportation Electrification Conference and Expo (ITEC), 2016, pp. 1–6.
- [101] Cree, Inc., "Design Considerations for Designing with Cree SiC Modules," Cree Inc, 2013.
- [102] B. Drury, Control Techniques Drives and Controls Handbook. IET, 2001.
- [103] B. Wu, Y. Lang, N. Zargari, and S. Kouro, Power Conversion and Control of Wind Energy Systems. WILEY, 2011.
- [104] N. P. Quang and J.-A. Dittrich, Vector Control of Three-Phase AC Machines System Development in the Practice. Springer, 2015.
- [105] S. D. Ochoa, "Diagnostics of rotor asymmetries in inverter fed induction machines," 2012.
- [106] S. Bolognani, N. Bianchi, and M. Zigliotto, "new perspectives for electric motors in adjustable speed drives," EPE J., vol. Vol. 14, no. 1, pp. 6–12, 2004.
- [107] P. C. Sen, C. S. Namuduri, and P. K. Nandam, "Evolution of control techniques for industrial drives," in Proceedings of International Conference on Power Electronics, Drives and Energy Systems for Industrial Growth, 1996, vol. 2, pp. 869–875 vol.2.
- [108] J. Holtz, "Developments in Sensorless AC Drive Technology," in 2005 International Conference on Power Electronics and Drives Systems, 2005, vol. 1, pp. 9–16.
- [109] J. Holtz, "Perspectives of sensorless AC drive technology from the state of the art to future trends," PCIM Eur. Nürnberg Ger., pp. 80–87, Jun. 2005.
- [110] J. Holtz, "State of the art of controlled AC drives without speed sensor," in Proceedings of 1995 International Conference on Power Electronics and Drive Systems. PEDS 95, 1995, pp. 1–6 vol.1.
- [111] N. P. Quang and J.-A. Dittrich, Vector Control of Three-Phase AC Machine. Berlin, Heidelberg: Springer, 2008.
- [112] V. Berinberg and F. Götz, "Enhanced Voltage Model for Sensorless Control of a Permanent Magnet Synchronous Motor Drive." SPS IPC Drives, 2008.

- [113] R. B. Sepe and J. H. Lang, "Real-time observer-based (adaptive) control of a permanent-magnet synchronous motor without mechanical sensors," *IEEE Trans. Ind. Appl.*, vol. 28, no. 6, pp. 1345–1352, Nov. 1992.
- [114] S. Bolognani, L. Tubiana, and M. Zigliotto, "Extended Kalman filter tuning in sensorless PMSM drives," *IEEE Trans. Ind. Appl.*, vol. 39, no. 6, pp. 1741–1747, Nov. 2003.
- [115] R. Dhaouadi, N. Mohan, and L. Norum, "Design and implementation of an extended Kalman filter for the state estimation of a permanent magnet synchronous motor," *IEEE Trans. Power Electron.*, vol. 6, no. 3, pp. 491–497, Jul. 1991.
- [116] S. Bolognani, R. Oboe, and M. Zigliotto, "Sensorless full-digital PMSM drive with EKF estimation of speed and rotor position," *IEEE Trans. Ind. Electron.*, vol. 46, no. 1, pp. 184–191, Feb. 1999.
- [117] F. D. R. Figueroa, "Predictive Control Scheme of the PMSM with a Modulator of Variable Switching Frequency." Dissertation, Siegen University, Siegen, Deutschland, Jan-2017.
- [118] R. Joetten and G. Maeder, "Control Methods for Good Dynamic Performance Induction Motor Drives Based on Current and Voltage as Measured Quantities," *IEEE Trans. Ind. Appl.*, vol. IA-19, no. 3, pp. 356–363, May 1983.
- [119] J. Holtz, "perspective of sensorless AC Drive Technology," *Int. Conf. Exhib. Power Electron. Intell. Motion Power Qual.*, p. Proc., 80-87, 2005.
- [120] S. Li, Q. Ge, X. Wang, and Y. Li, "Implementation of Sensorless Control with improved flux integrator for Wound Field Synchronous Motor," in *2007 2nd IEEE Conference on Industrial Electronics and Applications*, 2007, pp. 1526–1530.
- [121] G. Mirzaeva and R. E. Betz, "Advantages and limitations of the NFO control algorithm," in *2008 Australasian Universities Power Engineering Conference*, 2008, pp. 1–6.
- [122] B. K. Bose-, *Power Electronics and Variable Frequency Drives \_ Technology and Applications*. Wiley-IEEE Press, 1999.
- [123] D. Schröder, *Elektrische Antriebe-Regelung von Antriebsystemen*, Third Edition. Springer-Verlag Berlin Heidelberg, 2009.
- [124] S. Feuersänger, *Drehgeberlose Identifikation der Rotorlage der elektrisch erregten Synchronmaschine in Mittelspannungsantrieben*. Ph.D Thesis. Siegen-Germany: University of Siegen, 2015.